



McHugh, Patrick J. (2023) *Investigating electro- and sonoelectro-oxidation processes for sustainability on Earth and the exploration of space*. PhD thesis.

<https://theses.gla.ac.uk/83429/>

Copyright and moral rights for this work are retained by the author

A copy can be downloaded for personal non-commercial research or study, without prior permission or charge

This work cannot be reproduced or quoted extensively from without first obtaining permission in writing from the author

The content must not be changed in any way or sold commercially in any format or medium without the formal permission of the author

When referring to this work, full bibliographic details including the author, title, awarding institution and date of the thesis must be given

Enlighten: Theses

<https://theses.gla.ac.uk/>
research-enlighten@glasgow.ac.uk



Investigating Electro- and Sonoelectro-oxidation processes for Sustainability on Earth and the Exploration of Space

Patrick J. McHugh

Submitted in fulfilment of the requirements for the Degree of Doctor of Philosophy

School of Chemistry

College of Science and Engineering

University of Glasgow

2022

For Patrick Gallagher & James McHugh

Abstract:

In recent years, there has been an explosion in the adoption of electrochemical methods for tackling many of the environmental issues we face in modern society. This electrochemical approach encompasses a range of highly tuneable techniques which often remove the need for harmful chemicals and high temperatures. In this thesis, we will examine how electrochemistry can be utilised for the development of “green” processes based on electro-oxidation. Demonstrating the versatility of these techniques the work herein covers a wide range of fields, the results from which can have consequences stretching from removal of pollutants from water to future space travel.

Chapter 1 provides context to the research in chapters 3 to 5; namely in introducing the motivations and current state of research behind the development of anion exchange membrane electrolyzers as a clean energy solution, the implementation of electrolysis systems in space missions, and the use of combined sono-electrochemical methods for water decontamination. In Chapter 2, the experimental techniques behind the research in this thesis is reported.

Chapter 3 reports the development of a novel anion-exchange membrane electrolyser, and its use in the electrochemical degradation of the naturally occurring polymer, lignin. The performance of the membrane, a co-polymer of dehydrofluorinated poly(vinylidene fluoride-co-hexafluoropropylene) with (vinylbenzyl)trimethylammonium chloride and N-vinylimidazole, was benchmarked against a commercial equivalent yielding comparable results.

In Chapter 4, we report an investigation into the efficiency of oxygen-evolving electrolysis at gravity levels between 0 and 1 g. The data collected from this experiment, carried out as part of the European Space Agency’s Fly Your Thesis programme, is the first study to examine the efficiency of this process at gravitational fields equal to that of the Moon and Mars. This process was tested not just at reduced gravity levels but also at those exceeding Earth’s gravity, finding that results collected in hypergravity can be extrapolated to predict the performance of the procedure in microgravity.

In Chapter 5 we revisit the work introduced in Chapter 1 with an investigation in to the sonoelectrochemical degradation of the anti-inflammatory drug diclofenac. Coupling low-frequency sonication with electrolysis performed using a Pt/Ti anode, a degradation removal efficiency of 64% under optimal conditions was achieved. Comparison of this method with

non-coupled electrolytic and sonolytic degradation indicated that at 80 kHz, there was a strong synergistic effect.

Table of Contents

Abstract:.....	III
Table of Contents.....	V
Publications.....	VIII
Acknowledgements.....	IX
Author's Declaration	X
Abbreviations and Symbols.....	XI

Chapter 1: Introduction

1.1 Introduction.....	3
1.2 Hydrogen Production using an Anion Exchange Membrane Electrolyser	3
1.2.1 Water Electrolysis.....	5
1.2.2 SPM Electrolysers	6
1.2.3 The Hydrogen Evolution Reaction in AEM Electrolysers	7
1.2.4 The Oxygen Evolution Reaction in AEM Electrolysers.....	9
1.3 Oxygen Generation in Space	10
1.3.1 Lunar Resources	11
1.3.2 ISRU Processes for Oxygen Generation.....	12
1.3.3 Extra-terrestrial Electrolysis	14
1.4 A Sonoelectrochemical Approach to Water Decontamination.....	17
1.4.1 Important Factors in Sonoelectrochemical Advanced Oxidation Processes	19
1.4.1.1 Sonication Characteristics	19
1.4.1.2 Sonication Source.....	22
1.4.1.3 Electrode Materials.....	23
1.4.1.4 Background Electrolyte.....	25
1.4.2. Recent Examples of Sonoelectrochemical Wastewater Treatment	28
1.4.2.1 Dyes.....	31
1.4.2.2 Pharmaceuticals.....	33
1.4.2.3 Pesticides	37
1.4.2.4 Surfactants	39
1.4.2.5 Sonoelectrochemical studies performed in real wastewater.....	41
1.5. Conclusions.....	44
1.6 References.....	45

Chapter 2: Background on Experimental Techniques

2.1 Electrochemical Techniques	60
2.1.1 Typical Electrochemical Setup	60
2.1.2 Linear Sweep and Cyclic Voltammetry	61
2.1.3 Bulk Electrolysis.....	63
2.1.4 Electrical Impedance Spectroscopy	64
2.2 Spectroscopy.....	67
2.2.1 UV-Vis Spectroscopy	67
2.2.2 Nuclear Magnetic Spectroscopy	68
2.2.3 Infrared Spectroscopy	72
2.3 Liquid Chromatography-Mass Spectrometry	74
2.3.1 Liquid Chromatography.....	74
2.3.2 Mass Spectrometry	75
2.4 Scanning Electron Microscopy.....	76
References.....	79

Chapter 3: Hydrogen Production by Direct Lignin Electrolysis in a Continuous Flow AEM Electrolyser

3.1 Introduction.....	83
3.2 Experimental.....	86
3.2.1 Materials	86
3.2.2 Flow Cell Components	86
3.2.3 Electrochemical Characterisation of the Cell	87
3.2.4 Preparation of PVIB Membrane	88
3.2.5 Characterisation of the PVIB Membrane	88
3.3 Results.....	90
3.3.1 Properties of the PVIB Membrane	90
3.3.2 Characterisation of the PVIB-Based Electrolyser	93
3.3.3 PVIB in Alternative Electrolyser Configurations.....	97
3.3.4 PVIB Degradation	99
3.4 Conclusions.....	104
References.....	105

Chapter 4: Oxygen Production via Electrolysis in Altered Gravity Environments

4.1 Introduction.....	110
4.2 Experimental.....	113

4.2.1 Materials	113
4.2.2 Cell Design	113
4.2.3 Experimental Rig	114
4.2.4 Investigated Parameters	116
4.2.5 Flight Plan.....	116
4.3 Results.....	119
4.3.1 Cell Consistency	119
4.3.2 Microgravity Results	122
4.3.3 Hypergravity Results	126
4.3.4 Extrapolation from Microgravity to Hypergravity	128
4.4 Conclusions.....	131
References.....	132

Chapter 5: Sonoelectrochemical Degradation of Diclofenac

5.1 Introduction.....	137
5.2 Experimental.....	139
5.2.1 Materials	139
5.2.2 Cell Setup.....	139
5.2.3 Electrochemical Characterisation	140
5.2.4 UV-Vis Spectrometry Procedure	141
5.2.5 NMR Procedure	142
5.2.6 LCMS Procedure	142
5.2.7 SEM Procedure	142
5.3 Results and Discussion	143
5.3.1 Preliminary DCF Degradation Experiments.....	143
5.3.2 LC-MS Analysis	145
5.3.3 Synergistic Index	150
5.3.4 Anode Material	152
5.4 Conclusions and Future Work	154
References.....	156

Conclusions and Future Work	161
--	------------

Appendix.....	166
----------------------	------------

Publications

‘The Effects of Ultrasound on the Electro-Oxidation of Sulfate Solutions at Low pH’

A. G. Wallace, P. J. McHugh and M. D. Symes, *ChemPhysChem*, 2019, **20**, 3134-3140

“Decoupled Electrochemical Water Splitting: From Fundamentals to Applications.”

P. J. McHugh, A. D. Stergiou, M. D. Symes, *Adv. Energy Mater.* 2020, **10**, 2002453.

“An Investigation of a (Vinylbenzyl) Trimethylammonium and N-Vinylimidazole-Substituted Poly (Vinylidene Fluoride-Co-Hexafluoropropylene) Copolymer as an Anion-Exchange Membrane in a Lignin-Oxidising Electrolyser.”

P. J. McHugh, A. K. Das, A. G. Wallace, V. Kulshrestha, V. K. Shahi, M. D. Symes, *Membranes* 2021, **11**, 425

“Predicting the efficiency of oxygen-evolving electrolysis on the Moon and Mars.”

B. A. Lomax, G. H. Just, P. J. McHugh, P. K. Broadley, G. C. Hutchings, P. A. Burke, M. J. Roy, K. L. Smith, and M. D. Symes, *Nat. Commun.* 2022, **13**, 583.

“Sonoelectrochemical processes for the degradation of persistent organic pollutants.”

W. L. Ang, P. J. McHugh and M. D. Symes, *Chem. Eng. J.* 2022, **444**, 136573.

Acknowledgements

Firstly, I would like to acknowledge my supervisor Professor Mark Symes. Mark has been an incredible mentor to me since I first joined his group during my undergraduate degree. I owe him a great deal of thanks for his invaluable advice that has always been available to me whenever I needed it. Professor Symes has quite literally taught me everything I know about electrochemistry and has been an exemplary role model; I aspire to one day have the influence on someone else's career in the way he has in mine.

Secondly, I would like to thank my Mum & Dad, and my sisters Katy & Maria for their love, wisdom, and for making me the man I am today. They have been patient, supportive, and desperate to help whenever possible; for that I am incredibly lucky.

I would also like to thank my other family, the Stevensons. Maureen, Tommy, Seonaid, Eilidh, Frank, James & Archie have made me feel like one of their own and are some of my favourite people to spend time with. A large portion of this PhD was completed during the pandemic while working from their home and, thanks in no small part to how warm and welcoming their home is, I have a lot of fond memories from that time. It is not lost on me how lucky I am to have had such a great time in those circumstances; I'm privileged to be a part of their family.

My PhD experience could have been entirely different had it not been for the many colleagues I had over the years in the Symes group. Special thanks must be given to those who were here when I joined that helped guide me when in truth, I had no idea what I was doing. Most notably Alex Wallace, a great supervisor who became a greater friend. Thanks must also be given to the Relox team Beth, Gunter, Paul and Greg. It was an incredible effort to get our experiment ready while dealing with the pandemic, no doubt this wouldn't have been possible without such great colleagues.

I must also give a separate paragraph of acknowledgment to my two closest friends, Calum Hope and Athanasios Stergiou. Their support has been vital, and some of the best times I've had both in and out of the lab in the past 4 years have been shared with them. I'm certain our friendship will last for years to come.

Finally, I want to thank Siobhan Stevenson. It is no exaggeration to say that all that I've achieved in my adult life would not have been possible without her encouragement, formidable intelligence, and her ability to improve my mood in an instant. For her love I'll be forever grateful.

Author's Declaration

I declare that, except where explicit reference is made to the contribution of others, this thesis is the result of my own work and has not been submitted for any other degree at the University of Glasgow or any other institution

I declare that this thesis has been produced in accordance with the University of Glasgow's code of good practice in research.

I acknowledge that if any issues are raised regarding good research practice based on review of the thesis, the examination may be postponed pending the outcome of any investigation of the issues.

Patrick J. McHugh

Abbreviations and Symbols

)))	Sonication
A	Ampere/Area
A.M.U.	Atomic Mass Units
AC	Alternating Current
BDD	Boron Doped Diamond
C	Capacitance
c	Concentration/Speed of Light
COD	Chemical Oxygen Demand
CV	Cyclic Voltammetry
DC	Direct Current
DCF	Diclofenac
E	Potential Energy
EC	Electrochemical
EIS	Electrical Impedance Spectroscopy
ESA	European Space Agency
f	Frequency
F	Faraday's Constant
g	Grams
GC	Gas Chromatography
h	Planck's Constant
HER	Hydrogen Evolution Reaction
HPLC	High Performance Liquid Chromatography
Hz	Hertz
I	Current/Spin Quantum Number

I_A	Acoustic Intensity
I_α	Average Intensity
IEC	Ion-Exchange Capacity
IR	Infrared
ISRU	In-situ Resource Utilisation
K	Kelvin
K_f	Force Constant of a Bond
l	Optical Path Length
L	Litre
	Membrane Thickness
LC	Liquid Chromatography
\ln	Natural Logarithm
LSV	Linear Sweep Voltammetry
M	Moles per Litre
m	Moles
	Metres
	Magnetic Quantum Number
m/z	Mass to Charge Ratio
M_0	Bulk Magnetisation Vector
min	Minute
MS	Mass Spectrometry
n	Number of Electrons Transferred per Ion
NASA	National Aeronautics and Space Administration
NMR	Nuclear Magnetic Resonance
OER	Oxygen Evolution Reaction
P_a	Sound Wave Amplitude
P_h	Hydrostatic Pressure

P_{vg}	Vapour Pressure
ppm	Parts per Million
PTFE	Polytetrafluoroethylene
PVIB	Co-polymer of Dehydrofluorinated Poly(vinylidene fluoride-co-hexafluoropropylene) with (Vinylbenzyl)trimethylammonium Chloride and N-vinylimidazole
Q	Charge
R	Resistance
R_m	Maximum Bubble Size
R_p	Polarisation Resistance
R_r	Resonant Radius
R_s	Series Resistance
RPM	Revolutions per Minute
s	Seconds
SEM	Scanning Electron Microscopy
SI	Synergistic Index
t	Time
TOC	Total Organic Carbon
TOF	Time of Flight
US	Ultrasonic
UV-Vis	Ultraviolet-Visible
V	Volt
W	Watt
Z	Impedance
α	Rate of Change
γ	Gyromagnetic Ratio

δ	Chemical Shift
ε	Molar Extinction Coefficient
κ^m	Hydroxide Conductivity
λ	Wavelength
μ	Magnetic Moment/Effective Mass
ν	Frequency/Vibrational Quantum Number
ρ	Density
σ	Conductivity
τ	Bubble Collapse Time
φ	Phase Shift
ω	Radial Frequency
ω_a	Applied Ultrasonic Frequency

Chapter 1:

Introduction

This chapter contains expanded and updated sections from the following publications:

“Decoupled Electrochemical Water Splitting: From Fundamentals to Applications.”

P. J. McHugh, A. D. Stergiou, M. D. Symes, *Adv. Energy Mater.* 2020, **10**, 2002453.

“Sonochemical processes for the degradation of persistent organic pollutants.”

W. L. Ang, P. J. McHugh and M. D. Symes, Chem. Eng. J. 2022, 444, 136573.

Acknowledgements and Declarations

Some of the work presented in this chapter was originally published in collaboration with both my supervisor, Dr. Mark Symes, and colleagues, Dr. Athanasios Stergiou, Dr. Wei Lun Ang. I would like to thank and acknowledge both for their contribution to the original review. All parts in the original review not written by me have been replaced or removed entirely such that the work presented here is entirely my own.

Abstract:

The population and industry boom over the last few centuries has led to significant global warming and climate change. The result of this has been a marked increase in extreme weather events and a rise in the contamination of our waterways. In this chapter, we explore the current state of the art in three fields where these issues are being addressed: the maturation of anion-exchange membrane electrolyzers as a clean energy technology, the development of electrolysis as an in-situ resource utilisation method for future space missions, and the recent rise in popularity of ultrasound assisted electrochemical degradation of some pollutants.

1.1 Introduction

As the global population continues to grow larger, so too does the environmental “footprint” that mankind leaves on Earth’s climate. Currently, fossil fuels such as coal, oil and natural gas remain the world’s primary sources of energy. It is becoming increasingly clear that greenhouse gases (such as CO₂) that are formed during combustion of these fuels are linked to oceanic and global temperature rises,^{1,2} shrinking ice sheets,³ ocean acidification⁴ and extreme weather events.⁵ Moreover, the population boom over the last 100 years has been matched by a growth in death and disease caused by water pollution; some estimates link this problem to 14,000 deaths per day.⁶ Naturally, there has been significant efforts globally to address this environmental threat, be that through tackling aquatic pollution, the development of alternative energy solutions, and even by setting our sights to space where man may eventually be forced to find another home. In this chapter we present an overview of some of this research, focussing on the development of anion exchange membrane electrolysers, combining ultrasound and electrolysis towards the degradation of persistent organic pollutants in wastewater, and the electrochemical generation of oxygen in altered gravity.

1.2 Hydrogen Production using an Anion Exchange Membrane Electrolyser

Considering the detriments that come with the use of fossil fuels as our primary energy source, many governments have sought to develop and implement energy systems which utilise renewable energy sources. Renewable energy sources, such as wind, solar and tidal energy constitute the most promising of these clean energy solutions, but suffer from the fact that they are intermittent.⁷ Direct power supply from these sources therefore cannot be relied upon to satisfy instantaneous energy demands.⁸ A means of storing the energy generated by these renewable sources is therefore essential if we are to depend more heavily on renewably-generated power.⁹

Hydrogen (H₂) is often proposed in this context as a promising “carbon neutral” energy carrier (*i.e.* fuel). In such a system, renewably-generated electricity is used to electrolyse water to generate hydrogen and oxygen. The oxygen may be vented to the atmosphere whilst the hydrogen is stored as a fuel. This hydrogen is then subsequently oxidised (either by combustion or in a fuel cell) to re-generate water and to release energy. Hydrogen is not a perfect fuel, but it does have a number of attractive properties such as its low toxicity, ability

to be transported safely over long distances *via* pipeline¹⁰ and its high energy density per unit mass (three times greater than that of gasoline).¹¹

The process of water electrolysis can be considered in terms of its two corresponding half-reactions: the hydrogen evolution reaction (HER) and the oxygen evolution reaction (OER). The corresponding half-equations differ somewhat depending on the pH at which the electrolysis is carried out. At low pH, the HER and OER proceed as follows (all potentials are versus the standard hydrogen electrode, SHE):



Whereas, under alkaline pH, the half-reactions occur as below:



Hence there is a significant electrical energy requirement to drive water electrolysis. Under standard conditions, a potential difference of 1.23 V is the thermodynamic minimum required to electrolyse water. However, in order to overcome various kinetic and resistance barriers (and so to drive appreciable currents to flow for the OER and HER), additional voltage is required. This additional voltage is referred to as overpotential, which is a sum of overpotentials relating to concentration, ohmic resistances in the electrolyser, and to the kinetic overpotentials for the individual HER and OER half-reactions.¹² Of these various overpotentials, the overpotential requirement for the OER tends to dominate as the generation of O₂ is a kinetically-demanding four-electron, four-proton process.^{13,14} The OER is therefore often held to be the main kinetic bottleneck for the electrolytic generation of hydrogen from water.

1.2.1 Water Electrolysis

In its simplest form, water electrolysis will occur under the influence of a direct current between two electrodes in a single compartment. This crude form presents many limitations, the most deleterious of which is the lack of separation of the product gases. From Equations 1.1- 1.4, it can be seen that two moles of hydrogen are formed for every mole of oxygen generated. These gas-evolving reactions occur simultaneously, potentially creating a highly explosive mixture.¹⁵ Commercially, this is addressed *via* the use of membranes which separate the cell into anodic and cathodic chambers. Large scale water electrolysis at high pH is carried out using a liquid alkaline electrolyte (corrosive aqueous KOH solution), at low temperatures (293-353 K) with an asbestos diaphragm (figure 1.1).¹⁶ In this setting, the anodic and cathodic pressures must be carefully controlled to prevent gas permeation across the membrane.¹⁷⁻¹⁹ Recently, considerable progress has been made in the development of solid polymer membrane electrolyzers where an anion or proton exchange membrane (*e.g.* Nafion) is employed within a compressed cell stack. Though relatively expensive, these cell configurations can operate at large pressure differentials, at excellent operational current densities and without the need for caustic electrolytes. In these cells, the product streams are kept separate as gas crossover rates across the membranes are low (although crucially even these membranes are not entirely gas impermeable).^{16,19-23}

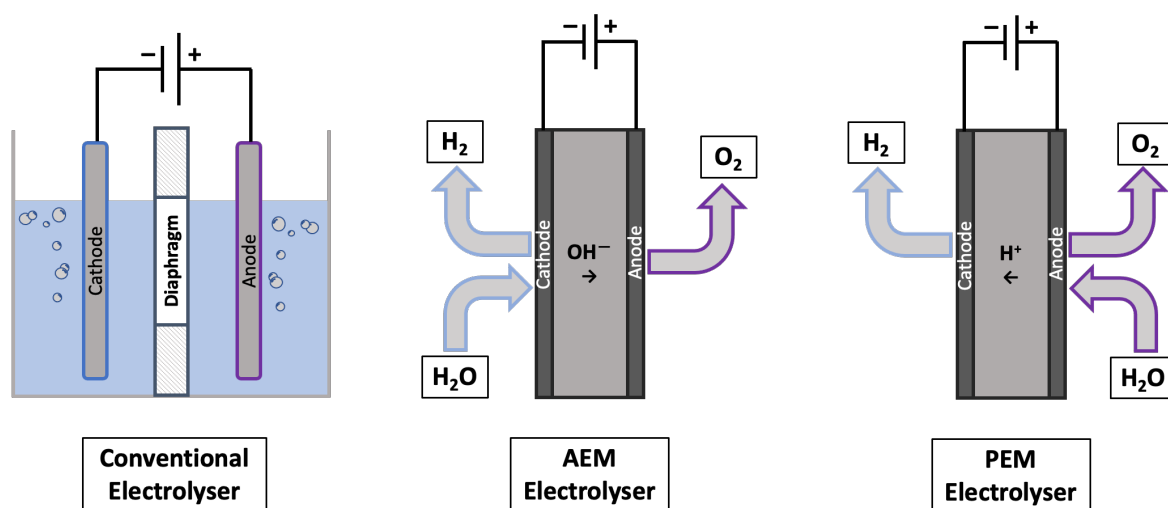


Figure 1.1: Simplified diagram of a conventional hydrogen electrolyser (left), an anion exchange membrane electrolyser (middle), and a proton exchange membrane electrolyser (right). Redrawn from ref [19].

The issue of separating these gases becomes more complex when using renewable energy sources, where the power inputs are variable and/or low. In such cases, the low current densities that are achieved correspond to low rates of gas production, and these rates of gas production may in turn start to approach the rates of gas crossover for some membranes, potentially leading to safety issues. A current density of 10 mA cm^{-2} is considered a useful benchmark for solar driven electrolyzers, as this is the approximate current expected of a water splitting device operating at 10% solar-to-fuels efficiency under “1 Sun” illumination (AM 1.5, 100 mW cm^{-2}).²⁴ In this scenario, the presence of hydrogen in the anodic chamber would be particularly hazardous as the lower explosion limit of hydrogen in oxygen is only 4 mol% H_2 in O_2 .^{25–28} Furthermore, even if efficient and safe gas separation could be achieved, any solar-to-hydrogen device in which the half-reactions of water splitting remain coupled (as in a conventional electrolyser) will suffer from the fact that the rate of the relatively facile HER would still be limited by the more sluggish OER. In this context, harnessing low pressures of hydrogen gas safely and efficiently from large solar-to-hydrogen arrays remains an unsolved challenge.

1.2.2 SPM Electrolyzers

Solid polymer membranes can be categorised based on the ion selectivity of their respective membranes; proton exchange membrane (PEM) electrolyzers which, as the name suggests, operate through proton migration and anion exchange membrane (AEM) electrolyzers in which hydroxyl ions (OH^-) move between electrodes facilitated by a membrane designed around their migration. Since their conception in the early 1950s, proton exchange membrane electrolysis cells have become the subject of a great number of reported studies, even more so than their anion exchange membrane counterparts.²⁹ Put simply, these cells split water at the anode, generating oxygen and protons. These newly formed protons move through the proton exchange membrane to the cathode, where they are reduced to form H_2 . These proton exchange membranes (figure 1.1, right), are designed to ensure high proton conductivity which in turn yields incredible operational current densities (up to 10 A cm^{-2}).³⁰ Moreover, these cells typically offer features attractive to an industrial setting such as a compact design and high hydrogen output pressure.³¹ However, what has slowed the adoption of this technology is its high capital cost. As can be expected when considering equations 1.1 & 1.2, a highly acidic environment is generated throughout operation of these

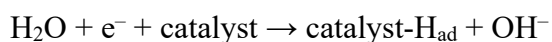
cells which in turn introduces limitations on the choice of materials from which they can be constructed. Where this can become most economically damaging is the electrocatalyst where, for this reason, example cells have been limited mainly to noble metal catalysts at the anode, whilst Pt is typically used to catalyse the cathodic reaction.¹⁹ At present, the high cost of these metals has impeded the large-scale application of this technology. Should PEM electrolyzers become the favoured solution for a future hydrogen economy, the market demand for these already scarce materials would only drive their price up further, therefore significant electrocatalyst innovation is considered necessary before widespread adoption of this technology is likely.³²

In function, there are some similarities for both AEM and PEM electrolyzers however, one of the main ways in which they differ is in the reactions that occur at each electrode. In AEM electrolyzers, water is reduced at the cathode forming hydrogen, which can be collected as a gas, and hydroxyl ions which, like protons in PEM electrolyzers, move through the membrane electrolyte to the anode. At the anode, these hydroxyl ions are oxidised forming water and oxygen.¹⁹ Arguably the greatest advantage of AEM electrolyzers over their PEM counterparts is that they do not require Pt-based electrocatalysts, and thus their construction comes with a lower capital cost.³¹ That being said, this configuration of electrolyser is disadvantaged by three main issues: (i) the relatively sluggish kinetics of OH^- through the AEM effectively impose a limit to the maximum operational current density of these cells which may always be lower than this value in PEM electrolyzers (ii) owing to the larger pores necessary for OH^- conduction, these membranes are often less stable at high pressure differentials (iii) an increase of the functional groups which promote OH^- conductivity also leads to an increase in water uptake which negatively impacts the membranes stability.^{31,32}

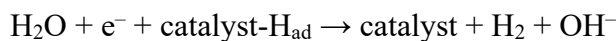
1.2.3 The Hydrogen Evolution Reaction in AEM Electrolyzers

As mentioned in section 1.2.2, the hydrogen evolution reaction in these cells can be summarised as water reduction, yielding hydrogen, electrons, and hydroxyl radicals. This process is much slower than the HER in acidic environment as the mechanism for the reaction requires proton dissociation of the water molecule & formation of adsorbed proton reaction intermediates. The process is described below where steps 2a and 2b represent the two possible hydrogen-evolving steps:^{31,33–36}

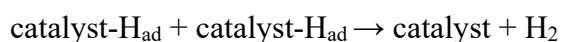
1. The Volmer Step (first electron-proton transfer):



2a. The Heyrovsky Step (second electron-proton transfer):



2b. The Tafel Step



Regardless of whether the HER follows the Volmer-Heyrovsky or Volmer-Tafel routes, initial breaking of the relatively strong H-OH bond is necessary and is generally considered the rate determining step.³⁷ As previously discussed, one of the benefits to using an AEM electrolyser over its PEM counterpart is the availability of suitable electrocatalysts that are not based on noble metals. Pt-based catalysts can still be used for the reaction in this environment but are not free from the sluggish kinetics demanded in the Volmer step.

Electrocatalysts based on Ni and other transition metal catalysts are common among published AEM electrolyser configurations. The suitability of these metals for the role was illustrated well by Subbaraman et. al., who assessed Co, Fe, Ni & Mn three-dimensional metal hydroxide catalysts on their proficiency in dissociating water.³⁸ Seeking to benchmark the trends in OER & HER reactivity to aid future catalyst development, the authors modified well-characterised Pt(111) surfaces with 3d-M metal hydr(oxy)oxide clusters. The results of their investigation concluded that in terms of the HER on these surfaces, the order of reactivity was Ni > Co > Fe > Mn. Interestingly, they found that the marker for reactivity in both the HER and OER was the strength of adsorption between the studied metal surface and hydroxyl units formed during the dissociation of water as their presence greatly influenced hydrogen adsorption on nearby sites. The findings of this study are in line with the trends observed in published examples of these electrolysers as indeed, Ni is commonly employed as the HER electrocatalyst though not always as the sole metal present. Several Ni-based alloys have been proposed that offer improved selectivity and stability over Ni catalysts, NiMo alloys in particular have been shown to exhibit excellent HER performance.³⁹⁻⁴¹ In one such study, an AEM electrolyser was constructed using NiMo and

NiFe as their cathode and anode respectively.⁴² The researchers used only water as their feedstock and were able to demonstrate operational current densities of 400 mA cm⁻² at a cell potential of 1.8-1.85 V, albeit with catalyst loading equal to 40 mg cm⁻². Moreover, this cell was found to be stable during operation at this current over 8 hours. In a more recent example, an amorphous NiMo cathode was prepared by reducing an aqueous solution containing both metals in the presence of sodium borohydride.⁴³ This alloy preparation method offered improved surface area which led to the incredible performance metric of achieving 1 A cm⁻² at 1.9 V. Moreover, the researchers found that in this same experimental setup, a Pt particle equivalent cathode offered only minimal improvement (1 A cm⁻² at 1.8 V).

1.2.4 The Oxygen Evolution Reaction in AEM Electrolysers

The main source of overpotential in AEM water electrolysis is generally considered to be the oxygen evolution reaction due to it being a four electron four proton coupled reaction; the mechanism of this reaction proceeds as follows (M indicates catalyst site):⁴⁴



Due to the necessity of the catalyst to form adsorbed species in each of the 4 steps in the mechanism above, optimising the adsorption energy of the intermediates is of great importance during catalyst development.³⁰ For example, if oxygen only weakly adsorbs to the surface of the catalyst the formation of the MOH species will be less prevalent and limit the reaction; likewise, if oxygen adsorption is favoured too much, the adsorbed species (MOOH) is stable and retards the reaction. Thus, an effective OER catalyst must have a binding strength to the intermediates within a moderate range. Example materials that fall within this range include RuO₂, NiO & LaNiO₃.⁴⁵ IrO₂ and RuO₂ are often cited as the benchmark materials against which prospective OER catalysts assess their performance.^{31,46} Ni-Fe based materials have come to the fore with a string of example publications

demonstrating catalysts which rival these benchmarks.³¹ In 2020, Koshikawa et. al. reported an AEM electrolyser utilising a nickel and iron-containing layered double hydroxide (NiFe-LDH).⁴⁷ Using this catalyst, the OER could be performed at 10 mA cm^{-2} at an overpotential of only 247 mV; to reach the same current using a conventional IrO_x catalyst an overpotential of 281 mV was necessary. The researchers demonstrated that this superior performance held even at higher currents, with cell voltages at 1.0 A being 1.59 vs 1.61V at 1.0 A cm^{-2} . For the electrolyser containing the NiFe-LDH anode, this value corresponded to an energy conversion efficiency of 74.7% making it one of the highest performing SPM electrolysers not using a noble metal catalyst that to date has been reported.

One other approach to combating the sluggish OER in these electrolysers, beyond improvements in electrocatalyst technology, is to replace this reaction altogether with an oxidation reaction requiring significantly less overpotential. To that end, Chapter 3 of this thesis details the development of an AEM electrolyser using the biopolymer lignin as an anodic feedstock in conjunction with a novel anion-exchange membrane.

1.3 Oxygen Generation in Space

The idea of mankind spreading out from our globe and colonizing other planets is one that has garnered constant fascination. However, efforts towards this have stalled somewhat in the last 50 years. The last time a person set foot on the moon was 1972 and, in the years since, various financial and political barriers have prevented this feat from being repeated. This may all soon change as in the coming decade, two major superpowers are planning to put astronauts on the Moon. NASA's ARTEMIS programme (performed in collaboration European, Japanese, and Canadian space agencies) is focussed on lunar exploration with the main intention of reviving a human presence on the moon; ARTEMIS III will mark the first time humans have returned to the moon, and is scheduled to launch in 2025.⁴⁸ Likewise, the China Aerospace Science and Technology Corp. have similarly ramped up efforts, with the Chief Designer of their Chinese Lunar Exploration programme claiming a crewed landing is possible before 2030.⁴⁹ The success of these plans is intrinsically linked to our ability to guarantee a stable supply of oxygen which can be used both as a propellant, and to generate a liveable environment for astronauts. With every kg of cargo in the payload of any space flight comes an exorbitant cost and so the further from earth one goes, the less efficient it would be to bring all necessary oxygen. For reference, it has been estimated that on NASA's space shuttle, the cost of launching to low-earth orbit was around \$54,500/kg and though

this number has decreased in recent years, this is still considerably expensive; SpaceX's Falcon 9 (with the Dragon capsule necessary for manned flight) costs around \$23,300/kg.⁵⁰ As such, the development of methods that can bring down this cost could be hugely important to the feasibility of not only these missions, but also to our future efforts to reach celestial bodies further afield.

1.3.1 Lunar Resources

One approach to improve the viability of these missions is through the development of energy methods centred around resources local to the Moon and Mars. This would have both short and long term benefits in that in the short term, it would help in making these missions more financially sustainable, and in the longer term these resources could then serve as a replacement for the depletion of Earth's non-renewable resources.⁵¹ The blanket term given to these methods is in-situ resource utilisation (ISRU). From this point, discussion of resources which can be harnessed for ISRU processes will be limited to those present on the Moon, as it is likely that the viability of these processes will be established here before other planetary bodies are inhabited.

The layer of regolith which covers the surface of the Moon is composed of rocks, mineral fragments, and glasses ranging vastly in size. This layer, formed through the continuous bombardment of meteoroids over millions of years, has been crucial in our understanding of the Moon as it is here that all material samples that have been examined originate.⁵² What's more, the study of Lunar regolith has found that it holds great potential value as it has an incredibly high oxygen content (40-45%),⁵² as well as an abundance of a number of metals such as Fe and Ni.⁵¹ This naturally has led to significant efforts to develop means of recovery of these materials from the Lunar surface; should this be achieved, lunar regolith could well serve as the primary feed stock for ISRU processes on the Moon. This is further driven by the sheer abundance of regolith present on the Moon with measurements indicating this layer is as thick as 10 metres in some areas.⁵²

Based on the study of lunar samples collected during the "space-race" of the 1960s & 1970s, the prevailing theory was that the environment in which the Moon was formed led to the evaporation of all water and volatiles from its surface.⁵³ This idea remained the consensus until the late 1990s, however, we know today that the Moon is not a dry sphere. At the Moon's poles, large deposits of ice have been confirmed, residing in permanently shadowed craters.^{54,55} As discussed in detail in section 1.2, water can be readily converted to both

oxygen and hydrogen through electrolysis and also, is a requirement for human life. However, an important consideration to be made is that there may be other materials encased in this ice. Due to the extremely low temperatures (<120 K) in permanently shadowed lunar craters, they have been found to act as cold traps and so hold a variety of volatile materials trapped from solar winds. For example, in the Lunar Crater Observation and Sensing Satellite (LCROSS) experiment, the upper stage of a rocket was purposely crashed into a permanently shadowed crater close to the south pole of the Moon. Then, an accompanying spacecraft analysed the resulting ejecta cloud using UV-Vis & IR spectroscopy to characterise the composition of the ice deposit. The main species detected, in order of abundance, were as follows: H₂O, H₂S, NH₃, SO₂, C₂H₄, CO₂, CH₃OH, CH₄, OH.⁵⁶ This makes the presence of ice an attractive focal point for the development of ISRU processes, however, a challenge remains; although the presence of this ice is unequivocal, there are gaps in our knowledge concerning its quantity, content, and ease of extraction.⁵⁵

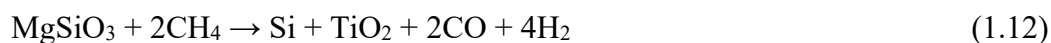
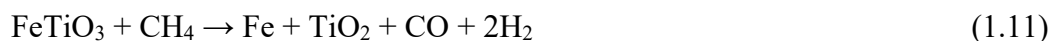
1.3.2 ISRU Processes for Oxygen Generation

The majority of ISRU research has been focussed on the production of oxygen due to its necessity for life and potential use as a propellant in rockets.⁵¹ One such process takes advantage of the titanium-iron oxide mineral ilmenite (FeTiO₃), which is considered to be the fourth most abundant mineral on the Moon.⁵⁷ The reduction of this mineral, by heating at a moderate temperature (900 °C), can yield oxygen (or water if performed in the presence of hydrogen) (equation 1.9 & 1.10).⁵⁸⁻⁶⁰



The two main disadvantages to this approach are that the presence of sulphides in the feedstock can lead to the production of H₂S which would then need to be removed in an additional purification step, and the process as a whole is limited by the ilmenite content in the feedstock; for this reason it is only suitable for use on regolith from certain areas of the Lunar surface.⁶¹ The reduction of ilmenite, and other oxygen-rich minerals, has also been demonstrated using methane.^{62,63} Here, the process is performed at a temperature such

that the methane decomposes to carbon, which then acts as a reducing agent. The products of this reduction are mainly hydrogen and carbon monoxide (equations 1.11-1.13). A further Ni-catalysed reduction is performed using these products to give methane and water (equation 1.14).⁶¹ This approach is hindered by high operating temperatures and the complexity of its multi-step procedure.



Oxygen can also be obtained direct electrolysis of lunar regolith. Here, the regolith is made molten by heating to temperatures of around 1600 °C and a potential is applied for the simultaneous generation of oxygen from silicates at the anode (equation 1.15) with reduction of metal cations to their respective metals at the cathode (equation 1.16).⁶⁴ The ability here to use regolith with no prior treatment is both this method's main benefit and disadvantage; while undoubtedly attractive by allowing for oxygen production utilising an abundant feedstock, the multi-component nature of the regolith gives rise to a number of competing reactions which decrease the efficiency of the approach. In addition, the high operational temperatures required make this process energy intensive.



The main drawbacks to the methods discussed so far have either been related complexity of the multi-step process or the requirement of extreme temperatures. One oxygen extraction technique not burdened by these detriments is the FFC (Fray, Farthing, Chen)-Cambridge process.⁶⁵ Using molten CaCl_2 as an electrolyte, this approach allows for the electrochemical reduction of solid lunar regolith whereby electrolytic oxygen production is achieved alongside the extraction of metals from their respective oxides. First demonstrated using

TiO₂, this method extracts oxygen from a decomposing cathode entirely in the solid state.⁶⁶ This oxygen, dissolved in the molten salt is then discharged as a gas upon oxidation at an inert anode. In the years since, the effectiveness of this method in generating a variety of different metals from their oxides has been demonstrated.^{66–69} More recently, Lomax *et. al.* applied this technique using a setup in which the cathode was formed from a loose powder sample of lunar regolith simulant.⁷⁰ Analysis of the regolith both before and after electrolysis found that 96% of the oxygen content had been removed leaving a mixture of metal alloys. Only around a third of this oxygen was detected in the anodic gas stream with the rest reacting with the vessel leading to corrosion. Despite this, the authors suggest that future reactor design may allow for improvement of this with almost complete recovery of all oxygen in a regolith sample being feasible.

1.3.3 Extra-terrestrial Electrolysis

As discussed extensively in section 1.2, in a number of relatively straightforward processes oxygen can be produced electrochemically; what was not mentioned is that these processes can only really be considered straightforward if performed in the presence of a strong gravitational field. When performing gas-evolving electrolysis in altered gravity, the behaviour of the produced bubbles changes which in turn can affect the overall efficiency of the process.

The evolution of gas bubbles generated at an electrode surface follows four steps, whose names are italicised in the following description.⁷¹ The first step, *nucleation*, is where bubbles form at active sites on the electrolysis due to a supersaturation of the electrolyte. Once formed, the bubbles go through a *growth* phase where the newly nucleated bubbles get bigger both through the continuing electrolysis procedure and through the coalescence of bubbles formed on neighbouring active sites. As these bubbles grow in size, the force of buoyancy acting upon the bubble will increase in magnitude until it surpasses the interfacial tension between the bubble and the electrode surface. Once bubbles reach this critical size the third step, *detachment*, occurs. The last step in this process, *rise*, concerns the behaviour of the bubble as it enters the bulk electrolyte which is governed by convection.

Buoyancy, as mentioned above, is the upward force opposing the weight of the bubble exerted by the electrolyte and is proportional to the gravitational field in which the electrolysis is being performed.⁷² Considering that the gravitational field on the Moon is 1/6 of the Earth's, it is evident that the behaviour of the bubbles in both the *detachment* and *rise*

steps will be significantly different. Namely, in reduced gravity the interfacial tension will hold the bubble on the surface for longer which will extend the *growth* phase.⁷³ While retained on the surface of the electrode, the bubble blocks contact between the electrode and the electrolyte; in reduced gravity, with longer retention of each bubble, this can impede mass transport, effectively decrease the active area of the electrode, and thus increase overpotentials necessary to drive the process.^{74–78} A number of studies have investigated this efficiency drop experimentally using a microgravity (i.e. near 0 g) environment generated using a drop-tower or on parabolic flight.^{73,75–81} Studying hydrogen evolution from sulfuric acid solutions in microgravity, Kaneko *et. al.* found that the decrease in gravity yielded increases in average bubble sizes alongside a considerable drop in current densities recorded at fixed potential.⁷⁹ Similar findings were made by Guo *et. al.* when operating a continuous-flow methanol electrolyser in a drop tower.⁸² Both reports concluded that in microgravity the process was limited by mass transport to and from the electrode whereas in Earth's gravity this process is kinetically controlled.⁸¹ In 2013, in papers published by Derhoumi *et. al.* and Mandin *et. al.* the behaviour of gas bubbles generated at a gold anode during the microgravity phases of parabolic flight was examined.^{80,81} At fixed current density, it was noted that a drop in the gravity resulted in a higher potential requirement. They also observed that the absence of buoyancy led to an increase in bubble size and population at the surface of the electrode. More recently, Brinkert *et. al.* detailed the performance of an photo-electrochemical cell when operated in microgravity using a drop tower.⁷⁸ Using indium phosphide photocathodes modified with rhodium, the researchers examined the effect that tuning the surface topography can have on mitigating the efficiency decreases when performing electrolysis in reduced gravity. Two photocathodes were used: In one, rhodium particles were simply electrodeposited on a thin film In-P electrode while in the other shadow nanosphere lithography was used to produce a hexagonal array of three-dimensional rhodium structures (figure 1.2). When using the nanostructured catalysts, it was found that bubble nucleation occurred preferentially at the tips of these Rh structures and so the resulting bubbles have much smaller contact area with the electrode surface than when using conventional electrodes. This naturally weakens the interfacial tension between the surface and the bubble therefore promoting detachment over growth and coalescence. This benefit was well illustrated in the current-potential curves recorded by the authors; the current density recorded using the conventional thin film photocathode in microgravity topped out at $\sim 5 \text{ mA cm}^{-2}$, whereas for the nanostructured electrode this value exceeded 15 mA cm^{-2} .

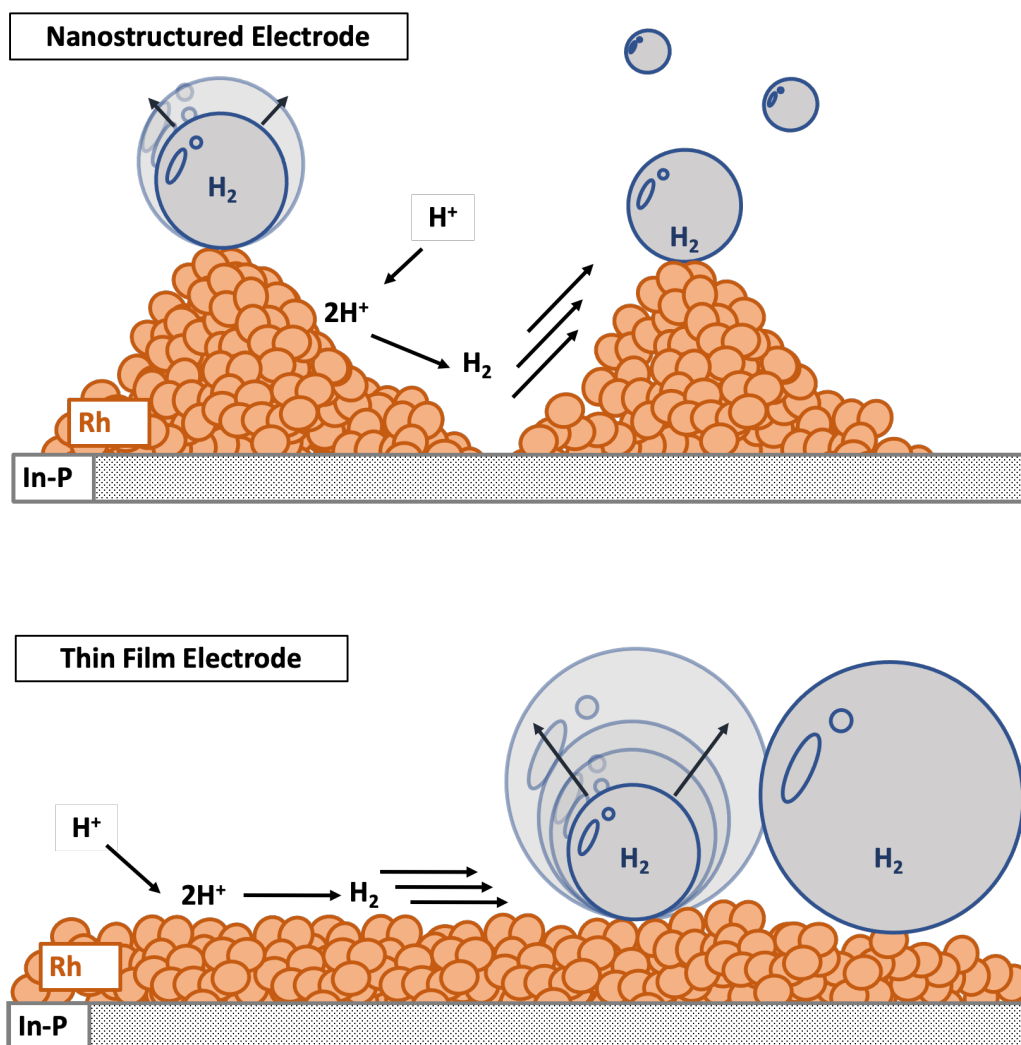


Figure 1.2: Diagram showing how bubble formation occurred on the two electrodes used by Brinkert et. al. On the thin film electrode, gas evolution occurred through nucleation and growth upon the surface. On the nanostructured electrode, H_2 generation was favoured at the tips of the three-dimensional Rh structures. The distance between these tips prevented coalescence and so retarded the formation of an insulating gaseous layer. Redrawn from ref [78].

All the experimental work discussed thus far in this section sought to compare the efficiency of these processes in Earth's gravity (1 g) with microgravity (near 0 g). However, the reader may have noticed an absence of experimental work in the gravity ranges relating to the Moon and Mars. In chapter 4 of this thesis, we present the first and only experimental validation of the efficiency of gas-evolving electrolysis at gravity levels between 0 & 1 g, including those equivalent to Lunar and Martian gravity.

1.4 A Sonoelectrochemical Approach to Water Decontamination.

As industry in the 21st century continues to expand, the need for effective methods for wastewater decontamination has become ever-more pressing. A large number of industrial processes produce and discharge hazardous effluents containing various dyes, pharmaceuticals, pesticides, surfactants, heavy metals, and so on, which pose a potential risk to local ecosystems. Conventional treatment methods have often struggled to deal with this wastewater effectively.^{83–88} Persistent organic pollutants, often present in industrial wastewater, are perhaps of the most concern, and have been linked to a number of chronic and acute medical conditions, including cancers, hypertension, cardiovascular disease, diabetes, suppression of the immune system, adverse effects on cognitive and neuro-behavioural function, and disruption of the function of sex steroids and the thyroid gland.⁸⁹ It is in this context that Advanced Oxidation Processes have come to the fore for the treatment of such wastewater. Advanced Oxidation Processes generate highly oxidising radical species that are capable of the complete mineralisation of dissolved organic pollutants (i.e. their conversion to ubiquitous and harmless mineral species such as CO₂, water and N₂).⁹⁰ First defined in 1987 as a process which generated hydroxyl radicals in sufficient quantity to purify water, the definition of an Advanced Oxidation Process has since been expanded to cover the generation of other reactive oxygen species (e.g. sulfate radicals, superoxide radicals etc.).⁸⁶

One effective route to radical generation in liquids is through the application of ultrasonic radiation. When ultrasound is applied to a liquid medium, it gives rise to pressure differentials. Due to the sinusoidal nature of the applied ultrasonic field, points in the medium may be subject to successive periods of positive pressure (compression) and negative pressure (rarefaction) (Figure 1.3). During periods of rarefaction, gaseous bubbles form which can increase in size with successive cycles; this process occurs on the microsecond timescale and, if a critical size is reached, can culminate in violent bubble collapse. These cycles of bubble generation, growth, and collapse (or “cavitations”) culminate in extremely high energy events and can yield temperatures and pressures calculated to exceed 2000 K and 500 bar.^{91–93} The volatilised molecules within these bubbles are subject to such harsh conditions during bubble collapse that their molecular bonds can be cleaved, yielding radicals.^{94–98} In addition, the operating parameters of the ultrasonic irradiation (e.g. frequency, power) can be tuned so as to maximise cavitation, allowing the optimisation of radical production.⁹⁹ Furthermore, it has been shown that application of an ultrasonic field to a liquid medium may lead to enhanced mass transport, thermal variations

caused by cavitation, and shear forces which can affect large molecules, particles, and surfaces.⁹⁷ Electro-oxidation of aqueous solutions is also known to bring about generation of hydroxyl radicals ($\cdot\text{OH}$) at the anode. With this in mind, it has long been understood that the coupling of ultrasonic radiation with other methods for radical production (especially electrochemical techniques) can be beneficial, with a synergistic relationship observed in many cases.¹⁰⁰⁻¹⁰³ Many of the inhibiting factors associated with electrochemistry, such as electrode passivation and mass transport at the electrode-electrolyte interface, are lessened under the action of an ultrasonic field.

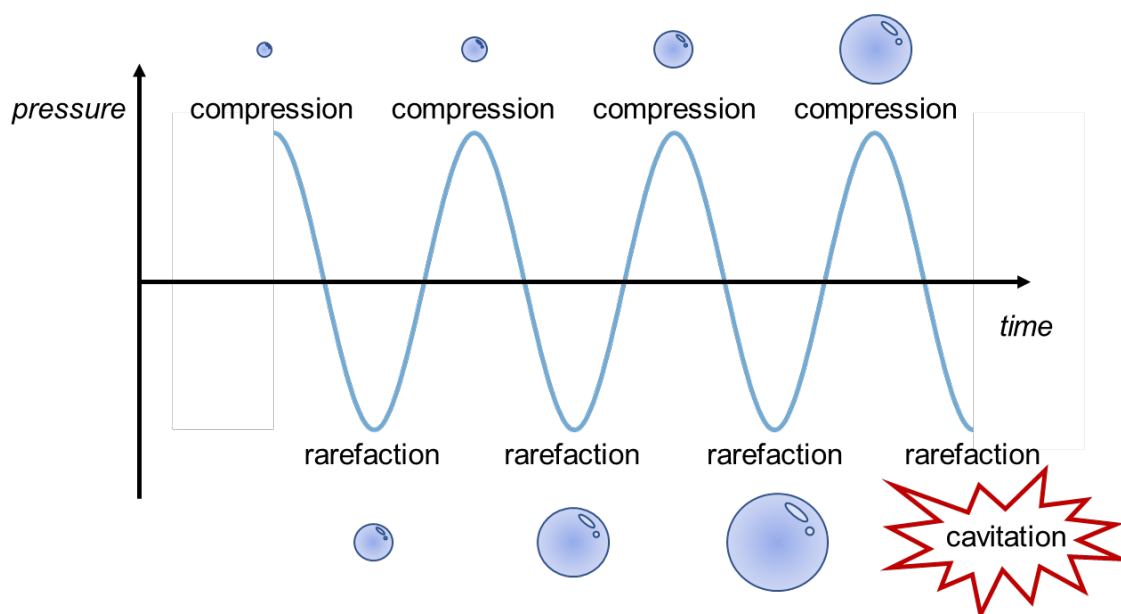


Figure 1.3: Diagram of bubble growth and cavitation under the action of a sinusoidal ultrasonic field.

1.4.1 Important Factors in Sonoelectrochemical Advanced Oxidation Processes

An understanding of electrode materials, reactor design, and operating conditions is vital for optimising the performance of sonoelectrochemical processes, and determining aspects such as pollutant degradation efficiency, process feasibility, energy efficiency, and environmental impacts. A few of the most important parameters which directly or indirectly affect the process performance are described below. In the following, we shall focus largely on oxidative degradation of organic pollutants. Electro-reductive routes to pollutant degradation may also be operating in some cases, and interested readers are referred to a recent review of electro-reductive water treatment.¹⁰⁴

1.4.1.1 Sonication Characteristics

The term ultrasound refers to sound with a frequency greater than the upper limit of the audible range of humans, typically 20 kHz and above. As the range above this threshold is large, the effect that sonication has on a liquid medium varies greatly within the span of frequencies classified as ultrasound. As such, several studies have sought the optimal frequency to maximise the number of acoustic cavitation events and achieve promoted degradation of their pollutant. In a study published in 2014 by Shestakova *et al.*, the sono-, electro-, and sonoelectrochemical removal of methylene blue dye was investigated across a wide range of frequencies (20, 40, 380, 850, 1000 & 1176 kHz).¹⁰⁵ The researchers first performed sonolysis at these frequencies before coupling the best performing frequencies to electrolysis. Despite not being the highest frequency trialled, the most effective setting was found to be 850 kHz which, when coupled with constant-current electrolysis at 20 mA, completely decolourised the solution in 45 mins, and reduced the COD value by 85.4% after 2 hours. In a follow up study on the degradation of formic acid, Shestakova *et al.* coupled 20 mA electrolysis with sonication at different frequencies which yielded a similar result.¹⁰⁶ At 381 kHz the degradation of formic acid was most efficient with a kinetic rate constant of 0.0374 min^{-1} , with higher sonication frequencies yielding lower kinetic rate constants; 0.0234 min^{-1} at 863 kHz, 0.0184 min^{-1} at 992 kHz, and 0.0201 min^{-1} at 1176 kHz. Similarly, a recent study on the degradation of the dye tartrazine found that the removal efficiency of the process reached a peak at 860 kHz (19.4%).¹⁰⁷ This value exceeded the performance when the method was employed at a lower frequency (18.4% at 578 kHz) or higher frequency (18% at 1140 kHz). A likewise optimal frequency peak was recorded in a study

by Yang *et. al.* in their investigation on the degradation of cephalosporin treated wastewaters.¹⁰⁸ They reported that increasing the ultrasound frequency from 25 kHz to 45 kHz yielded an increase in the degradation efficiency from 76% to 90%. However, when the frequency was increased further to 85 kHz, the degradation performance decreased to 77%.

To understand this relationship between sonication frequency and pollutant degradation, we must first consider how the cavitation behaviour changes with frequency. With increasing frequency, the number of rarefaction and compression periods within a given unit of time increases. This ultimately yields a greater number of bubbles, and a greater number of bubble collapses. However, the resonant radius of the bubble (i.e. the radius at which the instability of the bubble leads to collapse) becomes smaller with increasing frequency as the rarefaction/compression cycles are shorter; this is described by the expression below (equation 1.17):¹⁰⁹

$$R_r \approx 3.28 f^{-1} \quad (1.17)$$

Where R_r is the resonant radius and f^{-1} is frequency: it is clear from the equation above that the two experimental parameters are inversely related. Kim *et. al.* postulated that as frequency is increased so too does the number of cavitation bubbles being generated; this in turn leads to an increase in degradation performance.¹⁰¹ This increase in cavitations also results in more hydroxyl radicals being produced. Furthermore, the more rapid rarefaction/compression cycles inhibit the recombination of these radicals to hydrogen peroxide.^{101,110} As the applied acoustic frequency is increased, this trend continues until an inflection point when degradation performance worsens. When the frequency reaches this range a greater number of bubbles and cavitations are still being produced, however, the resonant radius of these bubbles is smaller, and so their resulting collapses are lower in energy. Eventually the intensity of the cavitation event will be weakened such that radical production, and thus degradation performance, is inhibited.¹⁰⁹ With this in mind, the importance of identifying the most effective sonication frequency is greatly important when optimising a sonoelectrochemical degradation strategy.

Another important parameter in applied sonication is power, which is a measure of energy per unit of time that is transmitted from the sonicator to the liquid. The power of the applied

sonication determines the acoustic intensity at any given point in the liquid; this intensity can be described by the following function:¹¹¹

$$I_A = \frac{P_a^2}{2\rho c} \quad (1.18)$$

Where I_A is the acoustic intensity, ρ is the density of the liquid medium, c is the speed of sound in the liquid, and P_a is the amplitude of the sound wave. As can be seen from equation 1.18 the acoustic power is directly related to the amplitude of the applied sonication and is only inhibited by the ρc value which can be considered an intrinsic acoustic impedance offered by the liquid medium. Studies have found that an increase in power during sonoelectrochemical pollutant removal typically promotes the process. Using a combined US-EC approach to investigate the degradation of ibuprofen, Binota *et al.* tested power densities ranging from 40 to 100 W L⁻¹.¹¹⁰ The authors reported that the rate constants for the degradation increased with increasing power, rising to 0.034 min⁻¹. Similarly, Ren *et al.* reported an improvement of the degradation of the dye malachite green from 88 to 95% when the sonication power was increased from 100 to 300 W.¹¹² These results are attributed to a greater number of cavitations occurring at higher power densities. This brings about all the same benefits as was discussed previously, however, an additional benefit here is that an increase in power also means there is an increase in the amplitude of the applied sound wave; this has an effect on the time, temperature and pressure of the bubble collapses (equations 1.19 & 1.20).¹⁰⁹

$$R_m = \frac{4}{3\omega_a} (P_a - P_h) \left(\frac{2}{\rho P_a}\right)^{1/2} \left[1 + \frac{2}{3P_h} (P_a - P_h)\right]^{1/3} \quad (1.19)$$

$$\tau = 0.915 R_m \left(\frac{\rho}{P_m}\right)^{1/2} \left(1 + \frac{P_{vg}}{P_m}\right) \quad (1.20)$$

In the equations above R_m is maximum bubble size, ω_a is applied frequency, P_h is the hydrostatic pressure, τ is bubble collapse time and P_{vg} is the vapour pressure. In general, cavitations under higher amplitude sonication will be more violent.¹¹¹ In some cases, much like with frequency, beyond a certain limit increasing power leads to a decrease in degradation efficiency. In a publication on the degradation of methylene blue from 2014, Yang *et al.* reported this phenomena.¹¹³ In their study, the removal of the pollutant became more efficient as power was increased from 100 to 200 W, however, at 250, 300 and 350 W the TOC removal progressively decreased. Several theories have been put forward to explain this trend such as degradation of the active surface of the electrode caused by the more plentiful and intense acoustic cavitations,^{112,113} and inhibited energy transfer from the cavitation events to the liquid due to sound wave scattering caused by the greater number of gas bubbles being formed.^{114–117} It has also been postulated that at higher sonication power, formed bubbles are more likely to coalesce. The cavitations from the resulting larger bubbles are lower energy.¹⁰⁷

1.4.1.2 Sonication Source

Sonication is commonly applied to a reaction via one of two approaches; either the reaction vessel is submerged in an ultrasonic bath, or an ultrasonic horn is immersed in the reaction liquid itself (figure 1.4).

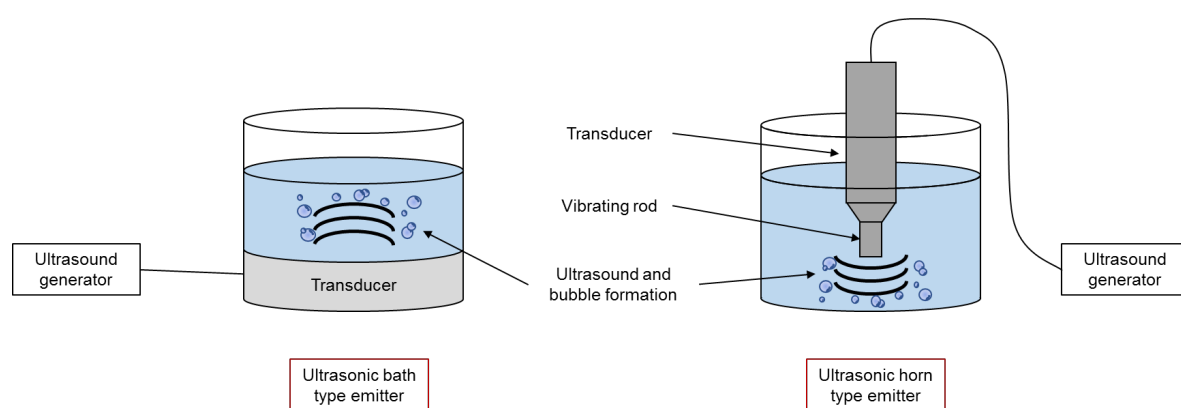


Figure 1.4: Bath vs. horn ultrasonic reactor configurations, redrawn from ref [109]

Of the two, a greater number of articles have been published using an ultrasonic bath in which ultrasound is generated throughout a liquid from a transducer fitted at the bottom of

the bath. When immersed in this bath, the reaction vessel is subject to the sonication generated by the transducer, however, as the working liquid is separated from the liquid in the bath by the vessel walls, the acoustic intensity will be weakened by sound dampening. As a result, the number of cavitations and subsequent radical production is lower in the reaction solution than in the water of the bath. A key benefit to this method though is that the ultrasonic field is better distributed across the reaction vessel, as the transducer is fitted to the base of the bath, and uses its walls as a sort of diaphragm to impart the sonication to the liquid medium.¹⁰⁹ When using an ultrasonic horn, the acoustic intensity is greatest near the head of the probe and, like with other point sources, decreases at points within the reaction that are further away from the horn due to dissipation of the ultrasonic power by the liquid medium.¹¹⁸ As such, sonoelectrochemical reactors utilising this sonication source must consider electrode positioning to best utilise the enhancements offered by ultrasound.¹¹⁹ The acoustic intensity at the tip of the horn can be determined using equation 1.21:¹²⁰

$$I_{\alpha} \approx \sin \frac{\pi}{\lambda} \left[(x^2 + r^2)^{\frac{1}{2}} - x \right] \quad (1.21)$$

Where I_{α} is the average intensity at the tip, x and r are the distance from and radius of the tip, and λ is the wavelength of the sound wave. This inhomogeneity is somewhat mitigated by the fact that ultrasonic horns typically offer much higher frequency ranges and more intense sonication than ultrasonic baths.¹⁰⁹

1.4.1.3 Electrode Materials

Many of the same design methodologies which inform electrode choice in conventional electrochemical processes hold for sonoelectrochemical experiments. In general, a model electrode will be both mechanically and chemically robust, have high electrical conductivity and selectivity, and be inexpensive. Depending on the material, electrodes can be classified as active (e.g. RuO₂, IrO₂), meaning the surface of the electrode interacts significantly with hydroxyl radicals in solution leading to partial or selective oxidation of organics,^{109,119} whereas in non-active electrodes, such as boron doped diamond (BDD) or PbO₂, only a weak interaction occurs with hydroxyl radicals. In the case of non-active electrodes, the oxidation

of pollutants occurs solely as a result of hydroxyl radical reactions; in these instances complete mineralisation is generally achieved.^{109,119} Figure 1.4 depicts the mechanisms of the different routes to organic pollutant degradation that can occur when using active and non-active electrodes.¹²¹ The promoted degradation efficiencies achieved when using non-active electrodes have led them to be extensively adopted in this field, however, both classes have their own merits and shortfalls. For example, despite the high electrochemical activity and remarkable chemical and mechanical stability of the non-active electrode BDD, widespread adoption of this technology has been inhibited by its expense.¹²¹

Recently, mixed metal oxide (or dimensionally stable) electrodes have garnered significant interest from researchers in this field.^{122,123} The deposition of two or more different metal oxides (e.g. oxides of Sn, Ir, Ru, Sb) on an inert substrate (e.g. C, Ti) often results in a material with more active acidic or basic sites, an increased surface area, leading to enhanced catalytic activity and stability over its individual components. These electrodes are often classified by their surface structure; for bulk mixed metal oxide electrodes, their surface layer comprises a single coating of mixed metal oxides, whereas supported metal oxide electrodes have a multi-layered composition formed from a supporting oxide layer, a dispersion layer and an active oxide layer. Both classes have been used extensively in electrochemical and sonoelectrochemical degradation experiments with generally favourable results.^{123–127} For instance, when investigating the sonoelectrochemical degradation of the dye malachite green, Ren *et al.* observed a substantial increase in degradation efficiency when using a Ru-Ir oxide coated titanium anode over bare Ti.¹¹² When using the bulk mixed metal oxide anode, the dye was removed from the test solution by 94% whereas with titanium, this value was only 64%. A further benefit to mixed metal oxide electrodes is that their properties can be favourably modified through doping the material; several studies have demonstrated that the inclusion of a suitable dopant (e.g. Sb, Ce, Yb) causes defects in the layers of metal oxides, thus enhancing both the conductivity and catalytic performance of the material.^{123,128–130}

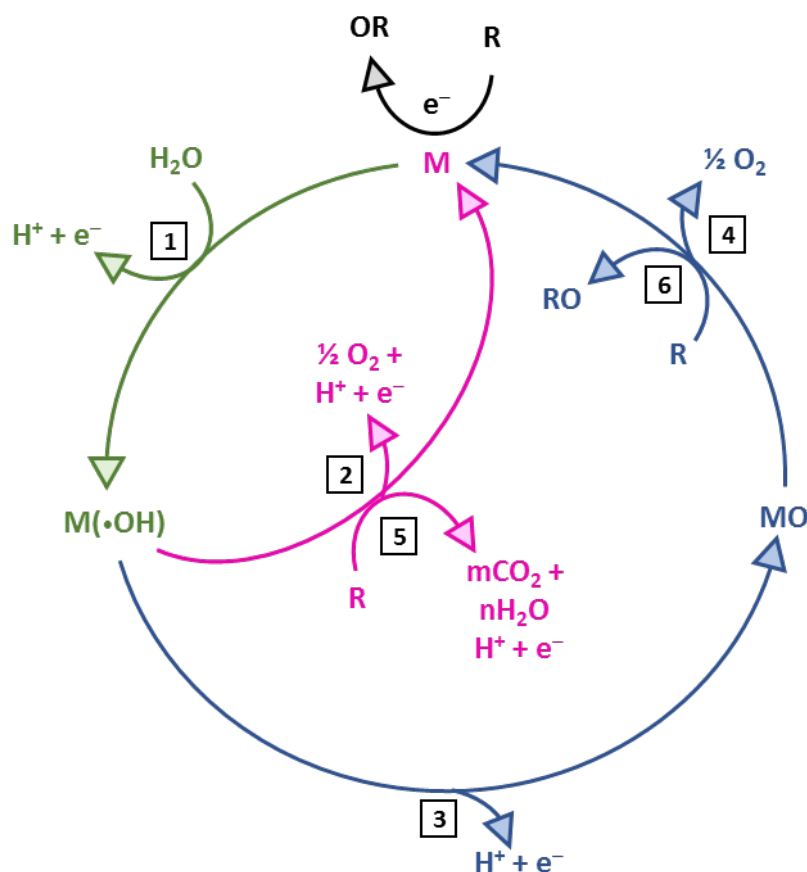
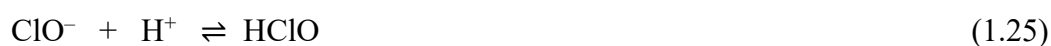


Figure 1.4: Diagram showing the electrochemical degradation mechanisms of organic pollutants on active (reactions 1, 3, 4 & 6) and non-active (reactions 1, 2 & 5) anodes. The reactions depicted are as follows: (1) generation of hydroxyl radicals (2) oxygen evolution from hydroxyl radicals (3) higher metal oxide formation (4) decomposition of metal oxide, generating oxygen (5) electrochemical conversion of the organic pollutant by hydroxyl radical and (6) electrochemical conversion of the organic pollutant via the metal oxide. Redrawn from ref [121].

1.4.1.4 Background Electrolyte

As previously discussed, one of the fundamental enhancements that sonication offers when coupled with electrochemical processes is the generation of radicals within the solution. It is prudent then, when designing a sonoelectrochemical degradation method, to fully consider the benefits that may be exploited through in-situ generation of radicals from the background electrolyte. Indeed, the addition of common salts offer not only higher electrical conductivity to the solution but, if chosen appropriately, can act as a resource from which highly oxidising species can be generated through acoustic cavitations. For example, a number of reports have demonstrated that the degradation of organic pollutants can be enhanced by the addition of

NaCl.^{131–133} A comparative study on the degradation of the dye Alizarin Red using both NaCl and Na₂SO₄ found that complete removal of the dye could be achieved in 6 mins when using the former, a result which took over 2 hours to achieve when using sodium sulfate.¹³¹ Similarly, Dionisio *et al.* achieved complete removal of methyl paraben in water containing NaCl in < 20 mins; complete removal of this pollutant was achieved in 5 hours when using Na₂SO₄.¹³³ These results are attributed to additional oxidation of pollutants via chloride species produced electrochemically and sonochemically throughout the reaction (equations 1.22 – 1.27):



In the same study by Dionisio *et al.*, despite having slower degradation rate for methyl paraben vs NaCl, it was found that complete removal of dissolved organic carbon was achieved faster when using Na₂SO₄. As with the previously discussed chloride species, the coupling of ultrasound to electrolysis in a sulfate medium yields a number of highly oxidising sulfate species through interactions with hydroxyl radicals (equations 1.12-1.15):¹³⁴



They postulated that the oxidation of the target pollutant when using NaCl occurs quickly through generation of organochlorinated intermediates. Once formed though these species

are somewhat stable and resistant to further oxidation, and so the rate of mineralisation is reduced. In the sulfate medium, the oxidising species that form attack the compound through the breaking of C-C bonds which, while slower than the chlorination of the molecule, promotes further mineralisation.¹³⁵ Furthermore, the formation of stable organochlorine species as a by-product in pollutant degradation is in some cases counterproductive, as these compounds themselves may have their own toxicity concerns.^{131–133,136}

Considering the significant effect that background electrolyte choice can have on degradation performance, it follows that the concentration of said electrolyte will also have an influence. The ionic strength and electrical conductivity of a solution will increase as the concentration of background electrolyte is increased, but there are further improvements that occur which are less intuitive. The presence of electrolyte can lead to more violent bubble collapses and promote the accumulation of the pollutant closer to these cavitation events.^{114,137–140} Taken together, these properties suggest that in most cases, increasing the concentration of background electrolyte will promote the degradation of organic pollutants, however, some key published results have found the contrary. In the case of sodium sulfate, works by done by Patidar *et al.* demonstrated that an optimum electrolyte concentration is reached which, if increased further, leads to gradual decrease in the decontamination of cosmetic wastewater.¹¹⁵ This was attributed to the formation of persulfate (equations 1.28 – 1.31) which can act as a hydroxyl radical scavenger.¹⁴¹ Similarly, Dominguez *et al.* reported that at higher doses of NaCl, higher concentrations of radical scavenging chloride species (e.g. ClO_2^- , ClO_3^- , ClO_4^-) were formed that negatively impacted the degradation efficiency.¹⁴²

The research presented above is critical to the further development of this method for real-world applications. Wastewater often contains a variety of ions which may be present in sub-optimal concentrations that can inhibit pollutant degradation. Moreover, the feasibility of this method in real wastewater merits further investigation as there may be complex interactions between the multiple different ions present (section 1.4.2.5).

1.4.2. Recent Examples of Sonoelectrochemical Wastewater Treatment

The above discussion of the fundamentals of sonoelectrochemistry and the important factors that affect the operation of sonoelectrochemical processes for the degradation of organic pollutants sets the scene for an in-depth analysis of recent examples of the application of sonoelectrochemistry for wastewater treatment (mostly from 2015 onwards). In the following, sonoelectrochemical degradation treatments are classified by pollutant type, including dyes, pharmaceuticals, pesticides and surfactants, finishing with an overview of systems that aim to decontaminate real-world wastewater streams.

Table 1.1: A summary of the reports of the sonoelectrochemical degradation of organic pollutants in water (since 2015). EC = electrochemical; US = ultrasound; TOC = total organic carbon; COD = chemical oxygen demand

Entry	Pollutant	Initial Pollutant Concentration	Electrodes	Electrolyte	Experimental Conditions	Efficiency	Reference
1	Methylene Blue	0.025 mM (~8 mg L ⁻¹)	<i>Anode:</i> Ti/Ta ₂ O ₅ -SnO ₂ <i>Cathode:</i> Ti plate	0.1 M Na ₂ SO ₄	EC - 20 mA (9.09 mA cm ⁻²), US - 850 kHz (0.186 Wcm ⁻³)	Complete decolourisation of dye solution after 45 mins. COD reduction of 85.4% after 2 hrs.	Shestakova et al. ¹⁰⁵
2	Anthroquinone C.I. Reactive Blue 49	100 mg L ⁻¹	<i>Anode:</i> Carbon <i>Cathode:</i> Pt Plate	10 M H ₂ O ₂ , H ₃ PO ₄ + NaH ₂ PO ₄ buffer	EC - 0.7 V, US - 35 kHz (150 Wcm ⁻²)	99% decolourisation was observed along with 87.8% COD reduction.	Radi et al. ¹⁴³
3	Anthroquinone C.I. Reactive Blue 49	100 mg L ⁻¹	<i>Anode:</i> Carbon <i>Cathode:</i> Pt Plate	H ₃ PO ₄ + NaH ₂ PO ₄ buffer	EC - 0.7 V, US - 35 kHz (150 Wcm ⁻²)	After 80 mins, 97.2% decolourisation and 91% COD removal.	Radi et al. ¹⁴⁴
4	Alizarin Red S	100 mg L ⁻¹	<i>Anode:</i> BDD <i>Cathode:</i> Stainless Steel	0.05 M Na ₂ SO ₄	EC - 100 mA cm ⁻² , US - 20 kHz (100 W)	Complete decolourisation of solution, and 86.07% COD removal after 3 hrs.	Zhu et al. ¹³¹
5	Naphthol Blue-Black	3.2 μM (~1.97 mg L ⁻¹)	<i>Anode:</i> BDD <i>Cathode:</i> Graphite	0.05 M (NH ₄) ₂ SO ₄ / 1 M H ₂ SO ₄	EC - 23 mA cm ⁻² , US - 37 kHz	Extent of mineralisation not determined.	Wallace et al. ¹³⁴
6	Acid Orange 7	50 mg L ⁻¹	<i>Anode:</i> Pt Sheet <i>Cathode:</i> Graphite Felt	10 mM Na ₂ SO ₄	EC - 300 mA (33.3 mA cm ⁻²), US - 20 kHz (100 W) Ozone dosage - 33 mg/L	Complete decolourisation of solution, and 88% COD removal after 1 hr.	Ghanbari et al. ¹⁴⁵
7	Methylene Blue	14.21 mg L ⁻¹	<i>Anode:</i> Zn ₃ (PO ₄) ₂ <i>Cathode:</i> Pt	0.1 M NaCl	EC - N.G., US - 40 kHz (180 W)	After 60 mins, the concentration of dye is reduced by 91 %.	Chennah et al. ¹⁴⁶
8	Allura Red	100 mg L ⁻¹	<i>Anode:</i> Ti-PbO ₂ <i>Cathode:</i> Stainless Steel	0.05 M Na ₂ SO ₄	EC - 0.75 A (18.5 mA cm ⁻²), US - 40 kHz	Complete removal of dye after 60 mins. Sonoelectrochemical method showed a 9% increase in COD removal versus the non-sonicated method.	Kacem et al. ¹⁴⁷

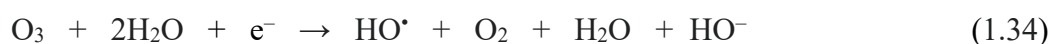
9	Erythrosine B	100 mg L ⁻¹	Anode: Ti-PbO ₂ Cathode: Stainless Steel	0.05 M Na ₂ SO ₄	EC - 0.75 A (18.5 mA cm ⁻²), US - 40 kHz	Complete removal of dye after 90 mins. Sonoelectrochemical method showed an 11% increase in COD removal versus the non-sonicated method.	Kacem et al. ¹⁴⁷
10	Malachite Green	100 mg L ⁻¹	Anode: Stainless steel, titanium, aluminum, Ru-Ir coated titanium, Ru-Ta coated titanium, graphite, brass and copper. Cathode: Graphite	15 g/L Na ₂ SO ₄	EC - 20 V, US - 25 kHz (300 W)	After 60 mins, the dye was degraded by 94.92% when using Ru-Ir coated Ti working electrode.	Ren et al. ¹¹²
11	Carbamazapine	10 mg L ⁻¹	Anode: Ti-PbO ₂ cylinder Cathode: Ti cylinder	Wastewater effluent	EC - 4.86 A (-11.6 mA cm ⁻²), US - 520 kHz (38.29 W)	Carbamezapine concentration had decreased by 93% after 177 mins. TOC and COD removal was 60% and 93%, respectively.	Tran et al. ¹⁴⁸
12	Diclofenac	50 µg L ⁻¹	Anode: BDD Cathode: BDD	30 mM Na ₂ SO ₄	EC - 7.2 V, US - 850 kHz (120 W)	After 5 mins, concentration of diclofenac had reduced by >90%.	Finkbeiner et al. ¹⁴⁹
13	p-Nitrophenol	100 mg L ⁻¹	Anode: Ti/Sb-SnO ₂ Cathode: Ti	0.05 M Na ₂ SO ₄	EC -10 V, US - 850 kHz (120 W)	After 2 hours of alternating electrode potential and ultrasonic pulses, 94.1% of p-nitrophenol was degraded.	Xie et al. ¹¹⁴
14	Cephalosporin Wastewater	COD - 326.9 mg L ⁻¹	Anode: Ru/Ir nanocoated electrode Cathode: Stainless Steel	Wastewater effluent	EC -8 mA cm ⁻² , US - 45 kHz (100 W)	94% removal efficiency for COD removal after 30 mins.	Yang et al. ¹⁵⁰
15	Chlortetracycline	10 mg L ⁻¹	Anode: Ti-PbO ₂ Cathode: Ti	Wastewater effluent	EC -3.92 A (14 mA cm ⁻²), US - 500 kHz (20 W)	Chlortetracycline concentration was reduced by 98% after 95 mins.	Tran et al. ¹⁵¹
16	Carbamazapine	10 mg L ⁻¹	Anode: Ti-PbO ₂ Cathode: Ti	0.01 M Na ₂ SO ₄	EC - 4.86 A, US - 520 kHz (38 W)	86% reduction in carbamazepine, and 80.59% mineralisation after 180 mins.	Tran et al. ¹⁰³
17	Sulfamethoxazole	20 mg L ⁻¹	Anode: Pt Cathode: Graphite	0.1 M Na ₂ SO ₄	EC - 20 mA cm ⁻² , US - 40 kHz (100 W)	Sulfamethoxazole concentration decreased by 83% after 60 mins.	Huang et al. ¹³⁹
18	Bisphenol A	1 mg L ⁻¹	Anode: BDD Cathode: BDD	30 mM Na ₂ SO ₄	EC - 20 mA cm ⁻² , US - 24 kHz (W)	>90% removal of bisphenol A after 30 mins.	Dietrich et al. ¹⁵²
19	Ibuprofen	5 mg L ⁻¹	Anode: Pt Cathode: Carbon cloth coated with Carbon black.	0.05 M Na ₂ SO ₄	EC - 0.03 A, US - 37 kHz (320 W)	84.2% removal after 60 mins using an oxygen-permeable cathode.	Darvishi Cheshmeh Soltani et al. ¹⁵³
20	Atrazine	TOC - 40.89 g L ⁻¹	Anode: BDD Cathode: Steel	Wastewater effluent	EC - 8 mA cm ⁻² , US - 24 kHz (200 W)	80% TOC removal after 30 mins, 100% after 250 min.	dos Santos et al. ¹⁵⁴
21	Piroxicam	245 µg L ⁻¹	Anode: BDD Cathode: Stainless Steel	0.1 M Na ₂ SO ₄	EC - 13 mA cm ⁻² , US - 20 kHz (14 W/L)	Complete degradation of piroxicam in <10 mins.	Kouskouki et al. ¹⁵⁵
22	Ofloxacin	2 g L ⁻¹	Anode: TiRuO ₂ Cathode: Steel	2.0 g L ⁻¹ Na ₂ SO ₄	EC - 214 A cm ⁻² , US - 33 kHz (54 W)	91.2% ofloxacin removal, 70.12% COD removal after 120 mins.	Patidar et al. ¹⁴¹

23	E.Coli	16,000 CFU 100 mL ⁻¹	Anode: BDD Cathode: Stainless Steel	Wastewater effluent	EC - 1.27 A cm ⁻² , US - 200 W	Complete disinfection in ~60 mins.	Llanos et al. ¹⁵⁶
24	Trichloroacetic Acid	0.5 mM (81.69 mg L ⁻¹)	Anode: Pt/Ti Cathode: Ti, AISI 304 stainless steel, carbon and Pb	Water	EC - 4 mA cm ⁻² or 14.3 V US - 863 kHz (0.054 W cm ⁻³)	Using Pb cathode, a degradation efficiency of 96.9% was achieved after 600 mins.	Esclapez et al. ¹⁵⁷
25	Perfluorooctanoic Acid	94 mM (38.92 g L ⁻¹)	Anode: Ti/PbO ₂ Cathode: Stainless Steel	75 mM Na ₂ SO ₄	EC - 83.64 mA cm ⁻² , US - 20 kHz	95.48% mineralisation after 90 mins.	Bonyadinejad et al. ¹⁵⁸
26	Methyl Paraben	100 mg L ⁻¹	Anode: BDD Cathode: Stainless Steel	3.0 g L ⁻¹ Na ₂ SO ₄	EC - 30 mA cm ⁻² , US - 20 kHz (75% power, instrument had a nominal power of 200 W)	Complete mineralisation of methyl paraben in less than 5 hours.	Dionisio et al. ¹³⁶
27	Thiram	100 mg L ⁻¹	Anode: BDD Cathode: Pt Net	0.05 M K ₂ SO ₄ 30% MeOH	EC - 50 mA cm ⁻² , US - 20 kHz (523 W cm ⁻²)	100% removal of the pollutant after 2 hours.	Steter et al. ¹⁵⁹
28	Formic Acid	250 mg L ⁻¹	Anode: Ti/Ta ₂ O ₅ -SnO ₂ Cathode: Ti plate	3.0 g L ⁻¹ NaCl	EC - 20 mA (~9.1 mA cm ⁻²), US - 381 kHz (0.02 W cm ⁻³)	Over 99% degradation of formic acid after 2 hours.	Shestakova et al. ¹⁶⁰
29	Pulp and effluent	4 mg L ⁻¹	Anode: Fe Cathode: Fe	Wastewater effluent	EC - 4 A dm ⁻² , US - 40 kHz (350 W)	After 4 hours, 100% decolourisation and 95% COD removal.	Asathambi et al. ¹⁶¹
30	Microcystin-LR	10 µg L ⁻¹	Anode: BDD Cathode: Stainless Steel	Wastewater effluent	EC - 6 mA cm ⁻² , US - 20 kHz (15 W)	93% degradation when process was carried out over 5 mins; 99% degradation was achieved after 10 mins.	Gao et al. ¹⁰²
31	Chlorpyrifos	900 mg L ⁻¹	Anode: Stainless Steel Cathode: Stainless Steel	2.0 g L ⁻¹ Na ₂ SO ₄	EC - 20 V, US - 40 kHz (200 W)	After 60 mins, 93.3% degradation of chlorpyrifos was observed.	Ren et al. ¹³⁷
32	Methyl Paraben in Synthetic Micellar Wastewater	DOC - 400 mg L ⁻¹	Anode: BDD Cathode: Stainless Steel	Synthetic Wastewater	EC - 30 mA cm ⁻² , US - 20 kHz	90% mineralisation was achieved in a reaction time of 8 hours.	Dionisio et al. ¹³³
33	Propyl Paraben	TOC - 7.7 mg L ⁻¹	Anode: BDD Cathode: Ti Sheet	0.1 M Na ₂ SO ₄	EC - 3.785 mA cm ⁻² , US - 20 kHz (36 W L ⁻¹)	TOC removal of 36% after 15 mins.	Frontistis ¹⁶²
34	Perfluorooctanoic Acid	60 mg L ⁻¹	Anode: Ti/SnO ₂ -Sb/Ce-PbO ₂ Cathode: Ti Sheet	50 mM Na ₂ SO ₄	EC - 5 V, US - 20 kHz (52 W)	98.7 % of the contaminant was removed after 180 mins.	Xu et al. ¹²⁸
35	4-Chlorophenol	COD - 338 mg L ⁻¹	Anode: Titanium suboxide-REM Cathode: Stainless Steel Mesh	50 mM NaClO ₄	EC - 3 V, US - 28 kHz (180 W)	After 100 successive cycles of 3 V for 40 mins, 87.81%-88.95% COD removal was maintained.	Teng et al. ¹⁶³
36	Wastewater Sludge	SCOD - 37.6 mg L ⁻¹	TiPbO ₂ -Fe-SS-SS electrode system	Wastewater effluent	EC - 100 A cm ⁻² , US - 40 kHz (180 W)	After 30 mins, a degree of degradation of 25.3% was achieved.	Ozyonar et al. ¹⁶⁴
37	Cosmetic Industry Wastewater	COD - 2350 mg L ⁻¹	Anode: Ti/RuO ₂ Cathode: Stainless Steel	Wastewater effluent	EC - 213 A cm ⁻² , US - 33 kHz (100 W)	80.9% COD removal efficiency after 180 mins.	Patidar et al. ¹¹⁵

1.4.2.1 Dyes

The sonoelectrochemical decomposition of methylene blue,^{105,146} anthraquinone C.I. reactive blue 49,^{143,144} naphthol blue black,¹³⁴ acid orange 7,¹⁴⁵ and malachite green¹¹² have all been investigated in recent years; in many cases near-complete removal of dye was reported (see Table 1.1). In 2018, Zhu *et al.*¹³¹ reported the degradation of Alizarin Red S using a boron doped diamond anode and a stainless steel cathode. Although a variety of conditions were tested, optimal results were achieved using an electrolyte consisting of 100 mg L⁻¹ of the dye and 0.05 M Na₂SO₄ at a pH of 4.97 and at 30 °C. Sonoelectrochemical oxidation (at a current density of 100 mA cm⁻², and 20 kHz (100 W power)) yielded complete discolouration of the solution, and >86% chemical oxygen demand removal was achieved after 3 hours. The authors used gas chromatography coupled to mass spectrometry (GC-MS) to identify some of the degradation products and assemble a possible degradation pathway. After 180 minutes of the sonoelectrochemical oxidation treatment, the main degradation product present was identified as bisphenol A, which can be mineralised to CO₂ and H₂O. The authors highlighted that many of the intermediates identified differed from the primary intermediates reported in the literature.^{165,166}

In a study published in 2020, Ghanbari *et al.*¹⁴⁵ coupled ultrasound to the electroperoxone method for the degradation of the dye acid orange 7 (AO7). The electroperoxone method refers to the in-situ electrochemical generation of peroxone (i.e. H₂O₂ and O₃), leading to the production of hydroxyl radicals. In short, oxygen is reduced at the cathode to H₂O₂, which may then react with ozone bubbled into solution, forming hydroxyl radicals.^{167,168} Additionally, hydroxyl radicals can be formed through the reduction of ozone (Equations 1.32-1.34):^{169,170}



The application of ultrasound to this process would be expected to further increase radical production, and indeed, complete discolouration and 88% mineralisation were achieved using a current of 300 mA (Pt sheet anode, graphite cathode), with sonication at 20 kHz (100 W), and an ozone dosage of 33 mL min⁻¹, at pH = 7 for 1 hour. This process was

benchmarked against several other oxidation techniques, including the purely electroperoxone method, sonication alone, ozone oxidation, and a combination of ultrasound and ozone oxidation: it was found that the ultrasound-assisted electroperoxone method provided the highest degradation rate. This study also reported a strong synergistic effect, meaning the degradation rate achieved in the combined method was greater than the sum of the results from the electrochemical and sonication techniques. The synergistic index (SI), given by equation 1.35, was found to be equal to 1.95.

$$SI = \frac{k_{\text{electroperoxone+sonication}}}{k_{\text{electroperoxone}} + k_{\text{sonication}}} \quad (1.35)$$

In both examples highlighted in this section thus far, the chosen anode materials were boron doped diamond and Pt respectively. Though undoubtedly effective for use in pollutant degradation, these materials are costly and could impede the scaling-up of such processes. Thus, recent efforts have focussed on using cheaper alternative electrodes for sonoelectrochemical dye removal. To this end, the sonoelectrochemical degradation of Allura Red AC and Erythrosine B, two food dyes, was of late investigated using a relatively low-cost Ti-PbO₂ anode. Using comparatively mild conditions (0.75 A, 40 kHz), Kacem *et al.*¹⁴⁷ achieved complete removal of Allura Red AC in 60 mins, and Erythrosine B in 90 mins. The time required to degrade the dyes was unchanged by the presence of ultrasound; however, the chemical oxygen demand removal was markedly improved by sonication (+9% for Allura Red AC, +11% for Erythrosine B) suggesting that sonication promotes complete mineralisation. Moreover, the effect of the supporting electrolyte was also established by running comparative tests with Na₂SO₄, NaCl, and Na₂CO₃; it was found that NaCl yielded the fastest degradations of each dye due to the generation of reactive chlorine species (Equations 1.22-1.27).

Significant degradation of the dyes was also achieved when using Na₂SO₄ as an electrolyte due to the known ultrasound enhanced electro-generation of sulfate radicals, which had previously been exploited by Dionisio *et al.*¹³⁶ for removal of the preservative methyl paraben from aqueous solution. More recently, a number of different anode materials were trialled for their suitability for the sonoelectrochemical degradation of malachite green.¹¹² Graphite, titanium, stainless steel, brass, copper, aluminium, iridium-tantalum-coated titanium, and ruthenium-iridium-coated titanium electrodes were all tested, using

Na_2SO_4 as a supporting electrolyte over 60 mins at an applied voltage of 20 V and sonication at 25 kHz (300 W). Considering only the materials which achieved >90% degradation of malachite green: copper and brass electrodes reacted with SO_4^{2-} ions in solution, forming copper sulfate, and thus were ill-suited over extended operation; graphite was found to corrode and fragment over the course of the experiment, necessitating further treatment before absorbance of the electrolyte could be measured; the stability of the aluminium anode was poor, and an oxidised film would form, and finally Ru-Ir coated Ti gave good performance, with no visible corrosion, thus making it the obvious choice for further experimentation. Under optimal conditions (see Table 1.1), this electrode material gave a malachite degradation efficiency approaching 95%. The authors then proposed a degradation pathway based on the identification of some intermediates; they postulated that HO_2^- ions generated at the cathode attack both tautomeric forms of the malachite green cation, as shown in Figure 1.5. A series of *N*-demethylation reactions then occur (disrupting the electron-donating properties of the nitrogen centres) before the resulting products are further oxidised.

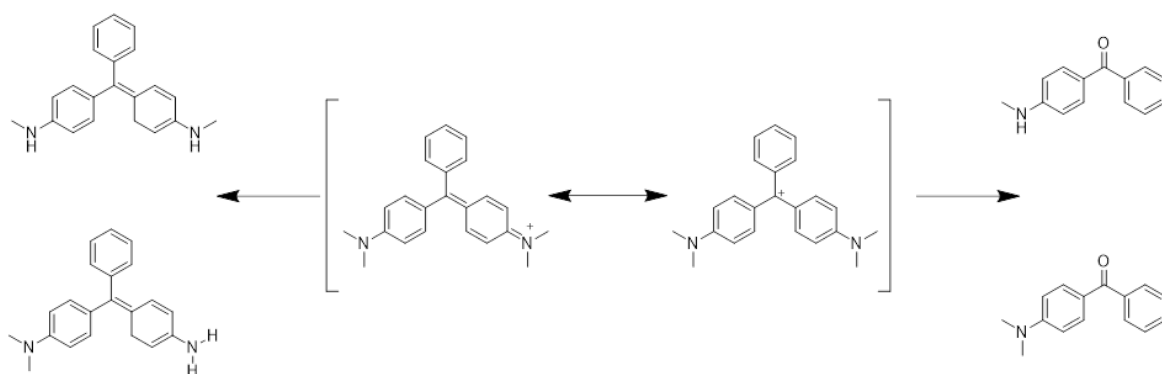


Figure 1.5: The degradation products of malachite green identified by Ren *et al.*¹¹², formed via reaction of HO_2^- with the positively-charged imine ion (left) and the carbocation (right).

1.4.2.2 Pharmaceuticals

Pharmaceuticals constitute a large and growing source of wastewater pollution. For example, somewhere between 50-90% of administered antibiotics and their primary metabolites are excreted.¹⁷¹ This has fuelled research into developing new ways to remove such pollutants from the watercourse. In 2017, Huang *et al.*¹³⁹ studied the sonoelectrochemical degradation of the antibiotic sulfamethoxazole. Using Pt and graphite as the anode and cathode

respectively in 0.1 M Na₂SO₄ at a current density of 20 mA cm⁻² under sonication at 40 kHz (100 W), an 83% degradation efficiency of sulfamethoxazole was observed after 60 mins. In comparison, under the same electrochemical conditions but in the absence of ultrasound, only 10% of the sulfamethoxazole was degraded, and using ultrasound alone resulted in only marginal degradation. Thus, a large synergy factor was evident in the combined sonoelectrochemical approach. A series of mechanistic studies were then performed to establish the primary oxidising species. The proposed mechanism (Figure 1.6) suggests that oxygen is reduced at the graphite cathode, forming superoxide (O₂⁻), which is reduced to H₂O₂ and then to HO[•]. The concurrent anodic reaction is the oxidation of H₂O and HO⁻, ultimately leading to the production of HO[•]. Hydroxyl radicals are also produced as a result of acoustic cavitation events, as discussed previously, with the sulfamethoxazole being oxidised both directly at the anode and indirectly through these radicals.

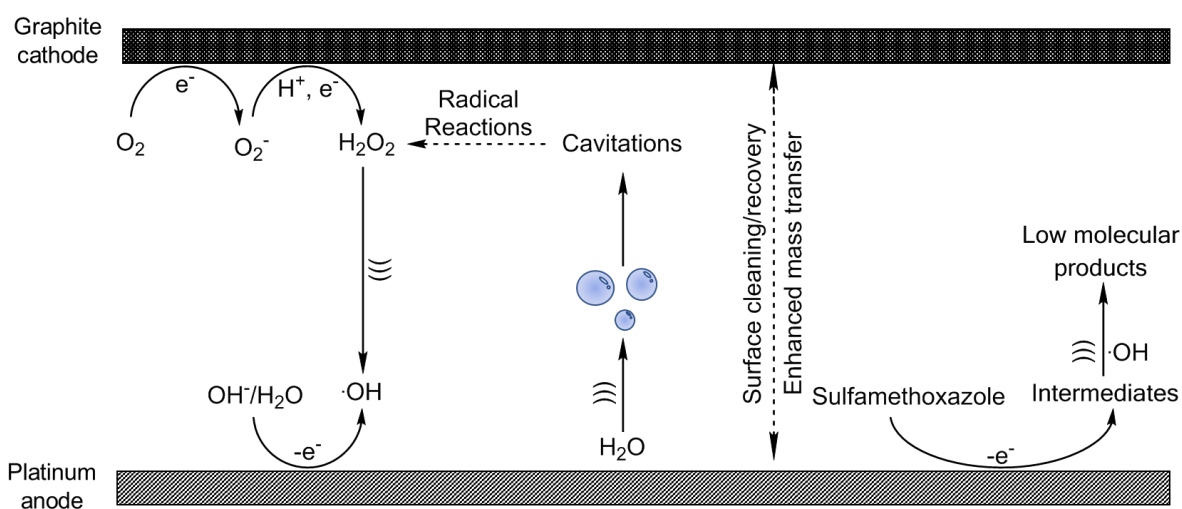


Figure 1.6: The proposed mechanism of radical generation in the degradation of sulfamethoxazole proposed by Huang *et al.*¹³⁹

The authors used high-performance liquid chromatography coupled with mass spectrometry to identify the organic intermediates hydroxylated sulfamethoxazole, 5-methyl-1,2-oxazol-3-amine, and 4-amino-hydroxybenzenesulfonic acid.¹³⁹ Using this information and examples in the literature, a possible degradation pathway was proposed (Figure 1.7). To assist in de-convoluting the degradation pathway (both in the presence and absence of ultrasound), the authors employed the same method, but using NaCl as a supporting electrolyte. The researchers determined that, in both methods, two degradation mechanisms

would occur due to oxidation from either HOCl or HO[•]. The hydroxyl radical-mediated degradation of sulfamethoxazole was found to be similar in the two experiments; however, fascinating insight was gained by comparing this with the HOCl pathway. In the absence of ultrasound, the electrooxidation of the pollutant was held to lead to the generation of complex chlorinated intermediates, some of which would couple, resulting in a number of potentially harmful dimeric and polymeric chlorinated by-products. The HOCl-mediated oxidation of sulfamethoxazole in the sonoelectrochemical system was far simpler, with only two chlorinated products detected in the degradation pathway. Should this result be observed in the degradation of other chlorinated pollutants, the authors noted it could add favour to the use of an ultrasound-assisted electrochemical degradation process over conventional methods (see also Section 1.4.1.4).^{147,150,151,156}

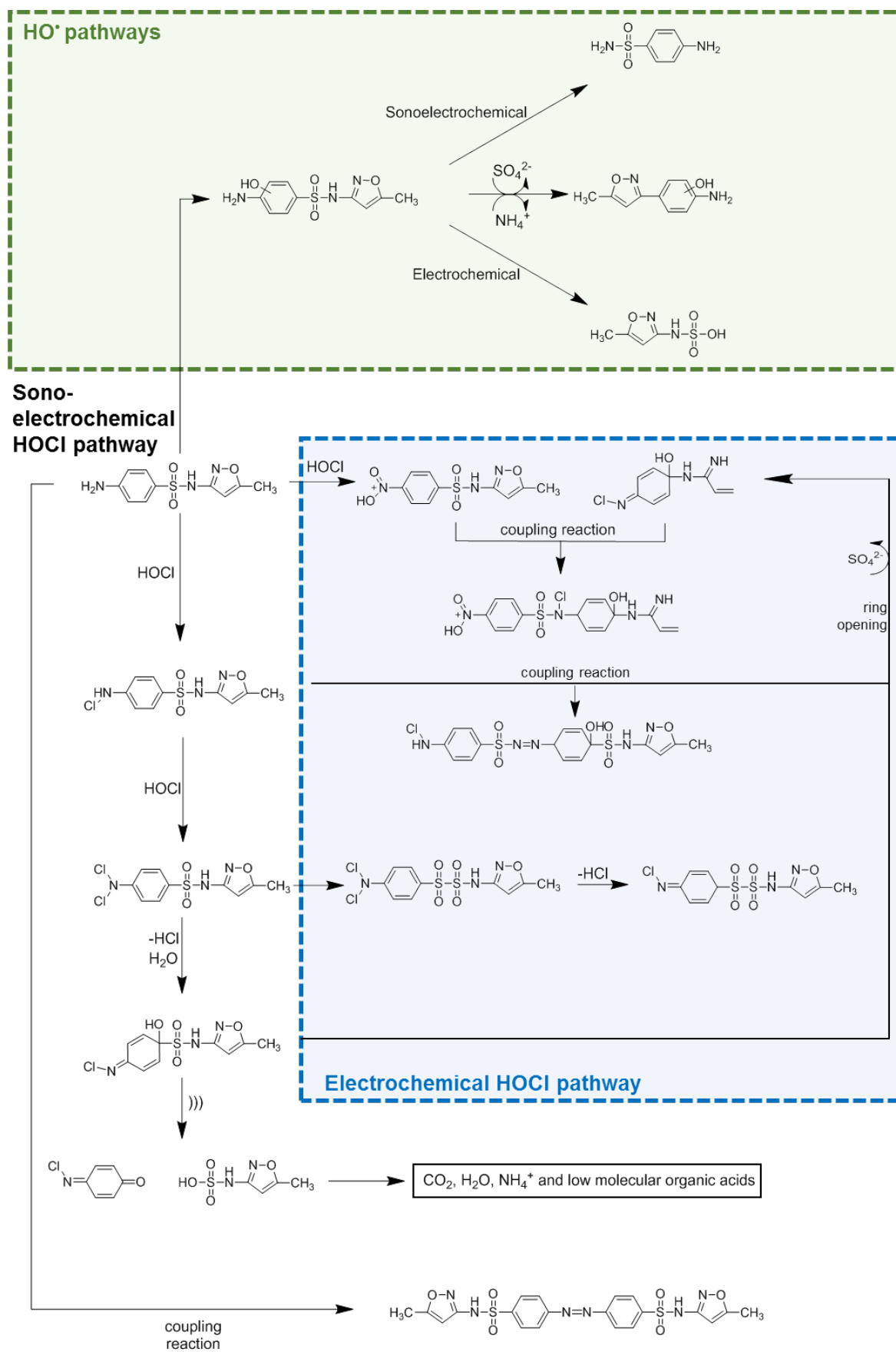


Figure 1.7: The various degradation pathways of sulfamethoxazole proposed by Huang *et al.*¹³⁹

The degradation of the anti-inflammatory drug ibuprofen was investigated by Soltani and Mashayekhi¹⁵³ using a sonoelectrochemical approach, employing a novel oxygen-permeable cathode: carbon black-coated carbon cloth. This group had previously demonstrated that the use of gas diffusion cathodes greatly promotes the electrochemical generation of H₂O₂, suggesting that such cathodes would be effective in the removal of pollutants from aqueous solution.¹⁷² A comparative degradation study of ibuprofen degradation (at a concentration of 5 mg L⁻¹) was performed over 60 mins, using a current of 0.3 A and 37 kHz sonication (320 W), in 0.05 M Na₂SO₄. Optimal ibuprofen removal was achieved when using a combined sonoelectrochemical method; this study also confirmed that the use of the novel oxygen-permeable cathode resulted in a significant increase in removal efficiency (84%) compared to that achieved with a standard carbon cloth (73%). Operating the ultrasonic bath in a pulsed mode resulted in a further increase in removal efficiency, up to nearly 89%.

Ofloxacin is an effective antibiotic, which, like other antibiotics, is bio-recalcitrant, with the potential to accumulate in wastewater as a pharmaceutical pollutant.¹⁷³ In light of this, Patidar and Srivastava¹⁴¹ studied its electrochemical degradation using a two-electrode reactor (TiRuO₂ anode, steel cathode) fitted with an ultrasonic transducer (see also Section 1.2.2). Under optimal conditions (see Table 1.1), this method was able to effectively eliminate ofloxacin (>91% ofloxacin removed, 70% chemical oxygen demand removal), and again a synergistic relationship was confirmed in the combined sonoelectrochemical approach. The authors employed radical scavengers to confirm the role of radicals in this oxidation process; perhaps unsurprisingly, it was discovered that the hydroxyl radical was the most significant contributor.

1.4.2.3 Pesticides

Since the mid-20th century there has been a massive increase in the adoption of pesticides in order to boost agricultural productivity.^{174–177} With current projections estimating that the global population may reach nearly 10 billion by 2050, it is likely that the use of these agents will only increase; however, many such pesticides can have a deleterious effect on the environment.^{176,178,179} It is against this backdrop that sonoelectrochemistry was utilised by Esclapez *et al.*¹⁵⁷ to degrade the herbicide trichloroacetic acid. Noting that the primary electrochemical degradation pathway for trichloroacetic acid consists of repeated cleavage

of the C–Cl bonds at the cathode, four different cathode materials were evaluated (Ti, AISI 304 stainless steel, carbon and Pb), and in each case the application of ultrasound was found to enhance the electrochemical degradation efficiency of trichloroacetic acid. The Pb cathode yielded the best results, with almost complete de-chlorination of trichloroacetic acid achieved after 600 min, and further tests suggested close to complete mineralisation of the acid. Although the Pb cathode was found to be the most effective for trichloroacetic acid degradation, the use of lead for water treatment processes is not ideal,¹⁸⁰ especially in the context of high frequency ultrasound, as acoustic cavitation can erode the cathode causing Pb to leach into the “treated” water. It was found that the Pb content in the water after this sonoelectrochemical process (2.1 ppm) far exceeded the maximum value permitted according to the U.S. Environmental Protection Agency (0.015 ppm). The authors argued that a mitigating factor could be that the eroded Pb particles were also found to degrade trichloroacetic acid and in turn they could be electrodeposited at the anode as PbO₂, removing them from the water. However, the requirements to meet such low Pb levels in the treated water stream will doubtless render many wary of developing sonoelectrochemical systems that are dependent on the use of lead.

Thiram is the second most widely-used contact herbicide in the world;¹⁸¹ however, it can be incredibly harmful if ingested and is a known neurotoxin.¹⁸² In 2016, it was demonstrated that thiram could be effectively degraded using a sonoelectrochemical approach with a boron doped diamond anode; under optimal conditions (see Table 1.1), complete degradation of thiram was achieved after 2 hours.¹⁵⁹ A comparative study of the electro-oxidation of thiram (both in the presence and absence of ultrasound) allowed the researchers to propose decomposition schemes under each regime. Common intermediates were identified in both pathways, such as the products formed through oxidation of the C=S groups in the thiram molecule, although it should be noted that several additional intermediates resulting from hydroxyl radical reactions were identified in the sonoelectrochemical reaction. In both approaches, the authors noted that the absence of lower molecular weight acids such as fumaric or oxalic acid was an indication that complete mineralisation of thiram was not achieved.

The removal of the pesticide chlorpyrifos via sonoelectrochemical oxidation using two stainless steel electrodes was reported in 2019.¹³⁷ Using a relatively high concentration of the pesticide (900 mg L⁻¹), a degradation of >90% was achieved after 1 hour (20 V, 40 kHz, 200 W); a synergistic factor between the electrochemical and ultrasonic inputs of 37% was also reported.

1.4.2.4 Surfactants

Surfactants are a class of molecules typified by being amphiphilic, generally with a hydrophobic tail and hydrophilic head.^{183,184} Above a certain concentration they aggregate, forming micelles in which the surfactant heads point outwards creating a hydrophilic exterior which shields a hydrophobic pocket. The benefit of this is that micelles can entrap otherwise poorly soluble organic compounds, and greatly enhance their solubility.¹⁸⁵ However, the shielding effect of these micelles has been shown to impede the oxidation of target molecules,^{186–188} and so a treatment method which can be effective in the presence of micelles is of great interest.

Building on their previous work utilising electrochemical and sonoelectrochemical methods for the degradation of methyl paraben,^{136,189,190} Dionisio et al.¹³³ investigated the effectiveness of these techniques on the treatment of a synthetic micellar-containing wastewater, with high concentrations of organic matter, mimicking the composition of wastes produced in the cosmetic industry. To understand the behaviour of the micelles under the action of an ultrasonic field, the researchers monitored particle size during electrolysis both in the presence and absence of sonication. Although it was anticipated that sonication would promote micelle degradation (as had previously been reported¹⁹¹) an initial growth in particle size was first observed under all sonication conditions. This growth was ascribed to incorporation into the micelles of gases produced during electrolysis, promoted by ultrasonic rupturing of the electro-generated bubbles. This initial growth was followed by a sharp decrease in size, suggesting that larger micelles are unstable and ultimately collapse, releasing their entrapped organic compounds into the bulk of the solution. Moreover, the extent of the initial growth was greatly dependent on the frequency of sonication. It was observed that the micellar growth was significantly higher when operating at a lower frequency (20 kHz) than at higher frequencies (1 or 10 MHz), leading the authors to speculate that the growth of the bubbles through the incorporation of gases was inhibited at higher frequencies.

The authors also reported that the application of ultrasound was effective in addressing physical features of wastewater which can negatively impact the efficiency of this process, finding that a faster depletion of turbidity and dissolution of foam was achieved. Despite this, when looking solely at the concentration of methyl paraben in the synthetic wastewater, no significant difference in its degradation was found in the presence or absence of ultrasound.

The degradation of the surfactant perfluorooctanoic acid has also been studied in some detail. In 2015, Bonyadinejad *et al.*¹⁵⁸ used a low-cost electrode setup (Ti/PbO₂ anode, Ti plate cathode) to effectively de-fluorinate perfluorooctanoic acid, achieving >95% mineralisation in 90 mins under optimal conditions (see Table 1). A synergism was observed in the combined sonoelectrochemical method, with three possible explanations: (1) ultrasound promoted the formation of sulfate radicals in the supporting electrolyte, Na₂SO₄, (2) the mass transfer enhancements brought about by sonication increased diffusion of the produced sulfate/hydroxyl radicals at the electrode surface, and/or (3) cavitation retarded the formation of a passive layer on the electrode surface. Xu *et al.*¹²⁸ compared perfluorooctanoic acid removal using Ti/SnO₂-Sb/C-PbO₂ and Ti/IrO₂-RuO₂ anodes. Significant perfluorooctanoic acid removal was only observed when using the Ti/SnO₂-Sb/C-PbO₂ anode, and the application of ultrasound improved the degradation efficiency from 89% to nearly 99%. The authors measured the hydroxyl radical production using both anodes, finding that the poor performance when using the Ti/IrO₂-RuO₂ anode was likely due to a lack of hydroxyl radical production. The significance of this radical on the degradation process was further highlighted when a HO[•] scavenger, tert-butyl alcohol, was introduced into the sonoelectrochemical experiments with Ti/SnO₂-Sb/C-PbO₂. At tert-butyl alcohol concentrations of 18 mM and 50 mM, the degradation efficiency was reduced from 98.7% to 43.9% and 25.2%, respectively. The proposed mineralisation mechanism was broadly in agreement with prior publications,^{129,192} with the first (and rate-limiting) step held to be direct oxidation of perfluorooctanoic acid at the anode. The authors postulated that the improvement offered by the combined sonoelectrochemical method was due to cavitation events causing higher temperatures and pressures near the electrode surface, thus enhancing the direct oxidation of perfluorooctanoic acid.

An interesting aside may be made at this point to consider why the effectiveness of the electrooxidation of perfluorooctanoic acid was greatly enhanced by the application of ultrasound, whereas the study by Dionisio *et al.*¹³³ observed no improvement in the degradation of methyl paraben. The main difference between these studies is that the sonoelectrochemical degradation of methyl paraben was performed in a synthetic wastewater designed to simulate a real-world waste stream, thus containing several other species including sodium dodecyl sulfate, Na₂SO₄, NaCl, H₂SO₄, CaCl₂·2H₂O, (NH₄)₂SO₄, Na₃PO₄ and MgSO₄·7H₂O. The authors pointed out that in a simple sulfate medium, it had already been shown that ultrasound enhanced the electrooxidation of methyl paraben, and sonication alone was enough to induce significant pollutant degradation.¹³⁶ In the synthetic

wastewater, no sonochemical decomposition of methyl paraben could be obtained without coupling with electrolysis. This led them to conclude that, in the more complex synthetic wastewater, the ultrasound primarily influences the reaction through its mechanical effects, as opposed to the investigations into the breakdown of perfluorooctanoic acid, which highlighted the positive role of acoustically generated radicals. It is therefore pertinent to consider that the complexity of the medium may have a significant influence on the degradation of any given target pollutant (see also Section 1.4.2.5).

1.4.2.5 Sonoelectrochemical studies performed in real wastewater

As the previous example shows, mixed electrolyte systems present an added level of complexity to the functioning and optimisation of sonoelectrochemical systems for organic pollutant degradation. These challenges are in turn only magnified when decontamination of real-world waste streams is attempted.^{107,193} For example, Yang *et al.*^{108,150} employed a sonoelectrochemical method in conjunction with a Ru/Ir nano-coated anode, finding that these electrodes provided an increase of chemical oxygen demand removal by ~24% compared to electrodes without the coating (see also Section 1.4.1.3). It was proposed that sonication enhanced the pollutant degradation process through the cleaning and activation of the anode, improving the chemical catalytic activity of the nano-coated electrodes, and increasing hydroxyl radical diffusion through the bulk solution. Moreover, the wastewater treatment was accelerated under the action of an ultrasonic field due to high concentrations of chloride, from which highly oxidizing species could be generated (e.g. $\cdot\text{Cl}$, HClO , see Equations 1.22-1.27).

The beneficial impact of the presence of chloride was similarly highlighted by Tran *et al.*¹⁵¹, who utilised a sonoelectrochemical method to treat wastewater containing the antibiotic chlortetracycline. Using a Ti-PbO₂ anode and a Ti cathode, a combined sonoelectrochemical method resulted in the degradation of up to 98% of the chlortetracycline in solution. A finding of significance was that the total organic carbon removal yield was low (37.2%), suggesting that a limited proportion of the organic material in the wastewater was completely mineralised in the process. The same researchers followed up this work by applying the same method to wastewater samples containing carbamazepine.¹⁴⁸ After performing a study to identify the optimal conditions (see Table 1.1), the authors recorded significant carbamazepine (93%), chemical oxygen demand (93%), total organic carbon (60%) and

colour removal (86%). The toxicity of the effluent was also assessed using the bioluminescent bacterium *Aliivibrio fischeri*, with the results suggesting that the wastewater was completely de-toxified after sonoelectrochemical treatment.

Sonoelectrochemical oxidation has similarly been demonstrated as an effective treatment method for municipal wastewater. Llanos *et al.*¹⁵⁶ studied the disinfection of effluent from a municipal wastewater treatment plant in Spain using a boron doped diamond anode. Following the concentration of the microorganism *E. coli*, the authors first applied ultrasound alone (200 W). It was found that after an initial decrease in population, the level of *E. coli* plateaued; they deduced that, despite prior success in sono-disinfection being reported in the literature,^{194–196} the conditions in their study were not sufficient for full disinfection of the wastewater effluent. However, when coupled with electrolysis, a synergistic effect was observed, which was ascribed to ultrasound preventing the agglomeration of the *E. coli*, making the population more susceptible to electrochemically-produced disinfectants such as hypochlorite and chloramines.

In a recent study, a hybrid electro-oxidation/coagulation treatment of sludge in municipal wastewater was examined.¹⁶⁴ Treatment and disposal of wastewater-activated sludge is expensive, and can account for up to 60% of the operational costs of a given facility.^{197–201} The study used an electrode setup in which two anodes (one Ti-PbO₂ and the other a sacrificial Fe anode) were arranged in parallel with two stainless steel cathodes (Figure 1.8); throughout the experiment the Fe anode was consumed, releasing positively-charged ions into solution.²⁰² These ions reacted with hydroxyl species generated through water reduction, to form a range of metal hydroxides and coagulants. Dissolved pollutants in the electrolyte then aggregated round these species, forming larger solid pieces which were easily separated and removed from the sample liquid as sludge. The authors evaluated the performance of the technique by considering factors such as the degree of degradation of the sludge, specific resistance to filtration, and the sludge moisture content. Applying sonication increased the degree of degradation achieved, although, crucially, the results indicated that the moisture content of the treated sludge was higher than when the process was performed in the absence of ultrasound. A consequence of this is that higher transportation and storage costs should be expected for sludge treated by this method over electro-oxidation/coagulation performed in the absence of ultrasound, which may limit its applicability.

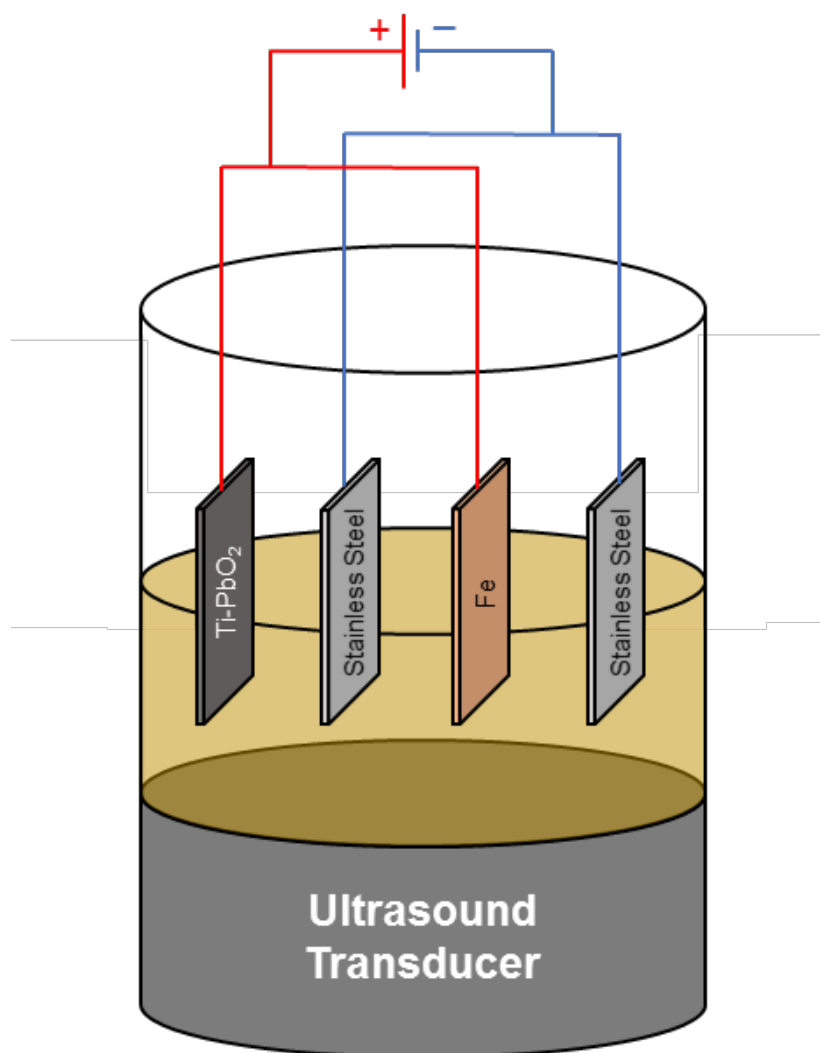


Figure 1.8: A schematic of the reactor used in the treatment of municipal wastewater sludge via ultrasound assisted electro-oxidation/coagulation, adapted from ref ¹⁶⁴.

More recently, Patidar and Srivastava ¹¹⁵ have applied this method directly to samples collected from the compensation reservoir of a factory which produces various cosmetics such as soaps, lipsticks, and shampoo. Using a Ti/RuO₂ anode with Na₂SO₄ as a supporting electrolyte, a chemical oxygen demand removal efficiency of nearly 81% was achieved using a sonoelectrochemical approach under optimal conditions (Table 1.1). The researchers tested several other methods, finding that the chemical oxygen demand removal was higher for the sonoelectrochemical method than for sonication alone (6.8%), ultraviolet light (4.6%), purely electrochemical inputs (60.2%), and a combined electrochemical-ultraviolet method (74.9%). Furthermore, it was found that the energy consumption for the same degree of mineralisation using the sonoelectrochemical process was lower than for the

electrochemical-ultraviolet approach (433.4 vs 540.5 kW per kg of chemical oxygen demand removed).

In terms of future prospects for sonoelectrochemical treatment of real-world waste streams, it should be noted that wastewater treatment systems normally integrate several different technologies in sequence.²⁰³ The same strategy is also applicable to sonoelectrochemical processes, given the fact that a standalone sonoelectrochemical process is not necessarily capable of meeting all the treatment targets (i.e. removal of all pollutants and impurities). Although studies on the integration of sonoelectrochemical water treatment processes with other treatment technologies are lacking at the current time, reports on the integration of purely electrochemical processes into water treatment trains offer some idea of the pathway ahead.^{122,204,205} For instance, electrochemical processes have been proposed as a pre-treatment step to improve the biodegradability of wastewater for subsequent biological processes and/or to help prevent membrane fouling.²⁰⁴ Alternatively, electrochemical processes could be deployed as polishing (post-treatment) steps to degrade recalcitrant pollutants that fail to be removed by conventional technologies. Sonoelectrochemical treatments could well take on such roles, especially given the synergistic effects that are often observed between the electrochemical and sonochemical inputs, provided that the technical challenges associated with reactor design (especially incorporation of the ultrasound generation system) and the impact of ultrasound on the other technologies in the treatment train can be addressed.

1.5. Conclusions

As mentioned in section 1.1, we are in the midst of a climate crisis. Throughout this chapter, we have introduced the background, main challenges, and state-of-the-art in three main subjects in which researchers have sought to address this. In chapters 3-5 of this thesis, we report our own contribution to these fields, namely: the development of an anion-exchange membrane electrolyser utilising the biopolymer lignin; the experimental validation of the efficiency of gas evolving electrolysis in reduced gravity; and finally the application of sonoelectrochemical degradation to the pharmaceutical pollutant diclofenac.

1.6 References

- 1 P. D. Noyes, M. K. McElwee, H. D. Miller, B. W. Clark, L. A. Van Tiem, K. C. Walcott, K. N. Erwin and E. D. Levin, *Environ. Int.*, 2009, **35**, 971–986.
- 2 L. Cheng, K. E. Trenberth, J. Fasullo, T. Boyer, J. Abraham and J. Zhu, *Sci. Adv.*, 2017, **3**, e1601545.
- 3 A. Shepherd, E. Ivins and E. Rignot, *Nature*, 2018, **558**, 219–222.
- 4 S. C. Doney, V. J. Fabry, R. A. Feely and J. A. Kleypas, *Ann. Rev. Mar. Sci.*, 2009, **1**, 169–192.
- 5 M. Lindner, M. Maroschek, S. Netherer, A. Kremer, A. Barbati, J. Garcia-Gonzalo, R. Seidl, S. Delzon, P. Corona, M. Kolström, M. J. Lexer and M. Marchetti, *For. Ecol. Manage.*, 2010, **259**, 698–709.
- 6 C. FN and M. MF, *J. Ecosyst. Ecography*, 2017, **07**, 5–8.
- 7 I. Roger, M. A. M. A. Shipman and M. D. M. D. Symes, *Earth-abundant catalysts for electrochemical and photoelectrochemical water splitting*, 2017, vol. 1.
- 8 S. Styring, *Faraday Discuss.*, 2012, **155**, 357–376.
- 9 N. S. Lewis and D. G. Nocera, *Powering the planet: Chemical challenges in solar energy utilization*, 2006, vol. 103.
- 10 J. S. Wallace and C. A. Ward, *Int. J. Hydrogen Energy*, 1983, **8**, 255–268.
- 11 S. A. Sherif, F. Barbir and T. N. Veziroglu, *Sol. Energy*, 2005, **78**, 647–660.
- 12 C. Xiang, K. M. Papadantonakis ab and N. S. Lewis, 2016, **3**, 169.
- 13 S. B. Lalvani, *J. Electrochem. Soc.*, 1992, **139**, L1.
- 14 N. T. Suen, S. F. Hung, Q. Quan, N. Zhang, Y. J. Xu and H. M. Chen, *Chem. Soc. Rev.*, 2017, **46**, 337–365.
- 15 L. M. Das, *Int. J. Hydrogen Energy*, 1996, **21**, 703–715.
- 16 M. Carmo, D. L. Fritz, J. Mergel and D. Stolten, *Int. J. Hydrogen Energy*, 2013, **38**, 4901–4934.
- 17 G. Gahleitner, *Int. J. Hydrogen Energy*, 2013, **38**, 2039–2061.
- 18 E. M. Sommer, L. S. Martins, J. V. C. Vargas, J. E. F. C. Gardolinski, J. C. Ordonez

- and C. E. B. Marino, *J. Power Sources*, 2012, **213**, 16–30.
- 19 J. Chi and H. Yu, *Chinese J. Catal.*, 2018, **39**, 390–394.
- 20 M. Umeda, K. Sayama, T. Maruta and M. Inoue, *Ionics (Kiel)*, 2013, **19**, 623–627.
- 21 J. Mališ, M. Paidar, T. Bystron, L. Brožová, A. Zhigunov and K. Bouzek, *Electrochim. Acta*, 2018, **262**, 264–275.
- 22 I. Vincent, A. Kruger and D. Bessarabov, *Int. J. Hydrogen Energy*, 2017, **42**, 10752–10761.
- 23 J. R. Varcoe, P. Atanassov, D. R. Dekel, A. M. Herring, M. A. Hickner, P. A. Kohl, A. R. Kucernak, W. E. Mustain, K. Nijmeijer, K. Scott, T. Xu and L. Zhuang, *Energy Environ. Sci.*, 2014, **7**, 3135–3191.
- 24 C. C. L. McCrory, S. Jung, I. M. Ferrer, S. M. Chatman, J. C. Peters and T. F. Jaramillo, *J. Am. Chem. Soc.*, 2015, **137**, 4347–4357.
- 25 M. Chandesris, V. Médeau, N. Guillet, S. Chelghoum, D. Thoby and F. Fouda-Onana, *Int. J. Hydrogen Energy*, 2015, **40**, 1353–1366.
- 26 M. Schalenbach, M. Carmo, D. L. Fritz, J. Mergel and D. Stolten, *Int. J. Hydrogen Energy*, 2013, **38**, 14921–14933.
- 27 F. Barbir, *Sol. Energy*, 2005, **78**, 661–669.
- 28 H. Janssen, J. C. Bringmann, B. Emons and V. Schroeder, *Int. J. Hydrogen Energy*, 2004, **29**, 759–770.
- 29 S. Shiva Kumar and V. Himabindu, *Mater. Sci. Energy Technol.*, 2019, **2**, 442–454.
- 30 D. Hua, J. Huang, E. Fabbri, M. Rafique and B. Song, *ChemElectroChem*, , DOI:10.1002/celec.202200999.
- 31 C. Li and J. B. Baek, *Nano Energy*, 2021, **87**, 106162.
- 32 C. Santoro, A. Lavacchi, P. Mustarelli, V. Di Noto, L. Elbaz, D. R. Dekel and F. Jaouen, *ChemSusChem*, , DOI:10.1002/cssc.202200027.
- 33 C. Li and J. B. Baek, *ACS Omega*, 2020, **5**, 31–40.
- 34 S. Y. Bae, J. Mahmood, I. Y. Jeon and J. B. Baek, *Nanoscale Horizons*, 2020, **5**, 43–56.
- 35 H. Tan, B. Tang, Y. Lu, Q. Ji, L. Lv, H. Duan, N. Li, Y. Wang, S. Feng, Z. Li, C. Wang, F. Hu, Z. Sun and W. Yan, *Nat. Commun.*, 2022, **13**, 1–9.

- 36 M. Manolova, C. Schoeberl, R. Freudenberger, C. Ellwein, J. Kerres, S. Stypka and B. Oberschachtsiek, , DOI:10.1016/j.ijhydene.2015.04.149.
- 37 R. Parsons, *Trans. Faraday Soc.*, 1958, **54**, 1053–1063.
- 38 R. Subbaraman, D. Tripkovic, K. C. Chang, D. Strmcnik, A. P. Paulikas, P. Hirunsit, M. Chan, J. Greeley, V. Stamenkovic and N. M. Markovic, *Nat. Mater.*, 2012, **11**, 550–557.
- 39 D. Pletcher and X. Li, *Int. J. Hydrogen Energy*, 2011, **36**, 15089–15104.
- 40 D. E. Brown, M. N. Mahmood, M. C. M. Man and A. K. Turner, *Electrochim. Acta*, 1984, **29**, 1551–1556.
- 41 D. Pletcher, X. Li and S. Wang, *Int. J. Hydrogen Energy*, 2012, **37**, 7429–7435.
- 42 L. Xiao, S. Zhang, J. Pan, C. Yang, M. He, L. Zhuang and J. Lu, *Energy Environ. Sci.*, 2012, **5**, 7869–7871.
- 43 A. Y. Faid, A. O. Barnett, F. Seland and S. Sunde, *Catalysts*, , DOI:10.3390/catal8120614.
- 44 I. Vincent, E. C. Lee and H. M. Kim, *Catalysts*, , DOI:10.3390/catal12050476.
- 45 E. Fabbri, A. Habereder, K. Waltar, R. Kötz and T. J. Schmidt, *Catal. Sci. Technol.*, 2014, **4**, 3800–3821.
- 46 M. Gong, Y. Li, H. Wang, Y. Liang, J. Z. Wu, J. Zhou, J. Wang, T. Regier, F. Wei and H. Dai, *J. Am. Chem. Soc.*, 2013, **135**, 8452–8455.
- 47 H. Koshikawa, H. Murase, T. Hayashi, K. Nakajima, H. Mashiko, S. Shiraishi and Y. Tsuji, *ACS Catal.*, 2020, **10**, 1886–1893.
- 48 NASA, Artemis III: NASA’s First Human Mission to the Lunar South Pole, <https://www.nasa.gov/feature/artemis-iii>.
- 49 Chinese crewed moon landing possible by 2030, says senior space figure, <https://spacenews.com/chinese-crewed-moon-landing-possible-by-2030-says-senior-space-figure/>, (accessed 22 January 2023).
- 50 H. W. Jones, *48th Int. Conf. Environ. Syst.*, 2018, 81.
- 51 M. Anand, I. A. Crawford, M. Balat-Pichelin, S. Abanades, W. Van Westrenen, G. Péraudeau, R. Jaumann and W. Seboldt, *Planet. Space Sci.*, 2012, **74**, 42–48.
- 52 D. S. McKay, G. Heiken, A. Basu, G. Blanford, S. Simon, R. Reedy, B. M. French

- and J. Papike, in *Lunar Sourcebook*, Cambridge University Press, 1991, pp. 285–356.
- 53 D. J. Lawrence, in *Encyclopedia of Lunar Science*, Springer, Cham, 2018, pp. 1–6.
- 54 M. B. Duke, B. R. Blair and J. Diaz, *Adv. Sp. Res.*, 2003, **31**, 2413–2419.
- 55 J. Carpenter, R. Fisackerly and B. Houdou, *Space Policy*, 2016, **37**, 52–57.
- 56 A. Colaprete, P. Schultz, J. Heldmann, D. Wooden, M. Shirley, K. Ennico, B. Hermalyn, W. Marshall, A. Ricco, R. C. Elphic, D. Goldstein, D. Summy, G. D. Bart, E. Asphaug, D. Korycansky, D. Landis and L. Sollitt, *Science (80-.)*, 2010, **330**, 463–468.
- 57 M. Lemelin, C. E. Morisset, M. Germain, V. Hipkin, K. Goïta and P. G. Lucey, *J. Geophys. Res. Planets*, 2013, **118**, 2582–2593.
- 58 A. H. Cutler and P. Krag, in *Lunar Bases and Space Activities of the 21st Century*, ed. W. W. Mendel, Houston, 1985, p. 559.
- 59 M. A. Gibson and C. W. Knudsen, in *Lunar Bases and Space Activities of the 21st Century*, ed. W. W. Mendel, Houston, 1985, p. 543.
- 60 R. J. Williams, in *Lunar Bases and Space Activities of the 21st Century*, ed. W. W. Mendel, Houston, 1985, p. 551.
- 61 C. Schwandt, J. A. Hamilton, D. J. Fray and I. A. Crawford, *Planet. Space Sci.*, 2012, **74**, 49–56.
- 62 S. D. Rosenberg, O. Musbah and E. E. Rice, *Lunar Planet. Sci.*, 1996, **27**, 1103.
- 63 R. J. Gustafson, E. E. Rice and B. C. White, *AIP Conf. Proc.*, 2005, **746**, 1224–1228.
- 64 O. Colson and A. Haskin, *Sp. Resour. NASA Johnson Sp. Cent.*, 1992, **3**, 195–209.
- 65 *US Pat.*, 2004.
- 66 G. Z. Chen, D. J. Fray and T. W. Farthing, *Nature*, 2000, **407**, 361–365.
- 67 T. Nohira, K. Yasuda and Y. Ito, *Nat. Mater.*, 2003, **2**, 397–401.
- 68 G. Z. Chen, E. Gordo and D. J. Fray, *Metall. Mater. Trans. B Process Metall. Mater. Process. Sci.*, 2004, **35**, 223–233.
- 69 G. Z. Chen, *Trans. Institutions Min. Metall. Sect. C Miner. Process. Extr. Metall.*, 2015, **124**, 96–105.

- 70 B. A. Lomax, M. Conti, N. Khan, N. S. Bennett, A. Y. Ganin and M. D. Symes, *Planet. Space Sci.*, 2020, **180**, 104748.
- 71 A. Taqieddin, R. Nazari, L. Rajic and A. Alshawabkeh, *J. Electrochem. Soc.*, 2017, **164**, E448–E459.
- 72 D. Zhang and K. Zeng, *Ind. Eng. Chem. Res.*, 2012, **51**, 13825–13832.
- 73 G. Sakuma, Y. Fukunaka and H. Matsushima, *Int. J. Hydrogen Energy*, 2014, **39**, 7638–7645.
- 74 M. Sakurai, Y. Sone, T. Nishida, H. Matsushima and Y. Fukunaka, *Electrochim. Acta*, 2013, **100**, 350–357.
- 75 H. Matsushima, T. Nishida, Y. Konishi, Y. Fukunaka, Y. Ito and K. Kuribayashi, *Electrochim. Acta*, 2003, **48**, 4119–4125.
- 76 D. Kiuchi, H. Matsushima, Y. Fukunaka and K. Kuribayashi, *J. Electrochem. Soc.*, 2006, **153**, E138.
- 77 H. Matsushima, D. Kiuchi, Y. Fukunaka and K. Kuribayashi, *Electrochem. commun.*, 2009, **11**, 1721–1723.
- 78 K. Brinkert, M. H. Richter, Ö. Akay, J. Liedtke, M. Giersig, K. T. Fountaine and H.-J. Lewerenz, *Nat. Commun.*, 2018, **9**, 2527.
- 79 H. Kaneko, K. Tanaka, A. Iwasaki, Y. Abe, A. Negishi and M. Kamimoto, *Electrochim. Acta*, 1993, **38**, 729–733.
- 80 Z. Derhoumi, P. Mandin, H. Roustan and R. Wüthrich, *J. Appl. Electrochem.*, 2013, **43**, 1145–1161.
- 81 P. Mandin, Z. Derhoumi, H. Roustan and W. Rolf, *Electrochim. Acta*, 2014, **128**, 248–258.
- 82 H. Guo, J. F. Zhao, F. Ye, F. Wu, C. P. Lv and C. F. Ma, *Microgravity Sci. Technol.*, 2008, **20**, 265–269.
- 83 M. Ilyas, W. Ahmad, H. Khan, S. Yousaf, M. Yasir and A. Khan, *Rev. Environ. Health*, 2019, **34**, 171–186.
- 84 P. Gautam, S. Kumar and S. Lokhandwala, *J. Clean. Prod.*, 2019, 237.
- 85 J. J. Rueda-Marquez, I. Levchuk, P. Fernández Ibañez and M. Sillanpää, *J. Clean. Prod.*, 2020, 258.

- 86 R. Ji, J. Chen, T. Liu, X. Zhou and Y. Zhang, *Chinese Chem. Lett.*, 2021.
- 87 R. Y. Krishnan, S. Manikandan, R. Subbaiya, M. Biruntha, M. Govarthan and N. Karmegam, *Environ. Technol. Innov.*, 2021, **23**, 101757.
- 88 J. Wang and S. Wang, *J. Clean. Prod.*, 2021, **315**, 128202.
- 89 D. O. Carpenter, *Rev. Environ. Health*, 2011, **26**, 61–69.
- 90 W. H. Glaze, J. W. Kang and D. H. Chapin, *Ozone Sci. Eng.*, 1987, **9**, 335–352.
- 91 T. G. Leighton, *The Acoustic Bubble*, Academic Press, London, 1994.
- 92 H. Maris and S. Balibar, *Phys. Today*, 2000, **53**, 29–34.
- 93 S. Koda, K. Tanaka, H. Sakamoto, T. Matsuoka and H. Nomura, *J. Phys. Chem.*, 2004, **108**, 11609–11612.
- 94 O. Lindström and O. Lamm, *J. Phys. Colloid Chem.*, 1951, **55**, 1139–1146.
- 95 C. Petrier, A. Jeunet, J. L. Luche and G. Reverdy, *J. Am. Chem. Soc.*, 1992, **114**, 3148–3150.
- 96 T. P. Caulier, M. Maeck and J. Reisse, *J. Org. Chem.*, 1995, **60**, 272–273.
- 97 R. G. Compton, J. C. Eklund and F. Marken, *Electroanalysis*, 1997, **9**, 509–522.
- 98 G. Cravotto and P. Cintas, *Chem. Sci.*, 2012, **3**, 295–307.
- 99 T. G. McKenzie, F. Karimi, M. Ashokkumar and G. G. Qiao, *Chem. – A Eur. J.*, 2019, **25**, 5372–5388.
- 100 R. G. Compton, J. C. Eklund, F. Marken, T. O. Rebbitt, R. P. Akkermans and D. N. Waller, *Electrochim. Acta*, 1997, **42**, 2919–2927.
- 101 K. Kim, E. Cho, B. Thokchom, M. Cui, M. Jang and J. Khim, *Ultrason. Sonochem.*, 2015, **24**, 172–177.
- 102 Y. Gao, W. Zhang, W. Wu, H. Yang, L. Li and W. Wang, in *Proceedings of the 2017 International Conference on Material Science, Energy and Environmental Engineering (MSEEE 2017)*, Atlantis Press, Paris, France, 2017.
- 103 N. Tran, P. Drogui, S. K. Brar and A. De Coninck, *Ultrason. Sonochem.*, 2017, **34**, 380–388.
- 104 S. Rondinini, C. Locatelli, A. Minguzzi and A. Vertova, eds. C. A. Martínez-Huitle, M. A. Rodrigo and O. B. T.-E. W. and W. T. Scialdone, Butterworth-Heinemann,

- 2018, pp. 3–28.
- 105 M. Shestakova, M. Vinatoru, T. J. Mason and M. Sillanpää, *Ultrason. Sonochem.*, 2015, **23**, 135–141.
- 106 M. Shestakova, M. Vinatoru, T. J. Mason, E. Iakovleva and M. Sillanpää, *J. Mol. Liq.*, 2016, **223**, 388–394.
- 107 G. Donoso, J. R. Dominguez, T. González, S. Correia and E. M. Cuerda-Correa, *Environ. Res.*, 2021, **202**, 111517.
- 108 B. Yang, J. Zuo, L. Gan, X. Yu, F. Liu, X. Tang and Y. Wang, *J. Environ. Sci. Heal. - Part A Toxic/Hazardous Subst. Environ. Eng.*, 2014, **49**, 1258–1264.
- 109 B. Thokchom, A. B. Pandit, P. Qiu, B. Park, J. Choi and J. Khim, *Ultrason. Sonochem.*, 2015, **27**, 210–234.
- 110 B. Thokchom, K. Kim, J. Park and J. Khim, *Ultrason. Sonochem.*, 2015, **22**, 429–436.
- 111 Y. G. Adewuyi, *Ind. Eng. Chem. Res.*, 2001, **40**, 4681–4715.
- 112 Q. Ren, C. Kong, Z. Chen, J. Zhou, W. Li, D. Li, Z. Cui, Y. Xue and Y. Lu, *Microchem. J.*, 2021, **164**, 106059.
- 113 B. Yang, J. Zuo, X. Tang, F. Liu, X. Yu, X. Tang, H. Jiang and L. Gan, *Ultrason. Sonochem.*, 2014, **21**, 1310–1317.
- 114 F. Xie, Y. Xu, K. Xia, C. Jia and P. Zhang, *Ultrason. Sonochem.*, 2016, **28**, 199–206.
- 115 R. Patidar and V. C. Srivastava, *J. Hazard. Mater.*, 2022, **422**, 126842.
- 116 P. Liu, Z. Wu, A. V. Abramova and G. Cravotto, *Ultrason. Sonochem.*, 2021, **74**, 105566.
- 117 S. Chakma and V. S. Moholkar, *Ind. Eng. Chem. Res.*, 2014, **53**, 6855–6865.
- 118 S. S. Rashwan, I. Dincer, A. Mohany and B. G. Pollet, *Int. J. Hydrogen Energy*, 2019, **44**, 14500–14526.
- 119 R. Patidar and V. C. Srivastava, *Crit. Rev. Environ. Sci. Technol.*, 2021, **51**, 1667–1701.
- 120 T. J. Mason and J. P. Lorimer, *Applied Sonochemistry*, Wiley, Weinheim, Germany, 2002.

- 121 Y. He, H. Lin, Z. Guo, W. Zhang, H. Li and W. Huang, *Sep. Purif. Technol.*, 2019, **212**, 802–821.
- 122 J. Qiao and Y. Xiong, *J. Water Process Eng.*, , DOI:10.1016/j.jwpe.2021.102308.
- 123 W. Wu, Z. H. Huang and T. T. Lim, *Appl. Catal. A Gen.*, 2014, **480**, 58–78.
- 124 G. Zhao, X. Cui, M. Liu, P. Li, Y. Zhang, T. Cao, H. Li, Y. Lei, L. Liu and D. Li, *Environ. Sci. Technol.*, 2009, **43**, 1480–1486.
- 125 H. Kong, H. Lu, W. Zhang, H. Lin and W. Huang, *J. Mater. Sci.*, 2012, **47**, 6709–6715.
- 126 Y. Zheng, W. Su, S. Chen, X. Wu and X. Chen, *Chem. Eng. J.*, 2011, **174**, 304–309.
- 127 H. An, H. Cui, W. Zhang, J. Zhai, Y. Qian, X. Xie and Q. Li, *Chem. Eng. J.*, 2012, **209**, 86–93.
- 128 L. Xu, X. Qian, K. Wang, C. Fang and J. Niu, *J. Clean. Prod.*, 2020, **263**, 121546.
- 129 J. Niu, H. Lin, J. Xu, H. Wu and Y. Li, *Environ. Sci. Technol.*, 2012, **46**, 10191–10198.
- 130 W. Wang, K. Wang, W. Hao, T. Zhang, Y. Liu, L. Yu and W. Li, *J. Rare Earths*, 2022, **40**, 763–771.
- 131 C. Zhu, C. Jiang, S. Chen, R. Mei, X. Wang, J. Cao, L. Ma, B. Zhou, Q. Wei, G. Ouyang, Z. Yu and K. Zhou, *Chemosphere*, 2018, **209**, 685–695.
- 132 F. E. Titchou, H. Zazou, H. Afanga, J. El Gaayda, R. Ait Akbour, P. V. Nidheesh and M. Hamdani, *J. Water Process Eng.*, 2021, **41**, 102040.
- 133 D. Dionisio, A. J. Motheo, C. Sáez, P. Cañizares and M. A. Rodrigo, *Appl. Catal. B Environ.*, 2019, **248**, 108–114.
- 134 A. G. Wallace, P. J. McHugh and M. D. Symes, *ChemPhysChem*, 2019, **20**, 3134–3140.
- 135 W. Da Oh, Z. Dong and T. T. Lim, *Appl. Catal. B Environ.*, 2016, **194**, 169–201.
- 136 D. Dionisio, A. J. Motheo, C. Sáez, P. Canizares and M. A. Rodrigo, *ChemElectroChem*, 2019, **6**, 1199–1205.
- 137 Q. Ren, C. Yin, Z. Chen, M. Cheng, Y. Ren, X. Xie, Y. Li, X. Zhao, L. Xu, H. Yang and W. Li, *Microchem. J.*, 2019, **145**, 146–153.
- 138 C. Yin, T. Ye, Y. Yu, W. Li and Q. Ren, *Microchem. J.*, 2019, **144**, 369–376.

- 139 Y. Huang, T. Zhou, X. Wu and J. Mao, *Ultrason. Sonochem.*, 2017, **38**, 735–743.
- 140 Y. Z. Ren, Z. L. Wu, M. Franke, P. Braeutigam, B. Ondruschka, D. J. Comeskey and P. M. King, *Ultrason. Sonochem.*, 2013, **20**, 715–721.
- 141 R. Patidar and V. C. Srivastava, *Chemosphere*, 2020, **257**, 127121.
- 142 C. M. Dominguez, N. Oturan, A. Romero, A. Santos and M. A. Oturan, *Water Res.*, 2018, **135**, 220–230.
- 143 M. A. Radi, N. Nasirizadeh, M. Rohani-Moghadam and M. Dehghani, *Ultrason. Sonochem.*, 2015, **27**, 609–615.
- 144 M. A. Radi, N. Nasirizadeh, M. Mirjalili and M. Rohani Moghadam, *Int. J. Environ. Sci. Technol.*, 2019, **16**, 2455–2464.
- 145 F. Ghanbari, F. Zirrahi, K. Y. A. Lin, B. Kakavandi and A. Hassani, *J. Environ. Chem. Eng.*, 2020, **8**, 104167.
- 146 A. Chennah, Z. Anfar, E. Amaterz, A. Taoufyq, B. Bakiz, L. Bazzi, F. Guinneton and A. Benlhachemi, in *Materials Today: Proceedings*, Elsevier, 2020, vol. 22, pp. 32–34.
- 147 S. Ben Kacem, S. C. Elaoud, A. M. Asensio, M. Panizza and D. Clematis, *J. Electroanal. Chem.*, 2021, **889**, 115212.
- 148 N. Tran, P. Drogui and S. K. Brar, *J. Chem. Technol. Biotechnol.*, 2015, **90**, 921–929.
- 149 P. Finkbeiner, M. Franke, F. Anschuetz, A. Ignaszak, M. Stelter and P. Braeutigam, *Chem. Eng. J.*, 2015, **273**, 214–222.
- 150 B. Yang, J. Zuo, P. Li, K. Wang, X. Yu and M. Zhang, *Chem. Eng. J.*, 2016, **287**, 30–37.
- 151 N. Tran, P. Drogui, L. Nguyen and S. K. Brar, *J. Environ. Eng.*, 2016, **142**, 04016011.
- 152 M. Dietrich, M. Franke, M. Stelter and P. Braeutigam, *Ultrason. Sonochem.*, 2017, **39**, 741–749.
- 153 R. Darvishi Cheshmeh Soltani and M. Mashayekhi, *Chemosphere*, 2018, **194**, 471–480.
- 154 E. V. dos Santos, C. Sáez, P. Cañizares, M. A. Rodrigo and C. A. Martínez-Huitle,

- J. Electrochem. Soc.*, 2018, **165**, E262–E267.
- 155 A. Kouskouki, E. Chatzisyneon, D. Mantzavinos and Z. Frontistis, *ChemElectroChem*, 2019, **6**, 841–847.
- 156 J. Llanos, S. Cotillas, P. Cañizares and M. A. Rodrigo, *Ultrason. Sonochem.*, 2015, **22**, 493–498.
- 157 M. D. Esclapez, I. Tudela, M. I. Díez-García, V. Sáez and P. Bonete, *Appl. Catal. B Environ.*, 2015, **166–167**, 66–74.
- 158 G. Bonyadinejad, M. Khosravi, A. Ebrahimi, R. Nateghi, S. M. Taghavi-Shahri and H. Mohammadi, *J. Environ. Heal. Sci. Eng.*, , DOI:10.1186/s40201-015-0232-9.
- 159 J. R. Steter, M. H. Kossuga and A. J. Motheo, *Ultrason. Sonochem.*, 2016, **28**, 21–30.
- 160 M. Shestakova, M. Vinatoru, T. J. Mason, E. Iakovleva and M. Sillanpää, *J. Mol. Liq.*, 2016, **223**, 388–394.
- 161 P. Asaithambi, A. R. A. Aziz, B. Sajjadi and W. M. A. B. W. Daud, *Environ. Sci. Pollut. Res.*, 2017, **24**, 5168–5178.
- 162 Z. Frontistis, *Int. J. Environ. Res. Public Health*, 2020, **17**, 2621.
- 163 J. Teng, S. You, F. Ma, X. Chen and N. Ren, *Ultrason. Sonochem.*, 2020, **69**, 105248.
- 164 F. Ozyonar and M. Solmaz, *J. Environ. Chem. Eng.*, 2021, **9**, 105236.
- 165 G. Liu, T. Wu, J. Zhao, H. Hidaka and N. Serpone, *Environ. Sci. Technol.*, 1999, **33**, 2081–2087.
- 166 M. Panizza and G. Cerisola, *Water Res.*, 2009, **43**, 339–344.
- 167 P. Drogui, S. Elmaleh, M. Rumeau, C. Bernard and A. Rambaud, *Water Res.*, 2001, **35**, 3235–3241.
- 168 F. C. Moreira, R. A. R. Boaventura, E. Brillas and V. J. P. Vilar, *Appl. Catal. B Environ.*, 2017, **202**, 217–261.
- 169 O. Turkay, Z. G. Ersoy and S. Barışçı, *J. Electrochem. Soc.*, 2017, **164**, E94–E102.
- 170 P. Frangos, H. Wang, W. Shen, G. Yu, S. Deng, J. Huang, B. Wang and Y. Wang, *Chem. Eng. J.*, 2016, **286**, 239–248.
- 171 M. P. Schlüsener and K. Bester, *Environ. Pollut.*, 2006, **143**, 565–571.

- 172 R. D. C. Soltani, A. Rezaee, A. R. Khataee and H. Godini, *Res. Chem. Intermed.*, 2013, **39**, 4277–4286.
- 173 V. Singh and V. C. Srivastava, *Environ. Pollut.*, 2020, **259**, 113822.
- 174 R. B. Singh, *Agric. Ecosyst. Environ.*, 2000, **82**, 97–103.
- 175 E. Brainerd and N. Menon, *J. Dev. Econ.*, 2014, **107**, 49–64.
- 176 F. E. Dayan, C. L. Cantrell and S. O. Duke, *Bioorganic Med. Chem.*, 2009, **17**, 4022–4034.
- 177 D. A. John and G. R. Babu, *Front. Sustain. Food Syst.*, 2021, **5**, 644559.
- 178 J. P. Gustafson and P. H. Raven, in *Mutation breeding, genetic diversity and crop adaptation to climate change*, CABI, Wallingford, 2021, pp. 3–9.
- 179 D. Tilman, K. G. Cassman, P. A. Matson, R. Naylor and S. Polasky, *Nature*, 2002, **418**, 671–677.
- 180 A. L. Wani, A. Ara and J. A. Usmani, *Interdiscip. Toxicol.*, 2015, **8**, 55–64.
- 181 O. M. S. Filipe, S. A. O. Santos, M. R. M. Domingues, M. M. Vidal, A. J. D. Silvestre, C. P. Neto and E. B. H. Santos, *Chemosphere*, 2013, **91**, 993–1001.
- 182 *Peer review of the pesticide risk assessment of the active substance thiram*, Wiley-Blackwell Publishing Ltd, 2017, vol. 15.
- 183 M. J. Rosen, *Surfactants and interfacial phenomena*, John Wiley & Sons, Inc, New York, NY, 1989, vol. 40.
- 184 C. N. Mulligan, R. N. Yong and B. F. Gibbs, *Eng. Geol.*, 2001, **60**, 371–380.
- 185 S. Laha, B. Tansel and A. Ussawarujikulchai, *J. Environ. Manage.*, 2009, **90**, 95–100.
- 186 C. Trelu, E. Mousset, Y. Pechaud, D. Huguenot, E. D. van Hullebusch, G. Esposito and M. A. Oturan, *J. Hazard. Mater.*, 2016, **306**, 149–174.
- 187 C. Trelu, O. Ganzenko, S. Papirio, Y. Pechaud, N. Oturan, D. Huguenot, E. D. van Hullebusch, G. Esposito and M. A. Oturan, *Chem. Eng. J.*, 2016, **306**, 588–596.
- 188 C. Trelu, N. Oturan, Y. Pechaud, E. D. van Hullebusch, G. Esposito and M. A. Oturan, *Water Res.*, 2017, **118**, 1–11.
- 189 J. R. Steter, R. S. Rocha, D. Dionísio, M. R. V. Lanza and A. J. Motheo, *Electrochim. Acta*, 2014, **117**, 127–133.

- 190 J. R. Steter, D. Dionisio, M. R. V. Lanza and A. J. Motheo, *J. Appl. Electrochem.*, 2014, **44**, 1317–1325.
- 191 E. V. Dos Santos, C. Sáez, C. A. Martínez-Huitle, P. Cañizares and M. A. Rodrigo, *Electrochem. commun.*, 2015, **55**, 26–29.
- 192 J. Niu, H. Lin, C. Gong and X. Sun, *Environ. Sci. Technol.*, 2013, **47**, 14341–14349.
- 193 D. Clematis and M. Panizza, *Curr. Opin. Electrochem.*, 2021, **30**, 100844.
- 194 D. E. . Hughes and W. L. Nyborg, *Science (80-.)*, 1962, **138**, 108–114.
- 195 S. S. Phull, A. P. Newman, J. P. Lorimer, B. Pollet and T. J. Mason, *Ultrason. Sonochem.*, 1997, **4**, 157–164.
- 196 E. Joyce, S. S. Phull, J. P. Lorimer and T. J. Mason, *Ultrason. Sonochem.*, 2003, **10**, 315–318.
- 197 A. Canales, A. Pareilleux, J. L. Rols, G. Goma and A. Huyard, *Water Sci. Technol.*, 1994, **30**, 97–106.
- 198 X. Hao, Q. Wang, Y. Cao and M. C. M. van Loosdrecht, *Water Res.*, 2010, **44**, 3993–4001.
- 199 X. Hao, Q. Wang, Y. Cao and M. C. M. van Loosdrecht, *Water Res.*, 2011, **45**, 5130–5140.
- 200 S. H. Gao, L. Fan, Z. Yuan and P. L. Bond, *Appl. Microbiol. Biotechnol.*, 2015, **99**, 2305–2312.
- 201 X. Zhou, Q. Wang, G. Jiang, P. Liu and Z. Yuan, *Bioresour. Technol.*, 2015, **185**, 416–420.
- 202 M. Y. A. Mollah, R. Schennach, J. R. Parga and D. L. Cocke, *J. Hazard. Mater.*, 2001, **84**, 29–41.
- 203 W. L. Ang, A. W. Mohammad, N. Hilal and C. P. Leo, *Desalination*, 2014, **363**, 2–18.
- 204 Z. Pan, C. Song, L. Li, H. Wang, Y. Pan, C. Wang, J. Li, T. Wang and X. Feng, *Chem. Eng. J.*, 2019, **376**, 120909.
- 205 Á. Anglada, A. Urtiaga and I. Ortiz, *J. Chem. Technol. Biotechnol.*, 2009, **84**, 1747–1755.
- 206 P. Ritesh and V. C. Srivastava, *J. Water Process Eng.*, 2020, **37**, 101378.

- 207 S. Calado Galvão de Melo, M. E. P. da Silva, M. E. B. da Silva, J. A. da Paz, C. M. B. de Menezes Barbosa, F. D. de Menezes, R. N. A. Loureiro, M. Navarro, J. Â. P. da Costa, G. F. da Silva, A. A. O. Villa and M. Vilar, *Int. J. Hydrogen Energy*, 2020, **45**, 22855–22872.

Chapter 2:

Background on Experimental Techniques

Abstract:

This chapter contains an introduction, and some background on the theory for the experimental techniques that were employed throughout this thesis.

2.1 Electrochemical Techniques

In this thesis, a variety of different electrochemical techniques were employed. By monitoring the potential, current, charge and resistance in an experiment, researchers can glean a great deal of information about both the target reactions and the materials within the electrochemical system. In the following section, the basics of electrochemistry and several of the methods used throughout the rest of the thesis will be covered.

2.1.1 Typical Electrochemical Setup

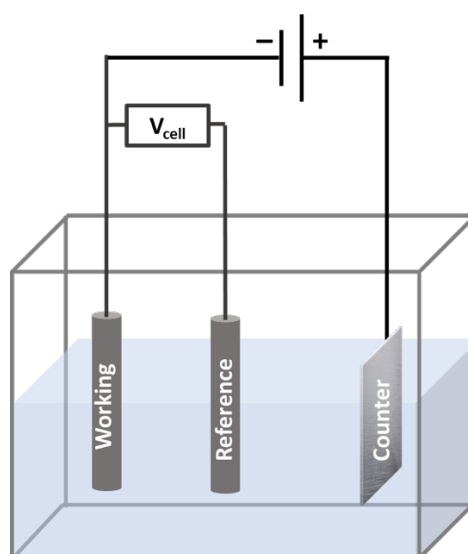


Figure 2.1: Schematic of a conventional 3-electrode cell.

In most cases, electrochemical reactions are performed using 3-electrodes; the working electrode, at which the desired reaction occurs and is investigated; the reference electrode, which contains a well-established redox couple whose half-cell potential remains constant throughout the experiment; and the counter electrode, which passes an equal but opposite current to the working (Figure 2.1). Throughout all the chapters in this thesis, the anode is denoted as the working electrode whilst the cathode is labelled as the counter, though it should be noted that in the literature these labels may be assigned differently depending on the reaction of study. For research in this field there is a great deal of flexibility in choice of working and counter electrodes, however, this choice can greatly influence the kinetics and thermodynamics of electron transfer and is therefore crucial to the success of a given experiment (see Section 1.2.3).¹ In chapter 3 of this thesis, a Pt-Ru/C anode and Pt/C cathode

were utilised in the development of a continuous-flow lignin electrolyser. In chapter 4, simple gold and copper sheet metal was cut to appropriate size and used in reduced gravity electrolysis experiments as working and counter electrodes respectively. Finally, in chapter 5, a Pt/Ti anode was used in conjunction with a Ti mesh counter.

For an experiment to proceed, it is necessary to have a closed circuit, thus it is only essential to have a working and counter electrode. In this case, an applied or measured potential is the difference in potential between the working and counter electrodes, and therefore performance of the whole cell is being evaluated as opposed to the performance of a given electrode or half-cell reaction.² For cases where this is not appropriate, a reference electrode is often employed. These electrodes utilise an internal redox system, the potential of which is constant under most conditions. During a reaction, minimal current flows through this electrode as its function is to provide a stable potential against which the potential at the working electrode can be referred. There are several examples of different reference electrodes which are available for use in both aqueous (e.g. standard hydrogen electrode, Ag/AgCl) and organic (e.g. Ag/AgNO₃) solvents, though in the case of references in organic solvents, these can more accurately be described as part of a larger class of pseudo-references. A pseudo reference differs from a true reference in that it does not have a stable thermodynamic equilibrium (i.e. its potential is not constant) however, if used in appropriate conditions, the potential of the pseudo-reference can be relatively stable; where exact potential measurements are required, an internal reference redox system (e.g. ferrocene) can be introduced.³ An Ag/AgCl reference electrode was used throughout the experiments in chapter 4 and a Pt wire pseudo-reference electrode was used in the preliminary DCF degradation experiments in chapter 5.

2.1.2 Linear Sweep and Cyclic Voltammetry

One of the most ubiquitous methods in the field of electrochemistry is voltammetry. In simple terms, this experiment measures the current response of an electrochemical system under a varying potential. Several techniques have been developed from this principle using different potential variation sequences such as cyclic, linear sweep, square-wave, and differential pulse voltammetry; the most popular of these methods being linear sweep and cyclic voltammetry. In linear sweep voltammetry, the potential is swept in one direction from a starting point, E_1 , to an end point, E_2 . In cyclic voltammetry, the applied potential follows the same path except, upon reaching E_2 , the potential is then swept in the opposite

direction; the applied potential is typically cycled between these two points several times (Figure 2.2).

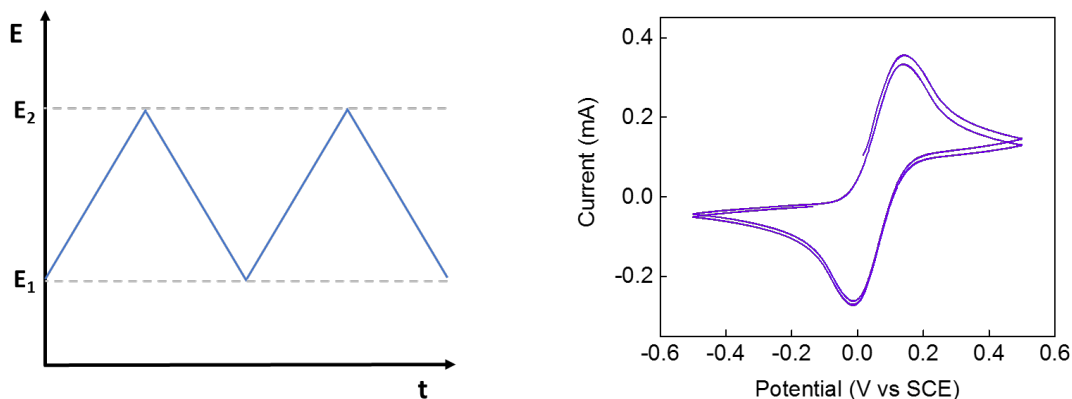


Figure 2.2: (left) potential-time graph for a typical cyclic voltammetry experiment (right) example of a voltammogram, in this case of the common redox probe ferrocene.

Cyclic voltammetry is a very useful tool for determining the redox potential at which a reaction can occur; it can also be used to electrodeposit substrates on an electrode and evaluate catalytic stability & activity.⁴⁻⁶ Furthermore, cyclic voltammetry can be used to investigate reversible reactions, which all have a characteristic line shape (Figure 2.2, right). Interpretation of the data from this technique can be used to assess if a process is fully reversible; in such cases certain criteria must be met:⁷

1. Voltage separation between the two peaks is equal to $\Delta E = \frac{59}{n} \text{ mV}$, where n is the number of electrons involved in the reaction.
2. The voltages at which each peak occur do not change with varying scan rate.
3. The ratio of the peak current in both directions is equal to one.
4. The peak currents are proportional to the square root of the scan rate.

Linear sweep voltammetry is often preferred for non-reversible reactions and can be used to assemble Tafel plots. These graphs are assembled by plotting \log_{10} of the current density vs the overpotential applied on the working electrode and can be used to glean information on an electrochemical system.⁷ For example these plots are used ubiquitously in the evaluation of heterogeneous catalysts, as researchers can very quickly determine based on the slope of

the plot how much overpotential is required to drive increases in current density. Moreover, through the use of a Tafel plot, one can calculate several important parameters such as the exchange current density (i.e. the rate of a reaction at equilibrium potential) and electron transfer coefficient, and even allows elucidation of the rate determining step.^{8,9} LSV was one of the methods used to evaluate the performance of the lignin electrolyser in chapter 3.

2.1.3 Bulk Electrolysis

Put simply, bulk electrolysis is when a condition is imposed upon the cell such that current flows over an extended period. You can categorise this electrolysis as potentiostatic, in which a potential difference is applied across the cell while the current response is measured, or galvanostatic, meaning a constant current is demanded through the circuit, and the potential requirement to meet that demand is then recorded. From both, it is possible to determine the theoretical yield from an electrochemical reaction by first determining the charge passed, Q , which is simply the product of current, I , and reaction time, t (Equation 2.1). From this value, one of Faraday's laws of electrolysis can then be used to determine theoretical yield (Equation 2.2):⁷

$$Q = It \quad (2.1)$$

$$Q = mnF \quad (2.2)$$

Where m is the theoretical number of moles of product yielded in the reaction, n is the number of electrons transferred in the experiment per mole, and F is Faraday's constant (96485 C mol⁻¹). If we consider that potential across the cell is analogous to energy input, and current is analogous to reaction rate, we can depict the merits of both approaches. With potentiostatic electrolysis you can define the energy input such that only your target reactant will be consumed; however, one is unable to control the rate of a reaction. The opposite is true in galvanostatic electrolysis where the rate of the reaction can be set and maintained, yet the system will alter the energy input to maintain that rate, and will do so using any reaction, meaning selectivity of the process could suffer. Electrolysis is used extensively in Chapters 3-5 in this work.

2.1.4 Electrical Impedance Spectroscopy

Electrical impedance spectroscopy (EIS) is one of the most useful electroanalytical techniques available to researchers to probe the resistances in their experiment. It is well established that all conductors will show some resistance to an electrical current; this value is often expressed simply using Ohm's law for resistance (Equation 2.3):

$$R = \frac{E}{I} \quad (2.3)$$

Where R is resistance, E is applied voltage and I is current. However, this law holds only for an ideal resistor which, among other things, assumes that alternating potentials and their resulting currents are in phase when passing through a resistor. In practice, there is a phase shift between the applied AC potential and current response (Figure 2.3); in EIS a small sinusoidal excitation signal (~ 5 - 15 mV) is applied,¹⁰⁻¹² whilst this phase shift is recorded at different frequencies, to give a more accurate insight into the resistance, or impedances, within an electrochemical system.^{13,14}

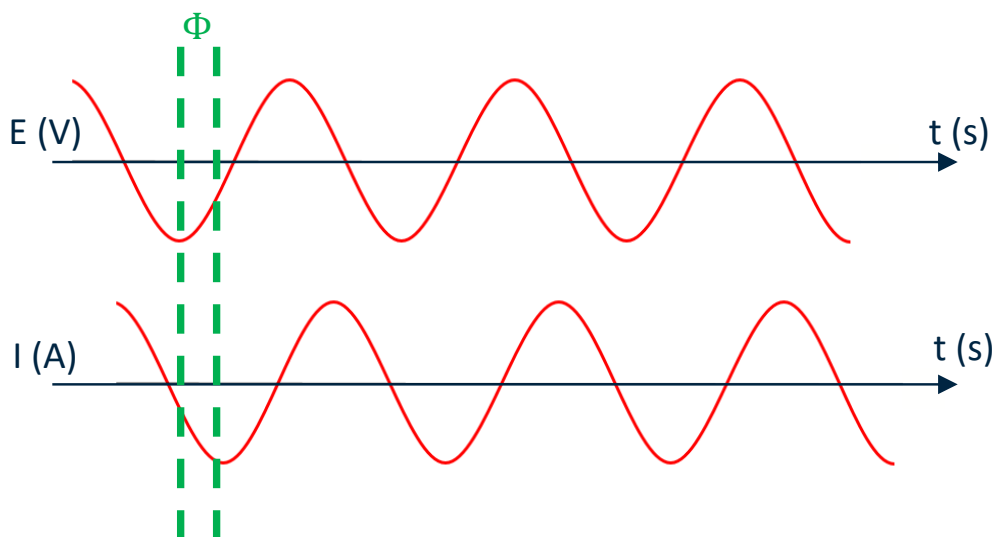


Figure 2.3: Diagram of AC excitation signal (top) and current response (bottom) through a resistor. The two signals are separated by a phase shift, ϕ .

Due to its sinusoidal nature, the potential of the excitation signal can be expressed as a function of time, t , and radial frequency, ω (Equation 2.4). Similarly, the current response can be expressed using both these terms, with consideration for the phase shift, ϕ (Equation 2.5).

$$E_t = E_0 \sin(\omega t) \quad (2.4)$$

$$I_t = I_0 \sin(\omega t + \phi) \quad (2.5)$$

Where E_t and I_t are the potential and current at time t , E_0 and I_0 are the amplitudes of their respective signals, ω is the radial frequency and ϕ is the phase shift between the two signals. Using a similar relationship to Ohm's law, we can then form an expression for impedance, Z .

$$Z_t = \frac{E_t}{I_t} = \frac{E_0 \sin(\omega t)}{I_0 \sin(\omega t + \phi)} = Z_0 \frac{\sin(\omega t)}{\sin(\omega t + \phi)} \quad (2.6)$$

Equation 2.6 defines the impedance at a given time t (Z_t), in terms of a magnitude, Z_0 , and the phase shift, ϕ . Historically, EIS measurements were interpreted by assembling a "Lissajous plot" in which the E_t signal is plotted on the x-axis and I_t is plotted on the y-axis (Figure 2.4, left).¹⁵ With the advent of modern EIS instrumentation, other forms of presenting EIS data such as Nyquist or Bode plots have become more common. In the work presented in this thesis, EIS data interpretation is done solely using Nyquist plots; for this, further manipulation of equation 2.6 must be performed. Firstly, one must consider Euler's formula which describes the relationship between trigonometric and complex exponential functions (Equation 2.7).¹⁶ We can use this relationship to alter our expressions for E_t and I_t (Equations 2.8 & 2.9), and thus impedance at any given frequency can be presented as a complex number (Equation 2.10).

$$\exp(i\phi) = \cos\phi + i\sin\phi \quad (2.7)$$

$$E_t = E_0 \exp(i\omega t) \quad (2.8)$$

$$I_t = I_0 \sin(i\omega t - \phi) \quad (2.9)$$

$$Z_\omega = \frac{E_t}{I_t} = Z_0 \exp(i\phi) = Z_0(\cos\phi + i\sin\phi) \quad (2.10)$$

As can be seen in the expression above, the impedance at a given frequency has both a real and imaginary component; in a Nyquist plot, these values are plotted on the x- and y-axis respectively (Figure 2.4, right). EIS data on a Nyquist plot has a characteristic semi-circle shape from which several values can be deduced. The high-frequency intercept of the x-axis (left side of the semi-circle) is the uncompensated resistance in the experiment (R_s); impedance can be drawn as a vector from this intercept to the “peak” of the semicircle with length $|Z|$, and the angle of this vector is the phase angle (ϕ). The difference between the high-frequency and low-frequency intercepts is the polarisation resistance (R_p), which is the sum of the resistances associated with polarising the cell, such as the energy barriers associated with the electrochemical reaction of study, and kinetic and mass transfer effects.^{14,15}

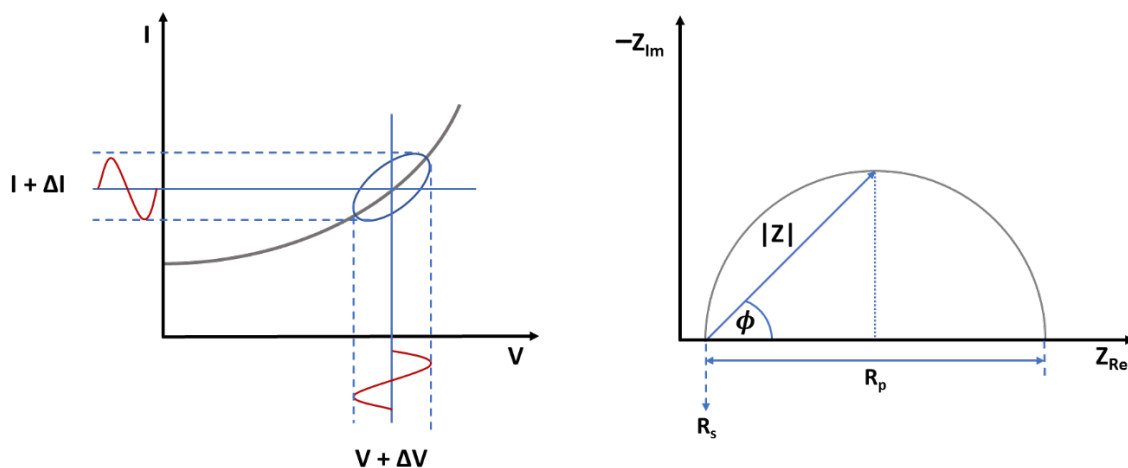


Figure 2.4: Representation of EIS data as (left) a Lissajous plot and (right) a Nyquist plot.

EIS data from electrochemical experiments is often fitted to an equivalent circuit to easier determine the individual resistances associated with the many processes in the system; these can be represented in the system as common circuit components (e.g. resistors, capacitors, inductors, etc).¹⁴ A commonly used example of such a circuit is the Randle’s circuit shown in Figure 2.5. Here R_1 corresponds to the uncompensated resistance across the cell, R_2 is

the resistance associated with polarising the cell, $C1$ is a capacitor which models the capacitive behaviour at the electrode double layer, and W is the Warburg element which accounts for the converted species being freely diffusing in solution. EIS is used to characterise the electrochemical setups in Chapters 3 & 5.

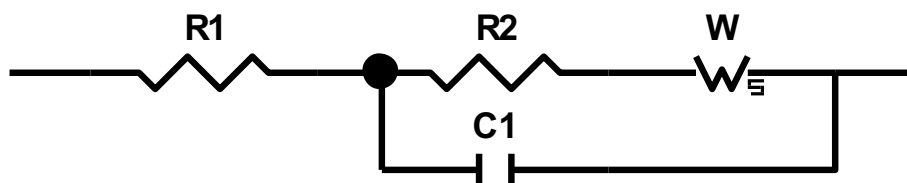


Figure 2.5: Diagram of a Randle's circuit which is commonly used as an equivalent circuit in EIS. Here, $R1$ & $R2$ are resistors, $C1$ is a capacitor and W is a Warburg element.

2.2 Spectroscopy

In addition to the previously discussed electrochemical techniques, a variety of spectroscopic techniques were employed throughout this thesis to either evaluate the success of each experiment or explain the deficiencies within our experimental setup. In the following section, a brief introduction to these methods is given.

2.2.1 UV-Vis Spectroscopy

Ultraviolet-Visible (UV-Vis) spectroscopy is an analytical technique in which the absorption or transmission of electromagnetic radiation at discrete wavelengths in a sample is probed. Sample composition and concentration will influence the absorption of light at a given wavelength, and so this technique is typically carried out by scanning this region of the electromagnetic spectrum (200-800 nm).¹⁷ UV-Vis active components absorb light at a characteristic wavelength, and so this technique can be utilised to identify functional groups or the identity of a component itself. Aside from the qualitative data available from this technique, the process is also quantitative due to the Beer-Lambert law, which states that there is a linear relationship between the concentration of an optically active species and the absorbance of its solution.¹⁸ This law, given by Equation 2.11, relates the absorbance (A), in terms of the molar extinction coefficient of the species (ϵ), with concentration (c) and the optical path length (l).

$$A = \epsilon cl \quad (2.11)$$

This molar absorption coefficient is a sample dependent property, which indicates how strongly a species or substance absorbs light at a particular wavelength. Thus, if the molar extinction is known, and the absorbance peak is correctly assigned, simple calculation of species' concentration in a sample is possible.

In Chapter 5 of this thesis, a single beam UV-Vis spectrometer was used. In these machines, light from a lamp is narrowed using a collimator and directed to a monochromator (often a prism) which splits the light according to wavelength, creating a diffracted spectrum. A mechanical slit can then selectively allow certain wavelengths of light to pass through the test sample, the intensity of light on the other side of the sample is then measured by a detector (Figure 2.6).¹⁹ UV-Vis was used briefly in chapter 5 to track the degradation of the anti-inflammatory drug, diclofenac.

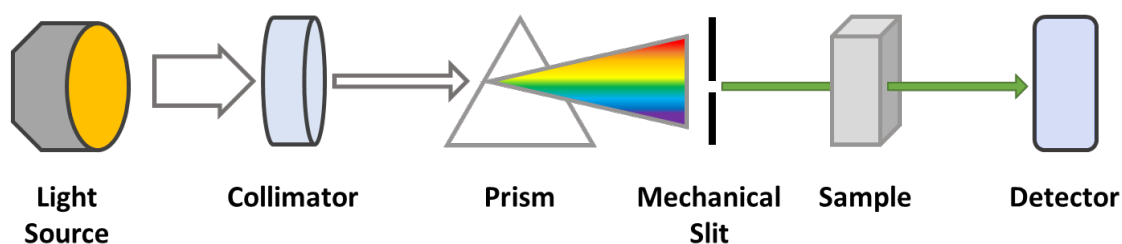


Figure 2.6: Schematic of a single beam UV-Vis Spectrometer.

2.2.2 Nuclear Magnetic Spectroscopy

Nuclear magnetic resonance (NMR) spectroscopy is a technique that probes the local environment around an atomic nucleus.²⁰ If a nucleus has an even number of mass nucleons but an unequal distribution of protons and neutrons, then the spin number will have integer values like 1 (e.g. ^2H , ^{14}N). Nuclei possessing an equal number of protons and neutrons have zero spin (e.g. ^{12}C , ^{16}O). To be detectable using NMR, a nucleus must have an inherent magnetic moment, μ , which is proportional to its spin (Equation 2.12):

$$\mu = I\gamma \frac{h}{2\pi} \quad (2.12)$$

In the above equation, γ , is the gyromagnetic ratio of the nucleus and h is Planck's constant. It is clear then that a nucleus with zero spin also has no magnetic moment and is not detectable. It should also be mentioned here that nuclei with a spin $>1/2$ have an electrical quadrupolar moment, resulting in a non-spherical distribution of charge.²¹

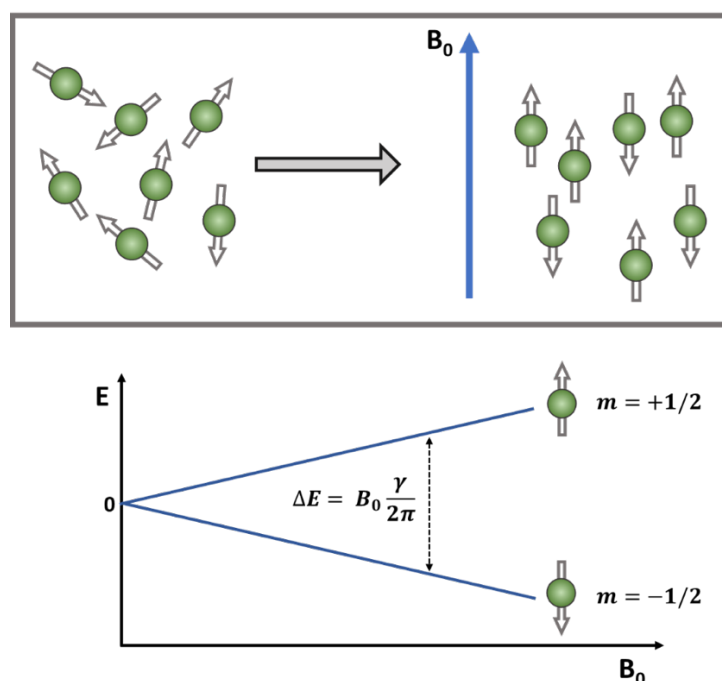


Figure 2.7: (top) Diagram showing how an $I = 1/2$ nucleus can align under the influence of a strong magnetic field, B_0 . (bottom) Representation of how the energy levels of two spin states change with increasing magnetic field strength.

The magnetic moment possessed by each nuclei results in them behaving as bar magnets which, in normal conditions, are randomly oriented. During the NMR experiment a strong magnetic field, B_0 , is applied which causes the nuclei to align and begin precessing radially around the direction of B_0 . This alignment can occur in various orientations depending on the atom's spin (Figure 2.7). For a nucleus with spin I , there exists $2I + 1$ possible alignments or "spin states" each with their own magnetic quantum number, m . For example, in the case of a $1/2$ spin nucleus such as ^1H there are two possible spin states: $m = -1/2$, where the magnetic moment is aligned with the applied field or $m = +1/2$, where the

magnetic moment opposes B_0 . In the absence of a magnetic field, these two spin states are degenerate. Once a field is applied, splitting of the spin states into discrete energy levels occurs; the difference between these levels then increases proportionally with magnetic field strength. (Figure 2.7).

The energy of a photon can be expressed as a product of its frequency, ν , and Planck's constant, h . (Equation 2.13). As previously mentioned, in the presence of a magnetic field, the nuclear magnetic moments precess around B_0 . This precession is regular and is proportional to the applied magnetic field. This precession is expressed as the Larmor frequency (Equation 2.14). In a magnetic field, the energy separation of the nuclear spin states is equal to the Larmor frequency.

$$E = h\nu \quad (2.13)$$

$$\nu = B_0 \frac{\gamma}{2\pi} \quad (2.14)$$

If a photon interacting with a nucleus has a frequency matching the Larmor frequency, a so-called resonance condition is met. In this instance, there is a strong coupling between the spin and the radiation, and absorption of the photon occurs. This can cause nucleus in the lower energy state to undergo a spin-flip to the higher energy spin state. After a given time, this nucleus returns from this excited state back to the lower energy state through relaxation.²³

Consider the sum of all the individual magnetic moments in a sample as a bulk magnetisation vector, M_0 (Figure 2.8, a). Because more nuclei adopt the lower energy spin state than the higher, M_0 will align with the direction of the applied magnetic field which we will assign as the z-axis. When the sample is irradiated with a radio frequency pulse introduced along the x-axis, many of the nuclear magnetic moments will switch spin state. Consequently, the bulk magnetisation vector will be tilted from this position and begin oscillating around the z-axis at the Larmor frequency due to angular momentum. A detector aligned along the y-axis can then record this signal as a free induction decay (Figure 2.8, b), which is converted using a Fourier transform from the time domain such that the intensity is given as a function of frequency.

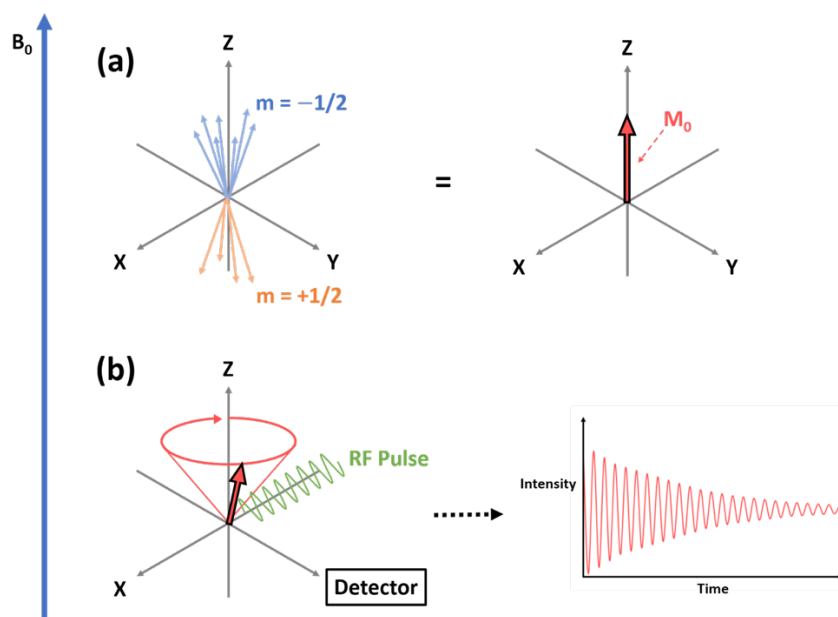


Figure 2.8: Diagram showing (a) how the magnetic moments from individual $I = \frac{1}{2}$ nuclei aligned in a magnetic field, B_0 , can be represented by their sum as a bulk magnetisation vector, M_0 (b) how a radiofrequency pulse can be used to tilt this vector from the z-axis such that it begins to precess. A detector on the y-axis can record the signal from this precession, which takes the form of a free induction decay.

This explains how a given nucleus will generate a signal throughout an NMR measurement but, based on the explanation given so far, all isotopes in a sample would give the same signal. However, as we know, this technique allows researchers to discern between the different local environments around all the target nuclei in a molecule. This is because, despite there being a single magnetic field applied, nuclei in different environments will have different effective magnetic fields. Electrons are charged particles and so will be influenced by B_0 such that they generate their own local magnetic field. The NMR target nucleus is shielded from the applied magnetic field by this local electron density; nuclei bonded to strongly electronegative atoms will have decreased electron density, and so their NMR signals will have higher frequency. Interpretation of NMR data is commonly performed by referencing the detected signals to tetramethyl silane, which acts as an internal standard. In this molecule both the protons and carbons are well shielded due to the weak electronegativity of silicon. This molecule gives one signal in both the ^{13}C and ^1H NMR which is arbitrarily defined as 0 Hz.²⁴ Finally, since the effective magnetic field strength experienced by a given nucleus will also vary depending on the magnetic field strength of the spectrometer, the frequencies are normalised as chemical shift (δ) which is expressed in

ppm. (Equation 2.15). NMR was used in chapter 5 to track the degradation of diclofenac relative to several internal standards.

$$\delta = \frac{v_{sample} - v_{reference} \text{ (Hz)}}{\text{frequency of the spectrometer (MHz)}} \quad (2.15)$$

2.2.3 Infrared Spectroscopy

The techniques discussed so far have utilised radiation from the ultraviolet & visible (UV-Vis spectroscopy) and radio-range (NMR) of the electromagnetic spectrum. Between these two, lies the infrared range (IR) which can also be used to investigate matter. The advantage that IR offers over NMR is that it provides a route to directly identify functional groups, as opposed to in NMR when these groups must be deduced through the chemical shifts of nearby atoms.²⁵ This technique detects the stretching and bending of chemical bonds, and so is particularly good at identifying functional groups such as OH, NH₂ and NO₂ due to their asymmetrical bonding. For a bond to be easily detectable by IR, it must stretch and vibrate in a way that differentiates itself from regular molecular vibration. For this reason, functional groups are highlighted by this experiment as the bonding in these groups is often much stronger/weaker than in a hydrocarbon chain and these groups often contain bonding between two atoms with very different masses.

$$E = \left(v + \frac{1}{2} \right) \frac{1}{2\pi c} \sqrt{\frac{k_f}{\mu}} \quad (2.16)$$

$$\mu = \frac{m_1 m_2}{m_1 + m_2} \quad (2.17)$$

The theoretical model behind this technique assumes two bonded atoms behave as simple harmonic oscillators. Hooke's law relates the frequency and mass of two objects attached to a spring, and it can be used in conjunction with solutions of the Schrodinger equation to give an expression for the energy of different vibrational levels of a molecule (Equation 2.16). In this equation E is the energy of the vibrational mode in wavenumbers, v is the vibrational quantum number, c is the speed of light, k_f is the force constant of the bond and μ is the

effective mass. The effective mass can be thought of as the product of two masses, m_1 & m_2 , that are forming the bond (Equation 2.17).^{23,25} The key observations from both of these equations are that stronger bonds will vibrate faster, as will bonds formed between heavy and light atoms.

According to quantum mechanics, a molecule may absorb a photon of energy to reach a vibrationally excited state. In IR analysis of a molecule, the transmittance of radiation across the IR region is monitored while detecting the absorption bands which arise from these vibrational transitions. For one of these transitions to occur, they must also be accompanied by a modulation of the molecular dipole moment; for this reason, homonuclear molecules (e.g. O_2 , N_2) are IR inactive.²⁶

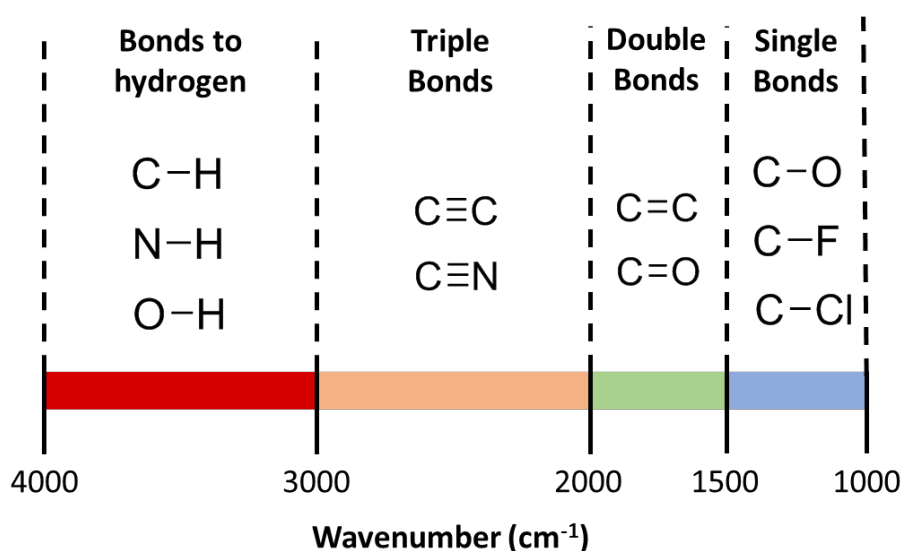


Figure 2.9: Diagram of the characteristic regions in IR spectroscopy, indicating the types of bonds detected within them. Redrawn from ref [22]

Modern IR spectroscopy is done using an interferometer, which enables frequency scanning of the IR range. The data collected here is intensity vs time; a Fourier transform, like that applied to the decay signal in NMR, is utilised to convert the recorded intensities from the time domain to the frequency domain. The spectra generated throughout an IR experiment are like UV-Vis in that the transmittance of the radiation is displayed across a range of different frequencies of light. However, rather than express this in wavelength, IR typically uses wavenumber (measured in cm^{-1}). Types of bonds fall characteristically within a wavenumber region (Figure 2.9).²⁵

Single bonds to hydrogen typically fall in the higher frequency region of the IR spectrum; this is because hydrogen is commonly an order of magnitude lighter than the atom it is bonded to. This difference in mass is so substantial that these bonds have a higher frequency than some of the strongest bonds between non-hydrogen atoms, triple bonds, which occupy the next region. The double bond region is one of the most important in the spectra as it is here that the characteristic absorption bands for many common bonding groups are found (e.g. C=O, C=C). The frequency range below this is referred to as the fingerprint region; it is here that many absorptions occur relating to various molecular bends and vibrations. Due to the sheer number of peaks in this region, it is difficult to assign individual peaks to specific vibration and bending modes of bonds; however, the spectral pattern here is specific to given molecules and so it can still be used for identification. IR-spectroscopy was used to characterise the novel anion-exchange membrane, PVIB, and help identify the mechanism by which it was decomposing in chapter 3.

2.3 Liquid Chromatography-Mass Spectrometry

One of the most useful techniques available to researchers for studying mixtures of compounds is liquid chromatography-mass spectrometry (LC-MS). This experiment combines the physical separation of mixtures offered by liquid chromatography with mass analysis. The following section will introduce the fundamentals and instrumentation of both components in this method.

2.3.1 Liquid Chromatography

Liquid chromatography is a separation technique for mixed samples, which isolates individual components in a mobile phase by the rate they move through a stationary phase.²⁷ In this method, the mobile phase is normally a liquid kept under high pressure (up to 400 bar) to maintain a steady flow rate. The stationary phase consists of chemically modified silica (e.g. silica with bonded C₁₈ alkyl groups) packed in a column capable of withstanding the high liquid pressures throughout the experiment. The choice of mobile phase is normally informed by the solubility of the sample, as complete analyte solubility is crucial. Most commonly, the mobile phase is chosen such that it is more polar than the stationary phase as separation of the components in the mixture hinges upon its interaction with both the mobile and stationary phases. However, it is not always possible to achieve sufficient separation of a mixture using a single solvent; as such, multiple-solvent eluent systems are often employed

which can be fine-tuned to optimise separation of the components of a sample.²⁷ If done successfully, certain compounds will have a characteristic retention time in specific eluent systems which, in theory, can be used for identification. The issue is that many compounds may have identical retention characteristics in a given system; as such, further analysis must be performed before unequivocal identification is possible.

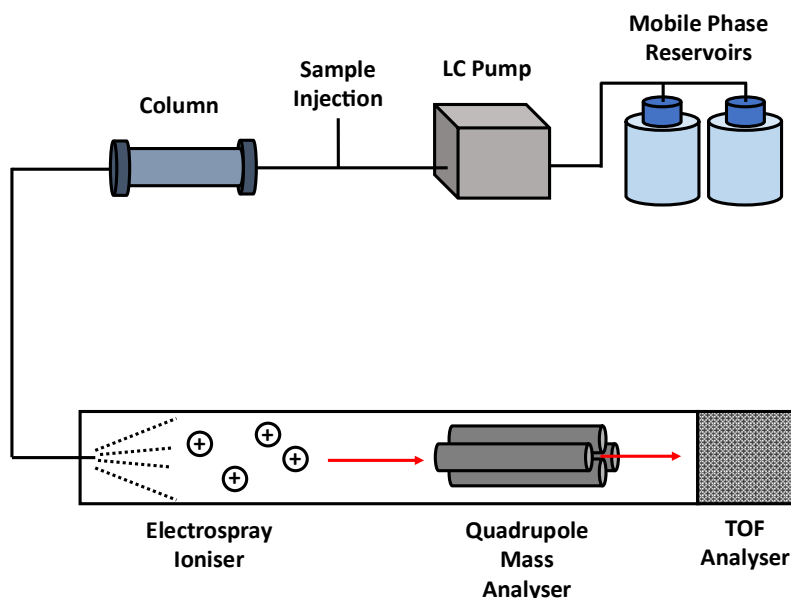


Figure 2.10: Basic schematic of a liquid chromatography-mass spectrometer.

2.3.2 Mass Spectrometry

Mass spectrometry provides information on both the structural makeup and molecular weight of an analyte. The operation of the instrument can be broken down into three main parts. Firstly, a sample is ionised; these ions are then separated out before the finally being analysed. It is important to note that, despite the name, this technique does not actually detect the mass of these ions. Rather, what is detected is the ratio of their mass to their charge (m/z).²⁸

There are several routes to ionisation of a sample. In this thesis, only electrospray ionisation (ESI) was used, so further discussion will be limited to this approach. In simple terms, ESI uses electrical charge to transfer ions from a solution into a gaseous phase. To achieve this, the liquid sample is passed continuously through a capillary needle which is maintained at a large potential difference to the surrounding chamber (2.5 – 6.0 kV).²⁹ As the liquid leaves the tip of the capillary, it forms an aerosol of charged droplets. Due to potential and pressure

gradients, the droplets make their way towards the analyser. A drying gas is employed over this stage to remove the solvent until the droplets reach a critical electric field strength, at which ions within the droplet can eject themselves in to the gaseous phase.²⁹

The separation of these produced ions is achieved by exploiting the fact that ions with a different m/z move differently through a magnetic or electrical field.²⁹ A number of different analysis instruments have been developed for use in this stage such as quadrupole, time-of-flight (TOF), and ion trap mass analyser.²⁷ Throughout this thesis, a tandem-in-space mass analysis process was implemented which combined both a quadrupole mass analyser with simultaneous TOF analysis. Hence further discussion will be limited to this approach.

A quadrupole mass analyser, as the name may suggest, consists of 4 parallel rods which are supplied a DC voltage superimposed with a radiofrequency AC voltage. Rods opposite each other are connected electrically, with the AC component between the two pairs being 180° out of phase. At each given value of these voltages, only ions of a particular m/z follow a trajectory through the rods that reaches the detector; other ions are brought to collision with the rods. By varying both the AC and DC voltages a mass spectrum can be produced.^{27,29} This method has gained popularity due to its ease of operation and ability to detect a wide mass range (10-4000 A.M.U.) at good resolution.³⁰ A TOF mass analyser works on the principle that ions produced during the ionisation phase have been supplied identical kinetic energy. Thus, the velocity of each ion is proportional to the square root of its mass, and the time taken for the ion to reach the detector is an indication of its m/z .²⁷ LC-MS was used in chapter 5 to monitor the degradation of diclofenac.

2.4 Scanning Electron Microscopy

The techniques discussed so far offer researchers methods to investigate their experiment both on a molecular and macroscopic level. However, these measurements can often be complemented and better understood by the addition of high-resolution imaging of their materials. It is in this instance that scanning electron microscopy (SEM) is of great value.

The smallest distance between two objects that is distinguishable using a light microscope is between 200-300 nm. This is because the human eye can only distinguish between two objects that are ~0.2 mm apart, and light microscopes have an effective magnification of x1000.³¹ Moreover, since the resolving power is also limited by the wavelength of the light source being used (average wavelength of visible light is 500 nm), a different source of illumination than light is required to image surfaces at a higher resolution; in the case of

SEM, electrons are used. This technique is highly tuneable and allows images to be gathered with a high resolution (1-20 nm).

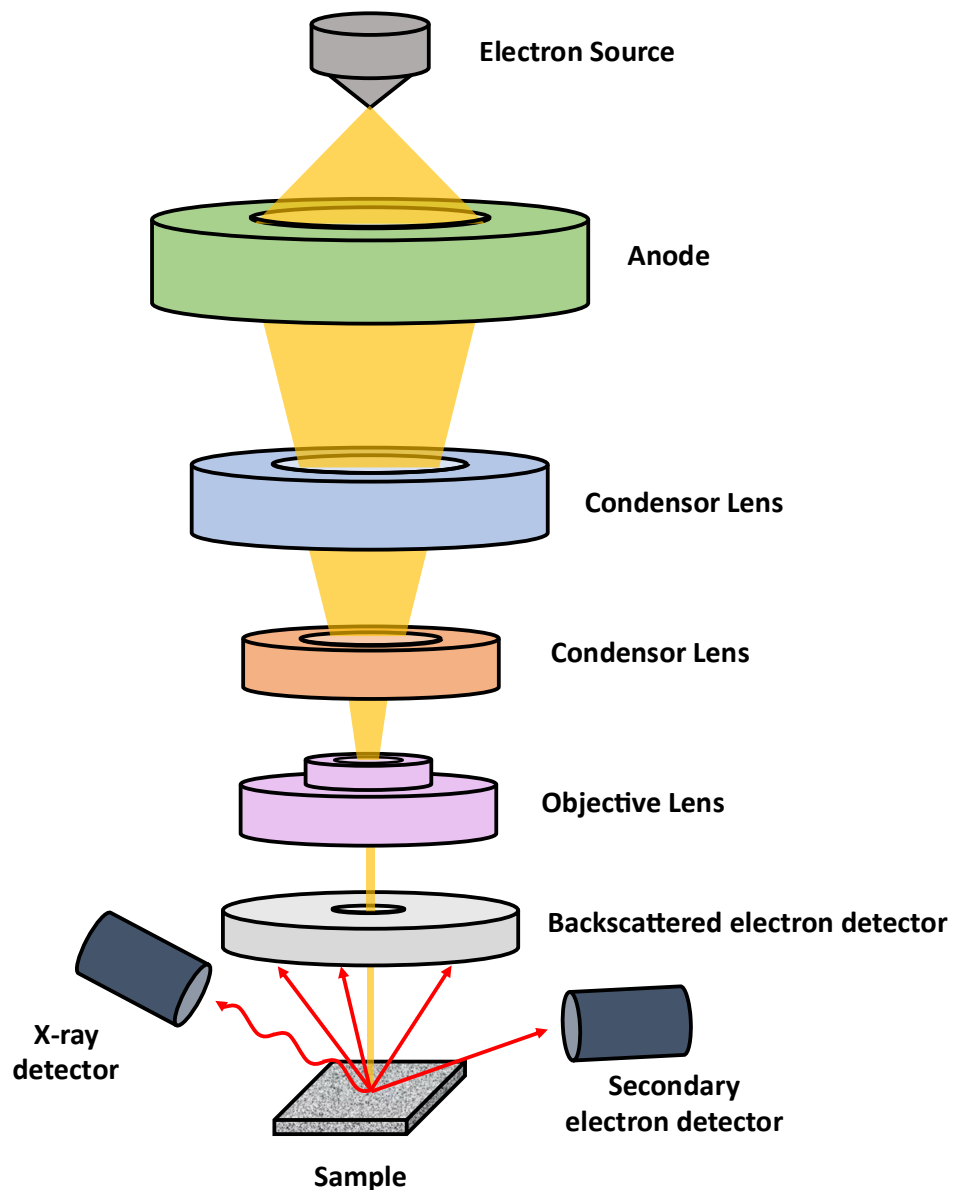


Figure 2.11: Diagram of a scanning electron microscope.

During the experiment, a small beam of electrons is generated by heating up a suitable filament (e.g. tungsten, lanthanum) in a high-vacuum column. These electrons are then accelerated by a potential difference and passed through several lenses and apertures which condense and focus the stream into a beam. At the end of a column, a magnetic device is used to direct the beam in parallel lines over a section of the subject (Figure 2.11).³² When electrons from this beam hit the surface of the sample they produce a number of signals such

as secondary electrons emitted from excited atoms in the sample, backscattered electrons originating from the beam that are reflected back after interaction with the sample, and characteristic x-rays which are collected using various detectors. The secondary electron detector provides topographical imaging of the subject, the backscattered electron detector renders compositional images and allows elements of higher atomic number to be visualised with higher contrast, and the x-ray detector is used to assemble an emission spectrum.³² The detection of these signals allows the image to be formed pixel by pixel.³³ Since the wavelength of electrons can be modified by their speed (i.e. acceleration voltage) it is possible to easily collect images within a range of resolutions using this method. Moreover, samples can be investigated using this method with no pre-treatment. This technique was used to characterise changes in the surface of the membranes used in Chapter 3 and the electrode surface in Chapter 5.

References

- 1 D. M. Heard and A. J. J. Lennox, *Angew. Chemie*, 2020, **132**, 19026–19044.
- 2 A. J. Bard and L. R. Faulkner, *Electrochemical Methods: Fundamentals and Applications*, John Wiley & Sons, New York, Second Edi., 2001.
- 3 G. Inzelt, A. Lewenstam and F. Scholz, *Handbook of Reference Electrodes*, Springer Berlin Heidelberg, Berlin, Heidelberg, 2013.
- 4 N. Elgrishi, K. J. Rountree, B. D. McCarthy, E. S. Rountree, T. T. Eisenhart and J. L. Dempsey, *J. Chem. Educ.*, 2018, **95**, 197–206.
- 5 L. C. Lopes, A. Santos and P. R. Bueno, *Sensors and Actuators Reports*, , DOI:10.1016/j.snr.2022.100087.
- 6 A. D. Stergiou and M. D. Symes, *Cell Reports Phys. Sci.*, 2022, **3**, 100914.
- 7 D. Pletcher, *A First Course in Electrode Processes*, The Royal Society of Chemistry, Cambridge, 2nd Editio., 2009.
- 8 T. Shinagawa, A. T. Garcia-Esparza and K. Takanabe, *Sci. Reports 2015 51*, 2015, **5**, 1–21.
- 9 R. Guidelli, R. G. Compton, J. M. Feliu, E. Gileadi, J. Lipkowski, W. Schmickler and S. Trasatti, *Pure Appl. Chem.*, 2014, **86**, 245–258.
- 10 T. Romero-Castañón, L. G. Arriaga and U. Cano-Castillo, *J. Power Sources*, 2003, **118**, 179–182.
- 11 T. Abe, H. Shima, K. Watanabe and Y. Ito, *J. Electrochem. Soc.*, 2003, **151**, A101.
- 12 R. F. Silva, M. De Francesco and A. Pozio, *J. Power Sources*, 2004, **134**, 18–26.
- 13 X. Yuan, H. Wang, J. Colin Sun and J. Zhang, *Int. J. Hydrogen Energy*, 2007, **32**, 4365–4380.
- 14 H. S. Magar, R. Y. A. Hassan and A. Mulchandani, *Sensors*, 2021, **21**, 6578.
- 15 D. Qu, G. Wang, J. Kafle, J. Harris, L. Crain, Z. Jin and D. Zheng, *Small Methods*, 2018, **2**, 1700342.
- 16 M. A. Moskowitz, *A Course in Complex Analysis in One Variable*, WORLD SCIENTIFIC, 2002.

- 17 R. J. Anderson, D. J. Bendell and P. W. Groundwater, *Organic Spectroscopic Analysis*, Royal Society of Chemistry, Cambridge, 2004.
- 18 Y. Guo, C. Liu, R. Ye and Q. Duan, *Appl. Sci.*, 2020, **10**, 1–18.
- 19 S. Jena, R. B. Tokas, S. Thakur and N. K. Sahoo, *SMC Bull.*, 2015, **6**, 1–9.
- 20 R. J. (Raymond J. Abraham, J. Fisher, P. Loftus and R. J. (Raymond J. Abraham, *Introduction to NMR spectroscopy*, Wiley, 1988.
- 21 J. W. Akitt and B. E. Mann, *NMR and chemistry: An introduction to modern NMR spectroscopy, fourth edition*, CRC Press, London, 2017.
- 22 A. Jerschow, *Prog. Nucl. Magn. Reson. Spectrosc.*, 2005, **46**, 63–78.
- 23 P. Atkins and J. de Paula, *Physical Chemistry*, Oxford University Press, Oxford, 10th Editi., 2014.
- 24 J. Keeler, *Understanding NMR Spectroscopy*, Wiley, Cambridge, 2005.
- 25 J. Clayden, N. Greeves and S. Warren, *Organic Chemistry*, Oxford University Press, Oxford, 2012.
- 26 B. Schrader, *Infrared and Raman Spectroscopy: Methods and Applications*, Wiley & Sons, 2008.
- 27 R. E. Ardrey, *Liquid Chromatography-Mass Spectrometry: an Introduction*, Wiley & Sons, Chichester, 2003.
- 28 G. L. Glish and R. W. Vachet, *Nat. Rev. Drug Discov.*, 2003, **2**, 140–150.
- 29 C. S. Ho, C. W. K. Lam, M. H. M. Chan, R. C. K. Cheung, L. K. Law, L. C. W. Lit, K. F. Ng, M. W. M. Suen and H. L. Tai, *Clin. Biochem. Rev.*, 2003, **24**, 3.
- 30 S. Parasuraman, A. Rao, S. Balamurugan, S. Muralidharan, K. Jayaraj Kumar and V. Vijayan, *Pharm. Methods*, 2014, **5**, 47–55.
- 31 Y. Pomeranz, *Adv. Food Res.*, 1976, **22**, 205–307.
- 32 A. Moropoulou, E. Zendri, P. Ortiz, E. T. Delegou, I. Ntoutsis, E. Balliana, J. Becerra and R. Ortiz, *Scanning*, 2019, 2019, 1–20.
- 33 E. Jensen, *Anat. Rec.*, 2012, **295**, 716–721.

Chapter 3:

Hydrogen Production by Direct Lignin Electrolysis in a Continuous Flow AEM Electrolyser

Published as “An Investigation of a (Vinylbenzyl) Trimethylammonium and N-Vinylimidazole-Substituted Poly (Vinylidene Fluoride-Co-Hexafluoropropylene) Copolymer as an Anion-Exchange Membrane in a Lignin-Oxidising Electrolyser.” P. J. McHugh, A. K. Das, A. G. Wallace, V. Kulshrestha, V. K. Shahi, M. D. Symes, Membranes 2021, 11, 425.

Acknowledgements and Declarations

I would like to thankfully acknowledge the following people for their contribution to this chapter: A. K. Das for the synthesis and initial characterisation of the membrane (section 3.3.1); A. G. Wallace for foundational work not here reported; J. Gallagher for collecting the SEM images of the membrane shown in Figure 9; V. Kulshrestha, V. K. Shahi, and M. D. Symes, who jointly conceived the idea and supervised the work.

Abstract:

Electrolysis is seen as a promising route for the production of hydrogen from water, as part of a move to a wider “hydrogen economy.” The electro-oxidation of renewable feedstocks offers an alternative anode couple to the (high-overpotential) electrochemical oxygen evolution reaction for developing low-voltage electrolyzers. Meanwhile, the exploration of new membrane materials is also important in order to try and reduce the capital costs of electrolyzers. In this work, we synthesise and characterise a previously unreported anion exchange membrane consisting of a fluorinated polymer backbone grafted with imidazole and trimethylammonium units as the ion-conducting moieties. We then investigate the use of this membrane in a lignin-oxidising electrolyser. The new membrane performs comparably to a commercially-available anion exchange membrane (Fumapem) for this purpose over short timescales (delivering current densities of 4.4 mA cm^{-2} for lignin oxidation at a cell potential of 1.2 V at 70 °C), but membrane durability was found to be a significant issue over extended testing durations. This work therefore suggests that membranes of the sort described herein might be usefully employed for lignin electrolysis applications if their mechanical robustness can be improved.

3.1 Introduction

Due to the finite supply of fossil fuels and the well-understood relationship between their widespread usage and negative effects on the global climate, there is major interest in the development and implementation of energy solutions which do not result in greenhouse gas emissions.¹ Renewables such as wind, solar and tidal all have great potential in this regard, but are limited by the fact that they are fluctuating, intermittent sources of energy. For such renewable power sources to meet global energy demand and become long-term solutions to the current energy crisis, we therefore require a suitable means of storing the energy as and when it is available.^{2,3} On this basis, the use of renewables to produce the fuel hydrogen (H_2) by electrolysis of water has long been considered as one of the most promising means of energy storage, as hydrogen has many attractive qualities as a fuel.⁴ At the time of writing, the majority of industrial-scale water electrolysis is performed using a corrosive liquid alkaline electrolyte, with an asbestos diaphragm which separates the anodic and cathodic chambers and prevents the product gases from mixing (which would otherwise form a highly explosive mixture).⁵ Although this liquid alkaline electrolyte approach is relatively inexpensive in terms of capital costs, the maximum operational current densities are limited, and the pressure in each chamber must be well managed to prevent gas cross-mixing via permeation across the membrane.⁶⁻⁸ The operational costs of liquid alkaline electrolyte cells are therefore sub-optimal.

The use of electrolysers employing solid polymer electrolytes has emerged steadily over recent decades as a route by which some of the drawbacks of liquid-phase alkaline electrolyte cells can be overcome. For example, caustic electrolytes are no longer required, many of the membranes commonly used in such cells can withstand high pressure differentials without significant gas cross-mixing occurring, and much higher operational current densities can be achieved.⁹ Proton-exchange membranes (e.g., Nafion) have been the subject of a large number of publications in this regard, and current densities $>2 \text{ A cm}^{-2}$ can be achieved,^{5,10} while the crossover rates of the gaseous products are kept low (although gas crossover is never entirely eliminated).^{8,11} In contrast to the liquid alkaline cells currently used in most large-scale industrial applications (which employ non-noble catalysts such as Ni and Co), proton-exchange membrane electrolysers require expensive noble metal catalysts and acid-resistant components. This is due to the harshly acidic environment generated at the electrode during electrolysis, and has financial implications which could impede the adoption of this technology on a commercial scale.⁸ In this regard, the development of anion-exchange membrane electrolysers could be transformational, as such

systems have the potential to work with non-noble metal catalysts, and the membranes themselves are often cheaper to produce than Nafion.^{12,13} Notwithstanding recent reports of excellent conductivity and stability,¹⁴⁻¹⁷ the conductivity of OH^- ions is generally lower in anion-exchange membranes than is the proton conductivity in proton-exchange membranes; however, in a practical setting, the higher operational costs of such anion-exchange membrane electrolyzers might well be offset by their (probably) lower capital costs.

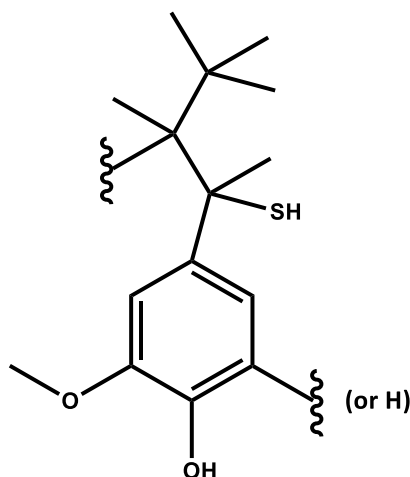


Figure 3.1: Structure of Lignin

Electrolytic water splitting can be expressed in terms of its two constituent half reactions: the oxygen evolution reaction (OER), and hydrogen evolution reaction (HER). Under standard conditions, the thermodynamic minimum voltage required to electrolyse water is 1.23 V. In practice, additional voltages are required to carry out the HER and OER at appreciable currents, on account of energy barriers related to concentration, ohmic resistances, and the kinetics of each half reaction.¹⁸ In water electrolysis, the primary source of these additional voltages, called overpotentials, is the OER, owing to the kinetic demands of carrying out the four-electron, four-proton production of O_2 .¹⁹ Although this energy requirement can be lowered by employing appropriate electrocatalysts, an intriguing alternative to this is to replace the OER with an anode couple that does not (at least in theory) require such significant overpotentials. To this end, the electrolysis of organic compounds as a route to H_2 production has garnered some interest.²⁰⁻²⁴ Provided that the organic substrates that are being oxidised are renewable (e.g., they are derived from plant-based material), then such a system would allow the production of hydrogen from water at lower potentials than the direct electrolysis of water to O_2 and H_2 without adding to the long-term concentration of CO_2 in the atmosphere. Ideally, candidates for these alternative renewable

anodic feedstocks should also be plentiful, non-toxic and otherwise not on the pathway to other critical resources such as foodstuffs. Lignin, a highly aromatic, naturally-occurring polymer found in wood, fits this specification well (Figure 3.1). It is produced as a low-value side product of the Kraft pulping process in volumes of 40–50 million tonnes per year, making it the second most abundant source of renewable carbon and readily available at a low cost.²⁵ Using lignin as a substrate for the production of hydrogen from water could thus leverage value from this by-product, and indeed, the use of lignin in this capacity has been the subject of several publications.^{19,26–34} However, the use of anion-exchange membranes in such lignin-converting electrolyzers remains underexplored, with only a very few examples of such studies reported to date.^{30,35,36}

The research reported herein describes the synthesis of a novel anion-exchange membrane and the testing of its suitability for use in an anion-exchange membrane electrolyser for direct lignin electrolysis. The membrane in question (hereafter called “PVIB”) is a copolymer of dehydrofluorinated poly (vinylidene fluoride-co-hexafluoropropylene) with (vinylbenzyl)trimethylammonium chloride and *N*-vinylimidazole. The performance of this membrane for lignin electrolysis was compared under a range of conditions to that of the commercially-available anion-exchange membrane Fumapem FAA-3-50, which (to the best of our knowledge) is the only anion-exchange membrane yet explored as a separator in a zero-gap lignin-oxidising electrolyser. Fumapem FAA-3-50 is cross-linked, generally non-reinforced anion-exchange membrane with a polyaromatic hydrocarbon backbone and utilising quaternary ammonium moieties to facilitate anion conduction.³⁷ PVIB therefore differs from Fumapem FAA-3-50 both in terms of the nature of its backbone (which is partly fluorinated) and in the incorporation of secondary imidazolium cationic units (see below). PVIB (whose synthesis has not been reported before), therefore seemed to us to offer some potential for increased conductivity and/or chemical stability compared to Fumapem FAA-3-50 when used as the anion-exchange membrane separator in a zero-gap lignin-oxidising electrolyser. With this in mind, we set out to test the performance of PVIB compared to that of Fumapem FAA-3-50 in an anion-exchange membrane lignin-oxidising electrolyser. It was found that the PVIB-based electrolyser performed comparably to an electrolyser using Fumapem for lignin oxidation over short timescales (with an applied potential of 1.2 V driving a current density of 4.4 mA cm⁻² at 70 °C during linear sweep voltammetry), but that membrane durability was an issue over extended testing durations. Together, our results show that PVIB-based membranes could show promise for such electrolysis applications, if their robustness can be improved.

3.2 Experimental

3.2.1 Materials

Ultrapure deionised water (18.2 M Ω ·cm) obtained from a Sartorius Arium Comfort combined water system was used in all experiments. Alkali (Kraft) lignin and sodium hydroxide ($\geq 98\%$) were purchased from Sigma Aldrich and Honeywell, respectively. The electrodes used were commercial products purchased from FuelCellStore. Poly (vinylidene fluoride-co-hexafluoropropylene) ($M_n \sim 130,000$ g/mol), *N*-vinylimidazole and (vinylbenzyl) trimethylammonium chloride monomers were purchased from Sigma Aldrich and used without further purification. Dimethylacetamide and isopropyl alcohol were supplied by SD Fine Chem Ltd. (Mumbai, India).

3.2.2 Flow Cell Components

The flow cell was assembled as shown in Figure 3.2. The anode used was Pt/Ru catalyst (2 mg cm⁻², 50% Pt/50% Ru wt/wt) impregnated on carbon cloth (410 μ m thick microporous layer). The cathode used was a Pt/C catalyst (0.2 mg cm⁻², 20% wt Pt) impregnated on identical carbon cloth to the anode. The commercial anion-exchange membrane FUMAPEM FAA-3-50 was purchased from FuelCellStore. The anolyte used was a solution of alkali lignin (10 g L⁻¹ in 1 M NaOH) and the catholyte was an aqueous solution of NaOH (1 M). The feed solutions were transported to and from the cell using two Fisherbrand GP1100 general purpose peristaltic pumps at a flow rate of 10 mL min⁻¹. The flow plates used were fabricated from stainless steel, with 6 channels (0.9 \times 0.9 mm) through which the feedstock solutions were passed. Gaskets were cut from either 0.45 mm or 0.1 mm thick polytetrafluoroethylene (PTFE). The stack compression was 5.65 Nm and the active area of the membrane was 12.96 cm². The temperature within the cell was controlled by heating the reservoirs of the feed solutions in an oil bath. The temperature was monitored using K-type thermocouples inserted into the inlet and outlet of the anodic side. Temperature data were recorded using a Pico TC-08 data logger and PicoLog software for Windows.

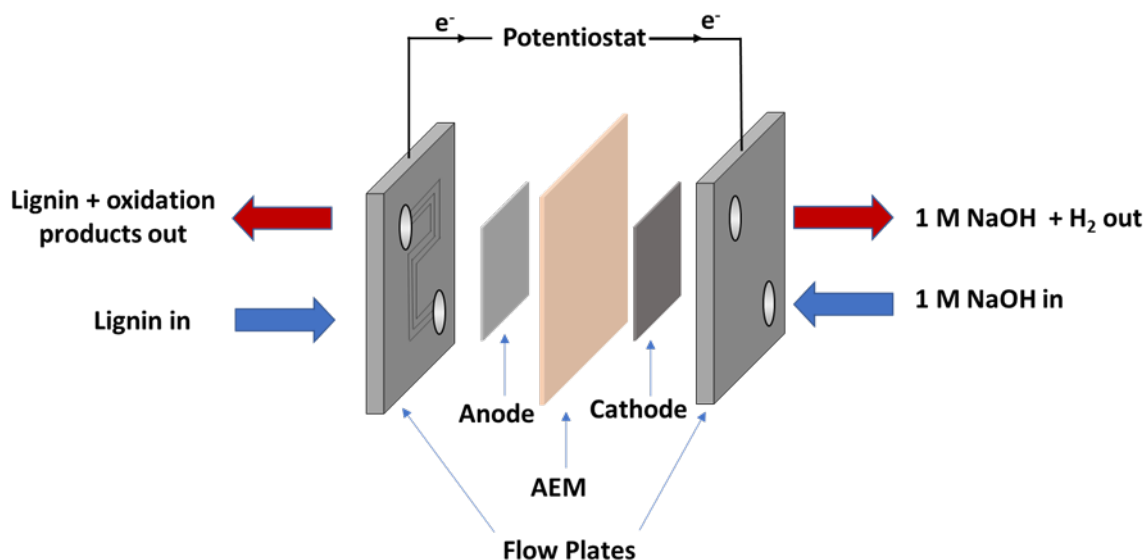


Figure 3.2: Diagram of the electrolyser cell setup used for lignin electrolysis. The electrolyser setup is a “zero-gap” configuration where the anode and cathode catalysts are sandwiched between the conductive flow plates. The potentiostat is connected to each flow plate by way of terminal spades with banana jacks, and so the flow plates also function as current collectors

3.2.3 Electrochemical Characterisation of the Cell

Electrochemical impedance spectroscopy (EIS) and linear sweep voltammetry (LSV) data were recorded for the electrolyser cell using a Bio-Logic SP-150 potentiostat equipped with a VMP3B-20 20 A booster. Data were recorded and analysed using EC-Lab (v11.12). Unless stated otherwise, EIS was carried out under the following experimental parameters: electrolyte flow rate = 10 mL min⁻¹, quiet time (resting at the DC bias potential) = 10 min, starting frequency = 1 MHz, ending frequency = 10 mHz, DC bias = 0.5 V (vs. the open circuit potential), AC excitation amplitude = 14.1 mV. LSV data were recorded at a scan rate of 0.5 mV s⁻¹. The EIS data were fitted to an equivalent circuit, L1 + R1 + Q1/R2 using AfterMath (v1.5.9644, Pine Research Instrumentation Inc. (Durham, NC, USA)). The details of the components of the equivalent circuit are as follows: L1, which is an inductor; R1, which corresponds to the series resistance of the cell (R_s); R2, which corresponds to the polarisation resistance of the cell (R_p); Q1, which represents a constant phase element.

3.2.4 Preparation of PVIB Membrane

Firstly, poly (vinylidene fluoride-co-hexafluoropropylene) (PVDF-co-HFP, 10 g) was dissolved in dimethylacetamide (500 mL). Then, saturated NaOH in isopropanol (10 mL) was added dropwise, over 30 min, while the solution was stirred vigorously at room temperature. During this step the colourless solution turned light brown in colour. The resulting dehydrofluorinated PVDF-co-HFP was then precipitated in water, filtered and then rinsed 3–4 times with deionised water and dried under vacuum at 70 °C. This polymer was then dissolved in a round-bottomed flask containing dimethylacetamide, *N*-vinylimidazole (20% wt), and (vinylbenzyl)trimethylammonium chloride at different weight % concentrations (4%, 6%, 8% and 10%), giving four different types of PVIB membrane on the basis of the amount of (vinylbenzyl)trimethylammonium chloride added: PVIB-4, PVIB-6, PVIB-8 and PVIB-10, respectively. The copolymerisation reaction was initiated by addition of 0.1% of azobisisobutyronitrile (AIBN), and the mixture was continuously stirred at 60 °C for 8 h under an N₂ atmosphere. The resulting viscous solution was cast onto a clean glass plate and dried under vacuum at 55 °C for 24 h. After this, the membrane was equilibrated in 1 M NaOH for 24 h to complete the exchange of Cl⁻ for OH⁻. These hydroxide-exchanged membranes were analysed after thoroughly washing with double distilled water 4–5 times. This work was performed by Arindam K. Das.

3.2.5 Characterisation of the PVIB Membrane

A number of analytical techniques were used to characterise the structure, functional groups, surface and phase morphology of the as-prepared PVIB and its precursors. Functional group analysis of the samples was performed using the PerkinElmer FT-IR spectrometer. Surface and cross-sectional morphology on freshly prepared membranes was analysed on a field-emission electron microscope (FE-SEM) using a JEOL JEM 7100F (USA) instrument. TEM images were recorded with a JEOL JEM 2100 microscope. Scanning electron microscopy on membranes after use in the PVIB-based electrolyser was performed with a Philips XL30 ESEM instrument equipped with an Oxford Instruments Energy 250 energy dispersive spectrometer system at an acceleration voltage of 20 kV. Following use in a lignin-oxidising electrolyser, membranes were thoroughly washed and then submerged in ultrapure water for 2 h, before being oven-dried for 4 h at 55 °C. Samples cut from the membrane were then loaded onto 12 mm AGAR scientific conductive carbon tabs. Images were obtained with acceleration voltages between 12 kV and 20 kV.

To measure the ion-exchange capacity, $2.5 \times 2.5 \text{ cm}^2$ fragments of the prepared membrane were submerged in 1.0 N NaCl (AR grade) solution for 24 h in order for the membrane to be entirely converted to the form with the chloride counter ion. These membrane squares were then removed from solution, thoroughly washed with ultra-pure water and equilibrated in deionised water for 2 h to remove any excess chloride ions from the membrane surface. Finally, the membrane squares were dried in a vacuum oven for 4 h at 55 °C and then weighed. The chloride-saturated membrane was subsequently immersed in 0.1 M Na₂SO₄ in order to allow exchange of the chloride counter ions for SO₄²⁻. The chloride ions thus released into solution were titrated by Mohr's method using 0.001 N AgNO₃ and dichromate solution as the indicator. The ion-exchange capacity (IEC) was then determined using the formula in Equation 3.1, where V_{AgNO_3} is the volume of 0.001 N AgNO₃ solution added and M_{Dry} is the dry mass of the membrane square:

$$\text{IEC (meq g}^{-1}\text{)} = \frac{0.001 \text{ N} \times V_{\text{AgNO}_3}}{M_{\text{Dry}}} \quad (3.1)$$

The ionic conductivity (σ) of the prepared membranes was measured at 30 °C using AC impedance spectroscopy with an AutoLab Model PGSTAT 30 potentiostat/galvanostat frequency response analyser. This instrument was connected to the conductivity cell. The conductivity cell itself was made in-house and consisted of two circular stainless-steel electrodes (each of effective area 1.0 cm²), each of which was encased in an acrylic outer cylinder (approximately 2 cm thick). The membrane was sandwiched between the two stainless-steel electrodes using 0.1 M NaCl as the conducting medium. The frequency of sinusoidal current perturbation was swept from 1 MHz to 1 Hz over the course of each experiment, and the current demanded was swept at 1 μA per second. The resulting Nyquist plot was then used to obtain the resistance of the membrane. The conductivity of the membrane was calculated by entering values for the membrane area (A), the distance between the electrodes (i.e., membrane thickness, L) and the resistance (R) into Equation 3.2 below:

$$\sigma \text{ (S cm}^{-1}\text{)} = \frac{L \text{ (cm)}}{R \text{ (\Omega)} \times A \text{ (cm}^2\text{)}} \quad (3.2)$$

The mechanical strength of the membrane samples (rectangular pieces of size 26 cm²) was studied by using a bursting strength tester machine (model No. 807DMP, Test Techno Consultants, Gujarat, India). The stability of the prepared PVIB membranes in alkaline media was studied by immersing the membranes in 5.0 M NaOH for 72 h at 30 °C. The mass and conductivity of the treated membranes were unaltered by this treatment, suggesting that they are stable in alkaline media at room temperature for at least 72 h.

3.3 Results

3.3.1 Properties of the PVIB Membrane

A schematic of the synthetic route used by Arindam K. Das to generate the PVIB polymer (according to the procedure in Section 2.4) is shown in Figure 3.3.

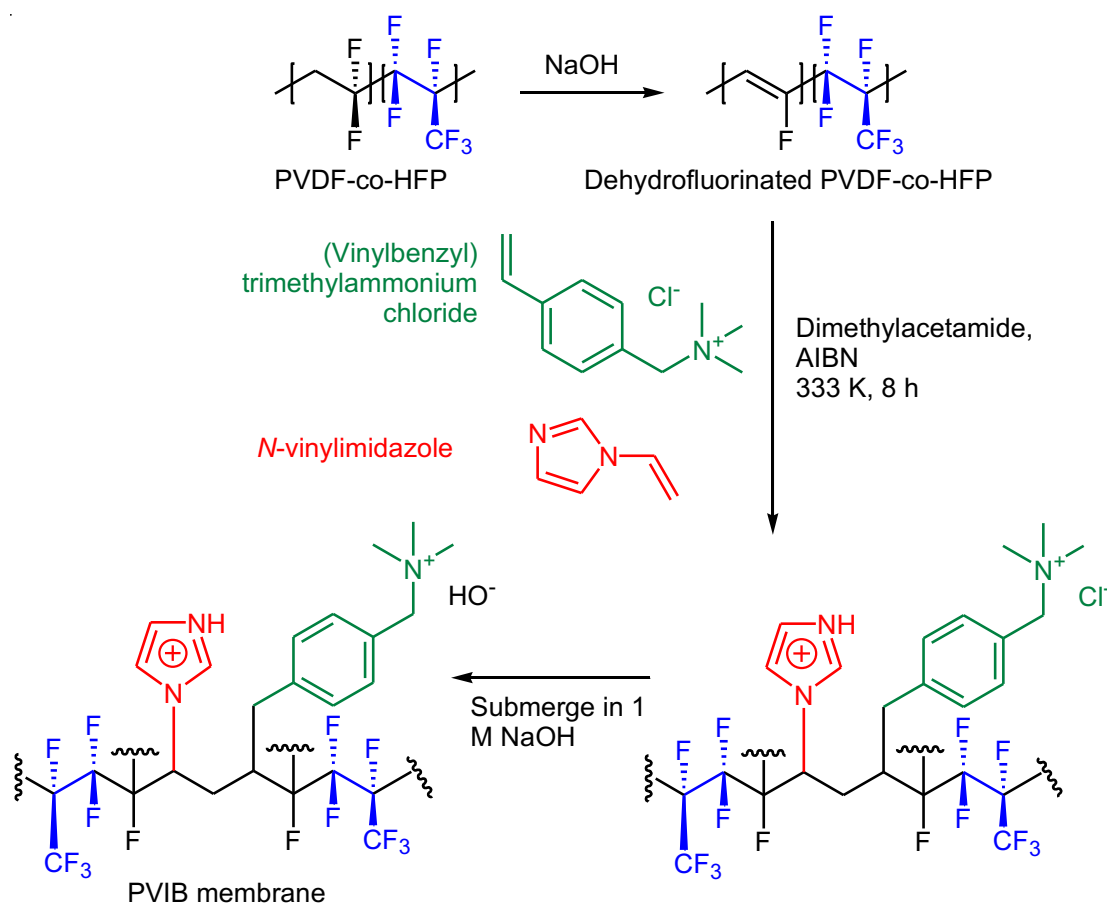


Figure 3.3: Synthesis and structure of the PVIB-based polymer.

Co-polymerisation to produce PVIB was achieved via free radical polymerisation using *N*-vinylimidazole and (vinylbenzyl)trimethylammonium chloride monomers and AIBN as a radical initiator (see Figure 2). The transmission spectrum for PVIB was recorded between 4000 and 400 cm^{-1} , as shown in Figure 3.4. The presence of absorption bands at 1402 cm^{-1} and 2933 cm^{-1} , and 2984 cm^{-1} and 3008 cm^{-1} is attributed to the C-F stretching and methylene ($-\text{CH}_2-$) stretching modes, respectively.³⁸ These peaks confirm the successful co-polymerisation reaction between the monomers and dehydrofluorinated PVDF-co-HFP.

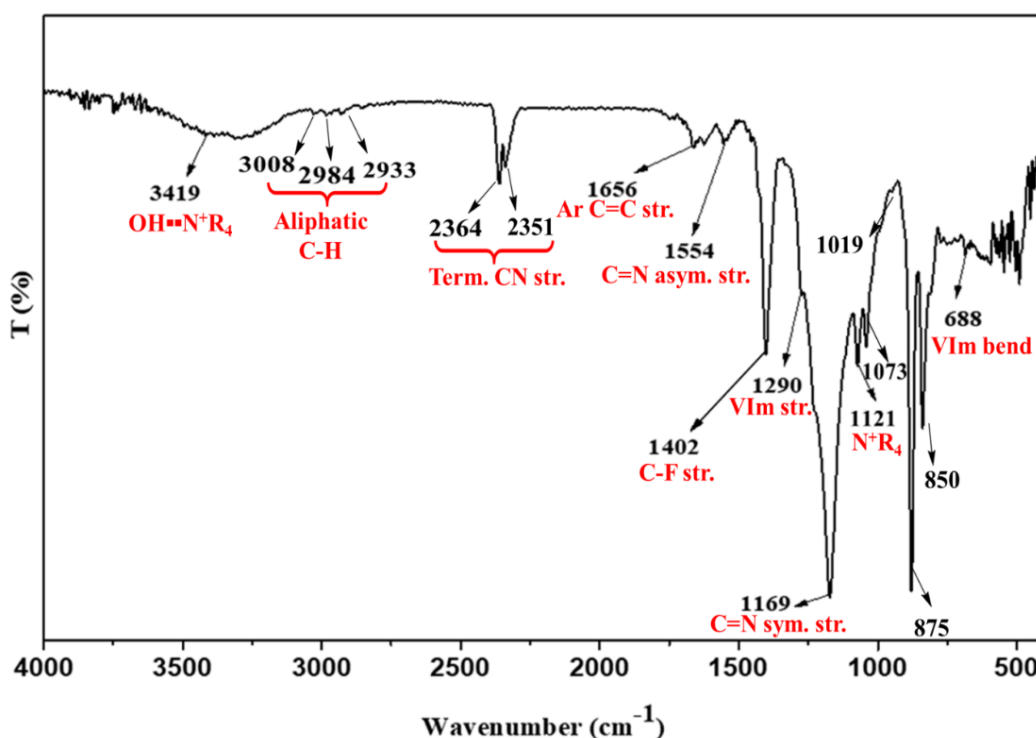


Figure 3.4: ATR-IR transmission spectrum of the PVIB anion-exchange membrane.

Meanwhile, the peaks at 688 cm^{-1} , 1073 cm^{-1} and 1290 cm^{-1} are assigned to the vinylimidazole bending and stretching modes, respectively, whilst the peaks at 1169 cm^{-1} and 1554 cm^{-1} are assigned to symmetric and anti-symmetric C=N stretches in the heterocyclic ring.³⁹ Finally, the peaks at 1121 cm^{-1} , 1656 cm^{-1} , 2352 cm^{-1} , 2364 cm^{-1} and 3419 cm^{-1} confirm ionomer grafting: these peaks are attributed to the stretching modes of C-N⁺, aromatic C=C and O-H (bound water) associated with the quaternary ammonium groups [38,40]. Interestingly, the bands at 850 cm^{-1} , 875 cm^{-1} and 1019 cm^{-1} additionally confirm the para-di-substitution and ring breathing of benzene, respectively.⁴⁰ No absorption bands at 960 or 1690 cm^{-1} (indicative of free vinyl groups) were observed, showing that addition across the double bond is complete.⁴¹

Surface and cross-sectional images (Figure 3.5) were captured by FE-SEM at 15.4 kV incident beam energy. The results illustrate that these membranes (as-prepared) possess homogenous dense morphology (both surface and bulk) devoid of any cracks, pinholes, or any other deleterious morphology which might influence membrane performance (at least at the outset) during application.

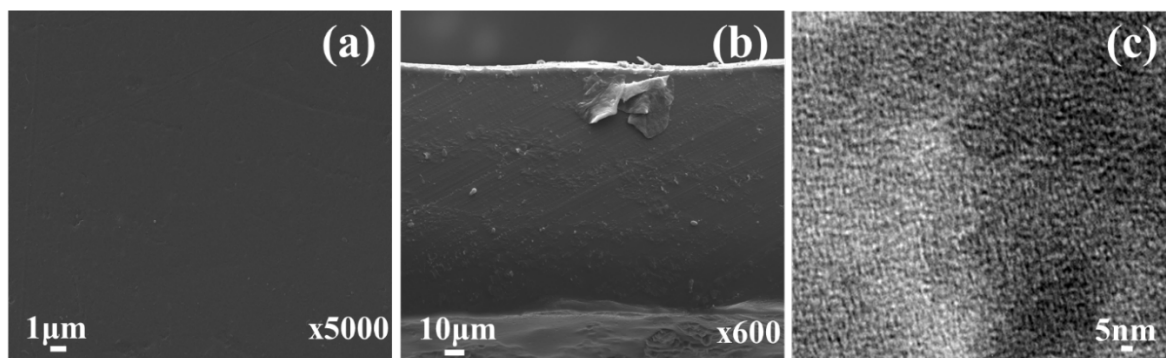


Figure 3.5: Microscopy images of the as-prepared PVIB-10 membrane: (a) SEM image of the membrane surface, (b) SEM image of the membrane cross-sectional morphology and (c) TEM image showing the nano-phase separated morphology of the PVIB-10 membrane.

Hydrophilic/hydrophobic nano-phase separation was examined using TEM. From Figure 4, it is apparent that dark and light regions can be distinguished on the nanometre ($\sim 3\text{--}5$ nm) scale, and that the domains are well connected. The former is attributed to the sinuous (worm-like) hydrophilic domain for $-\text{N}^+(\text{CH}_3)_3$ and the latter accounts for the hydrophobic fluorinated phase of PVDF-co-HFP.⁴² Due to presence of both hydrophobic (PVDF-co-HFP) and hydrophilic (*N*-vinylimidazole) domains, the membrane forming material showed phase separation, which is responsible for the formation of the ion-conducting channels.

Table 1 shows the ion-exchange capacity (IEC) and hydroxide conductivity (κ^m) for the series of PVIB membranes prepared in this work. The extent of ion migration through ion exchangers (in this case, the quaternary ammonium groups) is crucial for good membrane performance and depends upon the amount of charged functionality that is grafted into the polymer. The increase in IEC from 1.43 meq g^{-1} for PVIB-4 to 1.82 meq g^{-1} for PVIB-10 (a 27% increase) is attributed to the increasing degree of (vinylbenzyl) trimethylammonium grafting from 4 wt% to 10 wt% in the membrane matrix. The development of well-established ion percolating channels due to optimum swelling could be the underlying reason for this. A similar trend was observed for OH^- conduction through the membrane matrix: a

17% increase was recorded as this value ranged from $4.12 \times 10^{-2} \text{ S cm}^{-1}$ for PVIB-4 to $4.84 \times 10^{-2} \text{ S cm}^{-1}$ for PVIB-10. The membrane swelling ratio also increased with IEC, due to the associated improvement in the membranes' hydrophilic nature. The mechanical stability of the prepared PVIB membranes was assessed by burst strength value (Table 3.1). Freshly-prepared PVIB-10 membrane gave a burst strength value of 8.93 kg cm^{-2} , suggesting good mechanical stability for the as-prepared membrane.

Table 3.1: Physicochemical, electrochemical and mechanical parameters for the series of PVIB anion-exchange membranes prepared in this work. The codes applied to the different membranes indicate the weight % of (vinylbenzyl) trimethylammonium chloride added during synthesis, as mentioned in the text.

Membrane	IEC (meq g^{-1})	$\kappa^m \times 10^{-2}$ (S cm^{-1})	Swelling Ratio (%)	Burst Strength (kg cm^{-2})
PVIB-4	1.43	4.12	13.2	8.05
PVIB-6	1.62	4.27	15.9	8.34
PVIB-8	1.77	4.49	17.9	8.57
PVIB-10	1.82	4.84	20.5	8.93

3.3.2 Characterisation of the PVIB-Based Electrolyser

To define a benchmark for the performance of our PVIB-based lignin electrolyser, we first constructed an electrochemical cell using the commercially-available anion-exchange membrane, Fumapem (FAA-3–50). The suitability of this membrane for use in a lignin electrolyser has previously been investigated by Caravaca *et al.* [30]. The first method of analysis used was linear sweep voltammetry (LSV). In this technique, the current is recorded as the cell potential is varied. Much like cyclic voltammetry, the recorded current is a function of the scan rate, with higher currents being recorded at the same potentials when using higher scan rates. We therefore selected a very low scan rate (0.5 mV s^{-1}) in order to obtain a current density as close to the steady-state value as possible. Figure 5 shows a comparison of the performance of a cell using the components described in Sections 3.2.1 and 3.2.2 and a Fumapem membrane at various temperatures using a catholyte feed of 1 M NaOH, and an anolyte feed of alkali lignin (10 g L^{-1}) in 1 M NaOH. At $30 \text{ }^\circ\text{C}$, the current

density for lignin electrolysis was rather low and was similar to that achieved in a control without any lignin being present in the anolyte feed at room temperature (around 20 °C): compare the red solid and black-dashed traces in Figure 5. However, at the higher temperatures of 70 °C and 80 °C, significant increases in current density above the lignin-free background were evident, especially at cell potentials greater than 0.8 V. These results are broadly in agreement with those obtained by Caravaca *et al.*³⁰ with their analogous electrolyser and therefore show that the electrolyser configuration described in Sections 2.1 and 2.2 is a valid setup in which to test the performance of the PVIB membrane for lignin electrolysis. We can, therefore, have some confidence in the comparisons that we shall draw between this PVIB membrane and commercially-available alternatives.

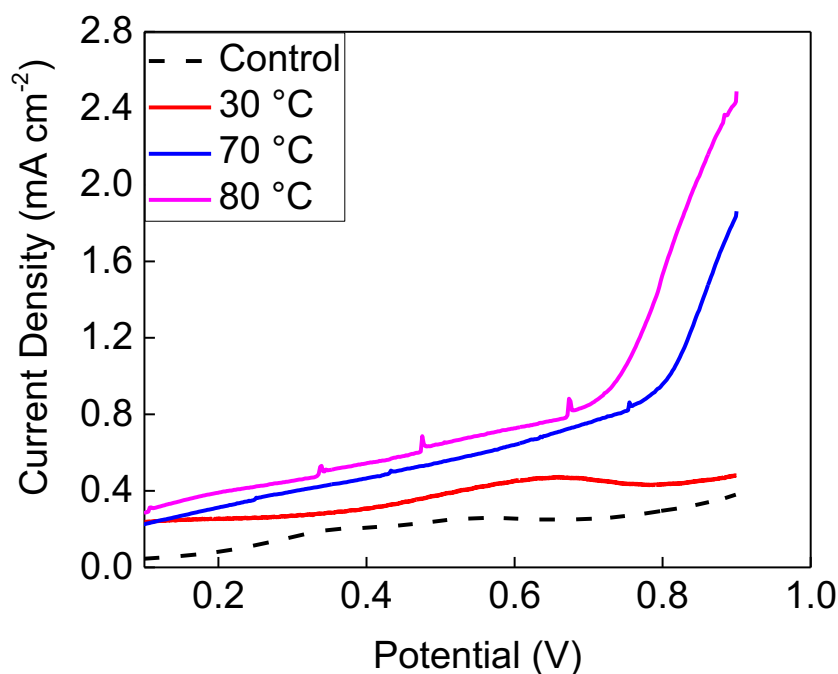


Figure 3.6: Polarisation curves recorded at 80 °C (pink trace), 70 °C (blue trace), and 30 °C (red trace) showing the behaviour of electrolysers using a commercial Fumapem membrane with an anolyte feed of 1 M NaOH containing 10 g L⁻¹ alkali lignin, alongside a control for the electrolyser using only 1 M NaOH at room temperature as the anolyte (black-dashed trace).

LSV measurements at 70 °C were then repeated using this electrolyser setup but having substituted the novel PVIB-10 membrane for Fumapem, as shown in Figure 3.7. Cell potentials were also scanned to more positive values in order to obtain higher current densities for lignin oxidation. A control measurement, shown in Figure 6 as the black-dashed trace, was also performed using PVIB-10 and 1 M NaOH as both the anolyte and catholyte

(i.e., in the absence of lignin). The data in Figure 3.7 show that the PVIB-10-based electrolyser produced current densities almost identical to those produced by the Fumapem-based electrolyser across a range of cell potentials as high as 1.2 V. For example, at 0.9 V a current density of 1.5 mA cm^{-2} was achieved using PVIB-10 (vs. 1.9 mA cm^{-2} when using Fumapem) and at 1.2 V a current density of 4.4 mA cm^{-2} was achieved (vs. 5.3 mA cm^{-2} when using Fumapem). Three repeat runs for both PVIB-10 and Fumapem are shown in Figure 6, indicating that both membranes show fairly consistent performance in these swept-voltage experiments, with only a slight deterioration in performance for the PVIB-10 membrane evident in the third run.

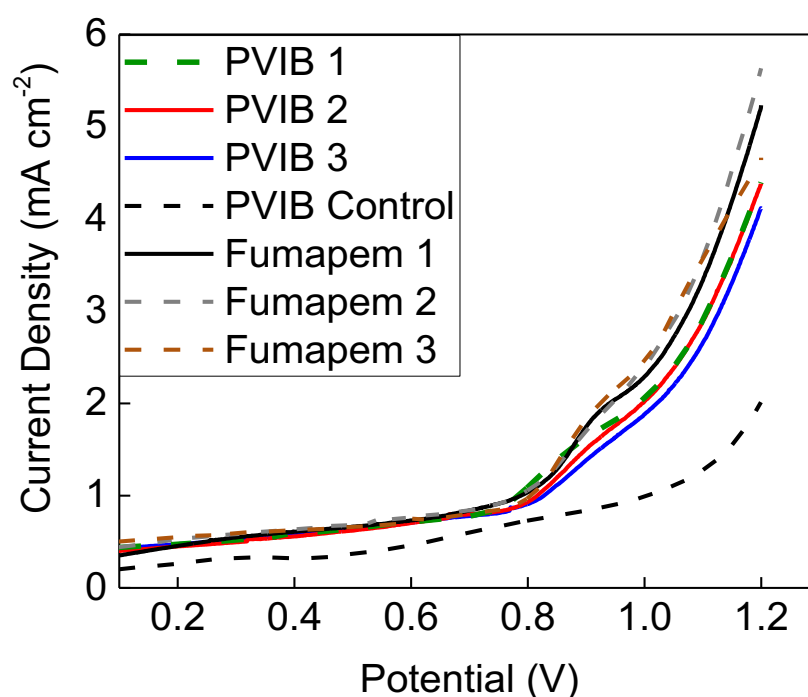


Figure 3.7: Polarisation curves at $70 \text{ }^\circ\text{C}$ showing the behaviour of electrolysers using commercial Fumapem and PVIB-10 with an anolyte feed of 1 M NaOH containing 10 g L^{-1} alkali lignin. The green-dashed line, solid red line and solid blue line show three repeat traces for the PVIB-10 membrane, and the black solid line, grey-dashed line and brown-dashed line show three repeat traces for the Fumapem membrane. A control for a PVIB-10-based system using only 1 M NaOH at $70 \text{ }^\circ\text{C}$ as the anolyte is also provided as the black-dashed trace.

EIS was also performed at $70 \text{ }^\circ\text{C}$ on the PVIB-10 and Fumapem-based electrolysers in order to gain insights into the resistances that these membranes present for lignin oxidation. These data (Figure 3.8) show that the series resistance, R_s , was found to be $0.87 \text{ } \Omega \text{ cm}^2$ for the PVIB-10-based system versus $0.80 \text{ } \Omega \text{ cm}^2$ for the Fumapem system, whilst the polarisation

resistance, R_p , for the PVIB-10 electrolyser was slightly lower than for the Fumapem system ($1.47 \Omega \text{ cm}^2$ versus $1.59 \Omega \text{ cm}^2$). R_s can be obtained from Figure 3.8 by considering where the semi-circle first intercepts the x -axis at high frequency. In an ideal setting, R_p is then simply the difference between the high and low frequency intercepts of the x -axis. As the data in Figure 3.8 do not intercept the x -axis again at low frequency, R_p was obtained by fitting the data to an equivalent circuit as described in Section 3.2.3. The polarisation resistance can be thought of as the sum of the resistances associated with polarising the cell, such as the energy barriers associated with the HER and OER, and kinetic and mass transfer effects. From the technical datasheet for Fumapem provided by the manufacturer, the stated OH^- conductivity for this membrane is lower than the observed OH^- conductivity of PVIB-10 ($4.0 - 4.5 \times 10^{-2} \text{ S cm}^{-1}$ for Fumapem versus $4.84 \times 10^{-2} \text{ S cm}^{-1}$ for PVIB-10). This slightly better in conductivity for (freshly-prepared) PVIB-10 versus Fumapem is borne out by the lower value of R_p . A comparison between the ion-exchange capacity and hydroxide conductivity of PVIB-10 and a selection of anion-exchange membranes from the recent literature is given in Table 3.2. Taken together, the EIS and LSV data suggest that PVIB and Fumapem show very similar underlying performance when employed as anion-exchange membranes in lignin-oxidising electrolysers, at least on the short timescales of the LSV experiments.

Table 3.2. Ion-exchange capacity (IEC) and hydroxide conductivity (κ^m) values for PVIB, and a selection of anion-exchange membranes from papers referenced in this work.

Membrane	IEC (meq g ⁻¹)	$\kappa^m \times 10^{-2}$ (S cm ⁻¹)	Ref
PVIB-10	1.82 ^a	4.84	This work
GT82-5	3.84 ^a (3.76 ^b)	10.9	14
GT64-15	3.26 ^a (3.28 ^b)	6.2	14, 15
XL4-PNB-X ₃₄ -Y ₆₆	3.43 ^b	8.68	16
Fumapem FAA-3-50	2.02	4.0–4.5	30

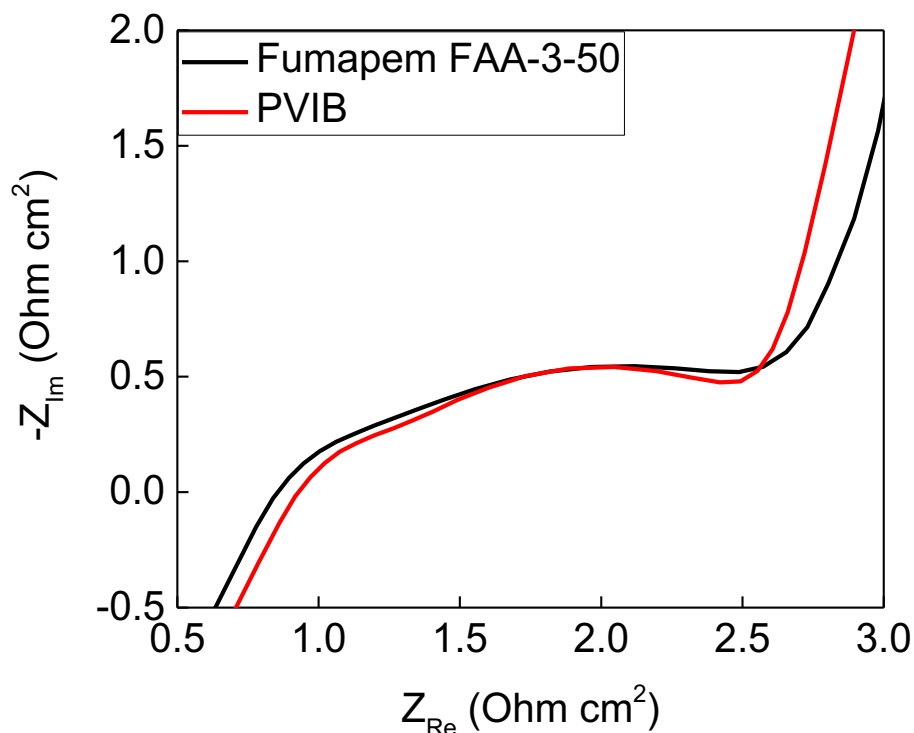


Figure 3.8: EIS comparison between commercial Fumapem and PVIB-10 at 70 °C when used in the electrolyser. Both the anolyte and catholyte were 1 M NaOH.

3.3.3 PVIB in Alternative Electrolyser Configurations

Before arriving at the final cell configuration using lignin, the PVIB membrane was tested in several other electrochemical systems. The first of these configurations, was a conventional water electrolysis cell, where both the catholyte and anolyte were ultrapure water. It was immediately apparent that PVIB was unsuitable for such a use, as EIS measurements indicated resistances multiple hundreds of times higher than what could be considered a feasible value. The consequence of this can be observed in the LSV where, even at potentials reaching 2.5 V, the current density does not exceed 1 mA cm^{-2} (Figure 3.9).

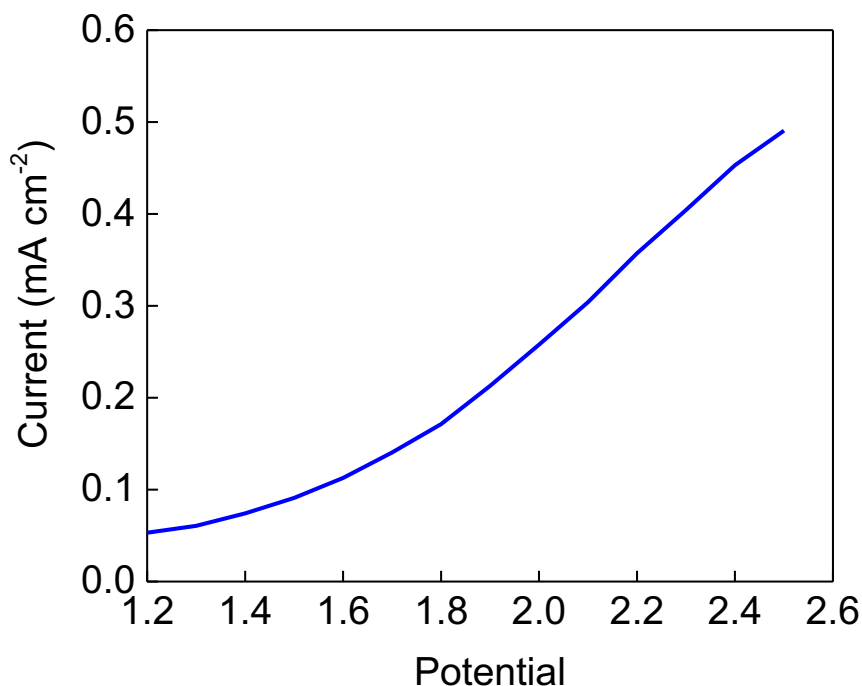


Figure 3.9: Polarisation curve recorded at room temperature showing the behaviour of the PVIB electrolyser using ultrapure water as both the catholyte and anolyte.

Based on the work of Ito et. al.,⁴³ an anolyte of 1% K_2CO_3 was also used in the cell configuration. Using this cell configuration, an I-V plot was collected by holding the cell potential at a given voltage for 10 mins while measuring the current response. After 10 minutes, the voltage was increased by 100 mV and the process repeated. The results of this can be seen in Figure 3.10, where although the current density is more than 4 times higher than what was measured using only ultrapure water, the performance of the cell still falls way below a system which could be considered viable.

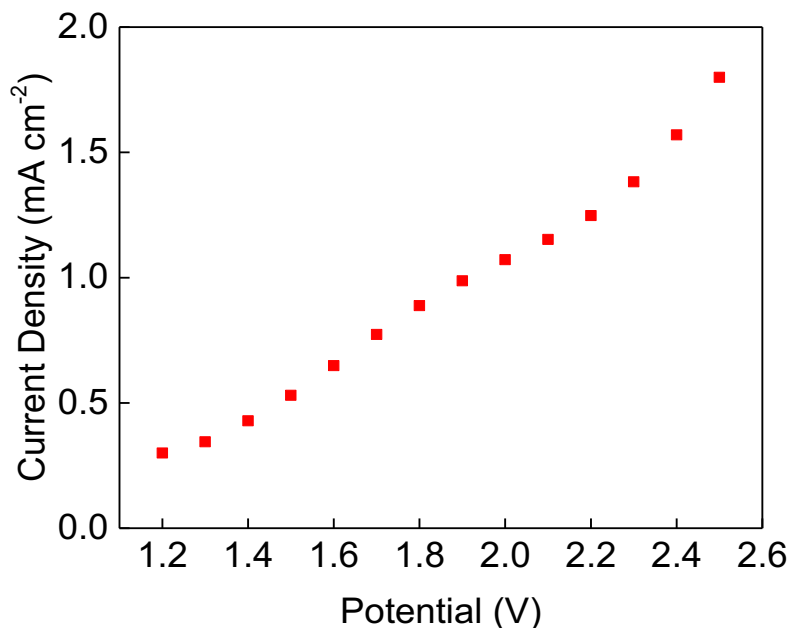


Figure 3.10: I-V plot recorded using the PVIB electrolyser with an analyte of 1% K_2CO_3 showing the average current response over 10 mins at each set potential.

The performance of the PVIB electrolyser in these experiments made clear that a switch in approach to utilising a chemical that would significantly lower the electro-oxidation potential of the cell was required, hence the use of lignin in our final configuration.

3.3.4 PVIB Degradation

Upon repeated testing of the PVIB-10 membranes in the continuous flow lignin electrolyser, it was noted that resistances increased, and current densities decreased at any given cell potential, suggesting that the membranes were unstable under extended use for lignin oxidation. Examination of the membranes after such repeated testing also showed that they had become less mechanically robust and more prone to warping and holing over the course of these experiments. Figure 3.11 shows typical examples of such damage, which tended to manifest most obviously around the edges of the active area (visible as the black square in Figure 8) where the membrane was most warped.

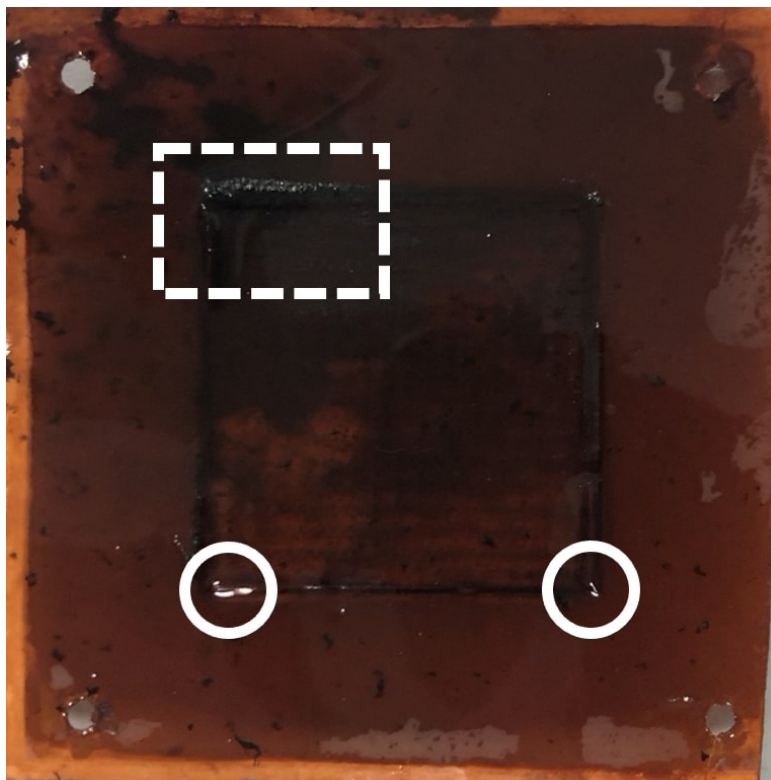


Figure 3.11: Warped and holed PVIB-10 membrane after repeated use. The total area of the membrane is a square of dimensions 7×7 cm.

Such warping is especially evident at the top left of the active area (highlighted with the dashed rectangle) whilst holes are present in the bottom left and right of Figure 3.11 (circled). The morphology of the membranes after use in the PVIB-based electrolyser was examined by SEM, as shown in Figure 3.12. Panel (a) in Figure 3.12 shows an image of an area of the membrane that appeared relatively undamaged to the naked eye. Nevertheless, considerable cracking is evident, and the morphology is now much less uniform when compared with pristine samples (see Figure 3.5). Meanwhile, Figure 3.12 b shows an image of an area where damage was already apparent by eye, and in this case extensive holing of the membrane on the microscale is evident. Clearly, then, the membrane has suffered significant deterioration as a result of use in the electrolyser. Further insight into the higher resistance of the membrane after use was found by considering the ion-exchange capacity of the used membranes: after repeated use, the ion-exchange capacity (as measured by the protocol in Section 3.2.5) was found to decrease to around 0.4 meq g^{-1} for PVIB-10 (compared to 1.82 meq g^{-1} for pristine membranes, see Table 3.1). Such a decrease in ion-exchange capacity suggests chemical degradation of the membrane by removal of cationic groups. Submersion in alkaline medium alone does not reduce the ion-exchange capacity of the membranes at room temperature (see Section 2.2.5), and so the cause of the membrane degradation is most

likely a combination of applied potential during membrane testing, together with the elevated temperature and basic medium.

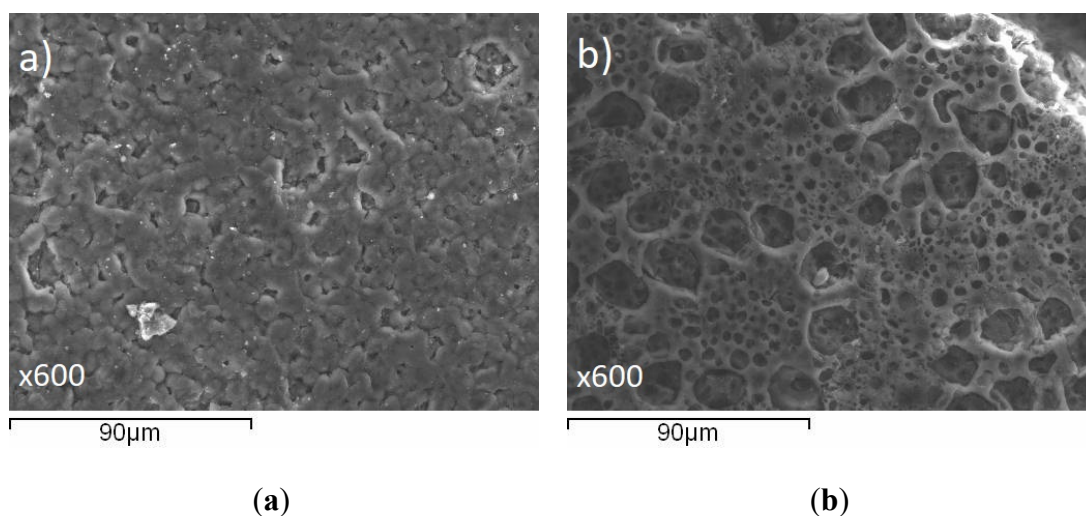


Figure 3.12: Microscopy images (at $\times 600$ magnification) of the PVIB-10 membrane after testing in a lignin-oxidising electrolyser: (a) SEM image of an area of the membrane surface that was apparently undamaged to the naked eye and (b) SEM image of an area of the membrane surface where damage was already evident by eye.

In terms of the mechanism of membrane degradation that leads to this loss of ion-exchange capacity, Sata *et al.* have previously shown⁴⁴ that anion-exchange membranes bearing benzyl trimethylammonium groups can suffer chemical degradation after immersion in highly alkaline solutions at temperatures of 75 °C (very similar conditions to those that we use here). These authors attributed their degradation to decomposition of the benzyl trimethylammonium moieties via attack of hydroxide at the carbon in between the benzene ring and the trimethylammonium unit through an S_N2 mechanism, yielding free trimethylamine and the benzyl alcohol derivative of the polymer. Moreover, there is evidence that this mechanism is also operating in our case: an IR spectrum collected on used membranes (Figure 3.13, red trace) shows that the peaks at 2352 cm^{-1} , 2364 cm^{-1} (assigned to the terminal $C-N^+$ stretches in the quaternary amine groups in Figure 3) are completely absent in the used membranes, suggesting that these groups have been mostly cleaved during operation.

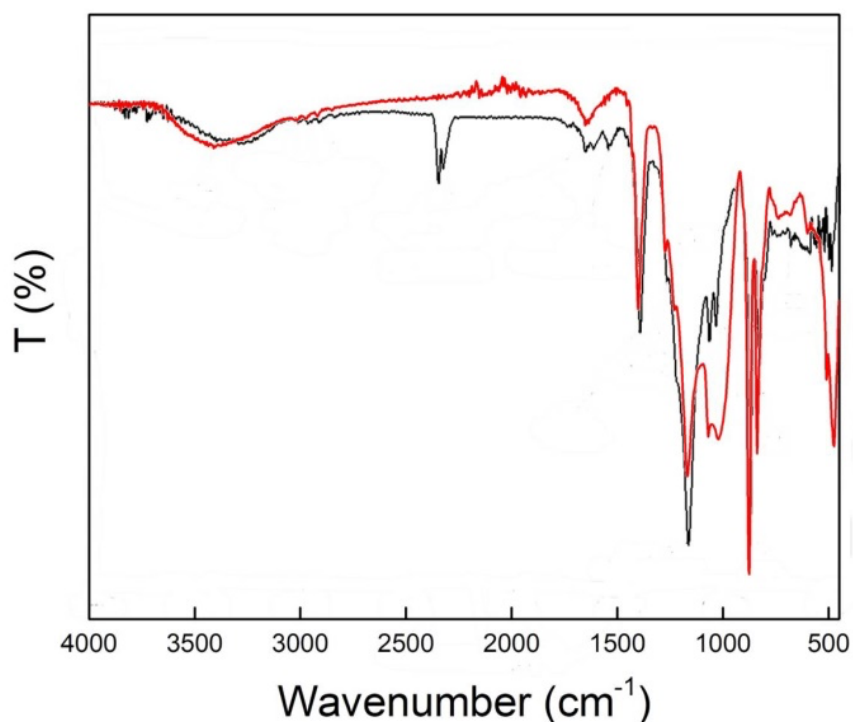


Figure 3.13: ATR-IR transmission spectrum of the PVIB-10 anion-exchange membrane before use (black) and after extensive use (red).

If cleavage of the trimethylamine groups is indeed operating in our case, then inserting an additional methylene unit(s) in between the trimethylammonium moiety and the aromatic ring would be expected to significantly retard this S_N2 mechanism and hence lead to increased stability of the membrane in highly alkaline solution. A similar strategy has been shown to be effective in previous work reported in the literature.⁴⁵⁻⁴⁷ The synthesis of a suitable monomer for this purpose that could be used in a synthetic scheme similar to that shown in Figure 3.3 has been reported.⁴⁸ Figure 3.14 a shows the putative hydroxide-mediated membrane degradation mechanism and Figure 3.14 b shows a structure for the proposed more robust polymer using this alternative monomer that might show slower degradation in alkaline solution at elevated temperature.

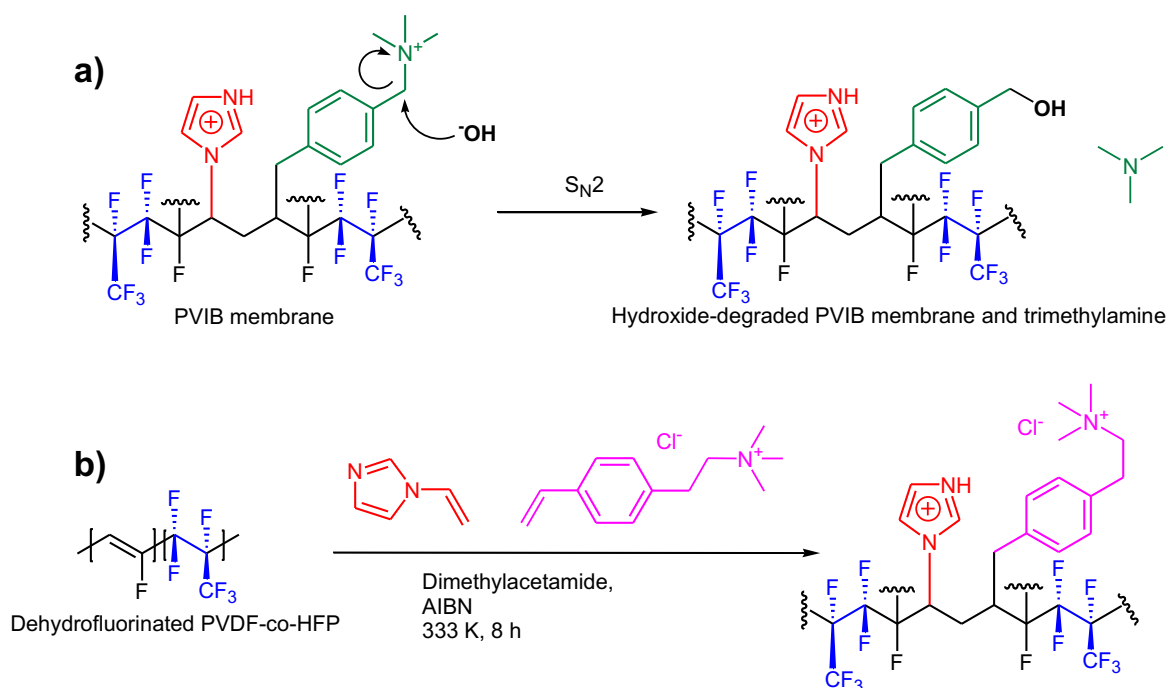


Figure 3.14: (a) A possible hydroxide-mediated route to membrane degradation involving the cleavage of trimethylamine from the polymer. (b) A potential strategy for the synthesis of a more stable analogue of PVIB: The vinylbenzene derivative highlighted in pink replaces (vinylbenzyl) trimethylammonium chloride in the general synthetic scheme shown in Figure 2, with the extra methylene group disfavoring the facile S_N2 mechanism shown in panel (a).

Regardless of the cause of this membrane degradation, such behaviour has so far prevented us from obtaining reliable data for steady-state operation (including current-time curves, hydrogen yields and investigations of the products of lignin electrolysis) to compare with that for a Fumapem-based electrolyser. Work to improve the longevity of these membranes so that such data can be obtained is currently underway in our laboratories.

3.4 Conclusions

In summary, we have described the synthesis and characterisation of a novel anion-exchange membrane, PVIB. This membrane was then employed in a continuous flow lignin oxidation cell, using Pt/C and Pt/Ru catalysts impregnated on carbon cloth. It was found that the performance of the novel membrane was competitive with a commercial equivalent, Fumapem, over short timescales, although long-term durability remains an ongoing challenge.

As may be deduced from the point in development at which this chapter ends, the continuation of this project was severely inhibited by logistical issues caused by the COVID pandemic. The majority of the data presented in this chapter was collected before our lab in Glasgow, and the labs of our collaborators in Bhavnagar, were closed for a lengthy amount of time. By the time this shutdown ended, our collaborator responsible for the synthesis of PVIB, Arindam K. Das had completed his PhD and moved to a job in a different country. It is for this reason that the synthesis of the alternative AEM proposed in figure 3.14 was not performed. Similarly, it had been planned to investigate the use of alternative catalysts which may further bring down the capital cost of this cell's construction. However, despite the aforementioned issues, the results collected using PVIB give us some encouragement that this material could one day be developed into a cost-effective conductive separator for electrolysers that simultaneously oxidise lignin and generate hydrogen.

References

- 1 I. Dincer, *Energy Policy*, 1999, **27**, 845–854.
- 2 I. Roger, M. A. M. A. Shipman and M. D. M. D. Symes, *Earth-abundant catalysts for electrochemical and photoelectrochemical water splitting*, 2017, vol. 1.
- 3 N. S. Lewis and D. G. Nocera, *Powering the planet: Chemical challenges in solar energy utilization*, 2006, vol. 103.
- 4 J. S. Wallace and C. A. Ward, *Int. J. Hydrogen Energy*, 1983, **8**, 255–268.
- 5 M. Carmo, D. L. Fritz, J. Mergel and D. Stolten, *Int. J. Hydrogen Energy*, 2013, **38**, 4901–4934.
- 6 G. Gahleitner, *Int. J. Hydrogen Energy*, 2013, **38**, 2039–2061.
- 7 E. M. Sommer, L. S. Martins, J. V. C. Vargas, J. E. F. C. Gardolinski, J. C. Ordonez and C. E. B. Marino, *J. Power Sources*, 2012, **213**, 16–30.
- 8 J. Chi and H. Yu, *Chinese J. Catal.*, 2018, **39**, 390–394.
- 9 P. Millet, F. Andolfatto and R. Durand, *Int. J. Hydrogen Energy*, 1996, **21**, 87–93.
- 10 S. A. Grigoriev, P. Millet, S. A. Volobuev and V. N. Fateev, *Int. J. Hydrogen Energy*, 2009, **34**, 4968–4973.
- 11 M. Schalenbach, M. Carmo, D. L. Fritz, J. Mergel and D. Stolten, *Int. J. Hydrogen Energy*, 2013, **38**, 14921–14933.
- 12 I. Vincent, A. Kruger and D. Bessarabov, *Int. J. Hydrogen Energy*, 2017, **42**, 10752–10761.
- 13 J. R. Varcoe, P. Atanassov, D. R. Dekel, A. M. Herring, M. A. Hickner, P. A. Kohl, A. R. Kucernak, W. E. Mustain, K. Nijmeijer, K. Scott, T. Xu and L. Zhuang, *Energy Environ. Sci.*, 2014, **7**, 3135–3191.
- 14 M. Mandal, G. Huang, N. U. Hassan, X. Peng, T. Gu, A. H. Brooks-Starks, B. Bahar, W. E. Mustain and P. A. Kohl, *J. Electrochem. Soc.*, 2020, **167**, 054501.
- 15 N. Ul Hassan, M. Mandal, G. Huang, H. A. Firouzjaie, P. A. Kohl and W. E. Mustain, *Adv. Energy Mater.*, 2020, **10**, 2001986.
- 16 M. Mandal, G. Huang and P. A. Kohl, , DOI:10.1021/acsaem.8b02051.
- 17 C. Zhang, W. Zhang and Y. Wang, *Membranes (Basel)*, 2020, **10**, 169.

- 18 C. Xiang, K. M. Papadantonakis and N. S. Lewis, 2016, **3**, 169.
- 19 S. B. Lalvani, *J. Electrochem. Soc.*, 1992, **139**, L1.
- 20 H. Ju, S. Badwal and S. Giddey, *Appl. Energy*, 2018, **231**, 502–533.
- 21 I. V. Pushkareva, A. S. Pushkarev, S. A. Grigoriev, E. K. Lyutikova, S. V. Akel’kina, M. A. Osina, E. P. Slavcheva and V. N. Fateev, *Russ. J. Appl. Chem.*, 2016, **89**, 2109–2111.
- 22 A. Caravaca, A. de Lucas-Consuegra, A. B. Calcerrada, J. Lobato, J. L. Valverde and F. Dorado, *Appl. Catal. B Environ.*, 2013, **134–135**, 302–309.
- 23 G. Sasikumar, A. Muthumeenal, S. S. Pethaiah, N. Nachiappan and R. Balaji, *Int. J. Hydrogen Energy*, 2008, **33**, 5905–5910.
- 24 P. J. McHugh, A. D. Stergiou and M. D. Symes, *Adv. Energy Mater.*, 2020, **10**, 2002453.
- 25 O. Movil-Cabrera, A. Rodriguez-Silva, C. Arroyo-Torres and J. A. Staser, *Biomass and Bioenergy*, 2016, **88**, 89–96.
- 26 H. R. Ghatak, *Int. J. Hydrogen Energy*, 2006, **31**, 934–938.
- 27 H. R. Ghatak, S. Kumar and P. P. Kundu, *Int. J. Hydrogen Energy*, 2008, **33**, 2904–2911.
- 28 S. B. Lalvani and P. Rajagopal, *Holzforschung*, 1993, **47**, 283–286.
- 29 F. Bateni, M. NaderiNasrabadi, R. Ghahremani and J. A. Staser, *J. Electrochem. Soc.*, 2019, **166**, F1037–F1046.
- 30 A. Caravaca, W. E. Garcia-Lorefice, S. Gil, A. de Lucas-Consuegra and P. Vernoux, *Electrochem. commun.*, 2019, **100**, 43–47.
- 31 R. Tolba, M. Tian, J. Wen, Z. H. Jiang and A. Chen, *J. Electroanal. Chem.*, 2010, **649**, 9–15.
- 32 W. Liu, Y. Cui, X. Du, Z. Zhang, Z. Chao and Y. Deng, *Energy Environ. Sci.*, 2016, **9**, 467–472.
- 33 X. Du, W. Liu, Z. Zhang, A. Mulyadi, A. Brittain, J. Gong and Y. Deng, *ChemSusChem*, 2017, **10**, 847–854.
- 34 T. Hibino, K. Kobayashi, M. Nagao and S. Teranishi, *ChemElectroChem*, 2017, **4**, 3032–3036.

- 35 M. NaderiNasrabadi, F. Bateni, Z. Chen, P. B. Harrington and J. A. Staser, *J. Electrochem. Soc.*, 2019, **166**, E317–E322.
- 36 O. Movil, M. Garlock and J. A. Staser, *Int. J. Hydrogen Energy*, 2015, **40**, 4519–4530.
- 37 M. T. Tsehaye, F. Alloin and C. Iojoiu, *Energies 2019, Vol. 12, Page 4702*, 2019, **12**, 4702.
- 38 P. P. Sharma, V. Yadav, A. Rajput and V. Kulshrestha, *Desalination*, 2018, **444**, 35–43.
- 39 A. G. Kuba, Y. Y. Smolin, M. Soroush and K. K. S. Lau, *Chem. Eng. Sci.*, 2016, **154**, 136–142.
- 40 J. Sharma, S. K. Misra and V. Kulshrestha, *Chem. Eng. J.*, 2021, **414**, 128776.
- 41 O. V. Lebedeva, Y. N. Pozhidaev, E. A. Malakhova, T. V. Raskulova, A. N. Chesnokova, V. Kulshrestha and A. S. Pozdnyakov, *Membr. Membr. Technol.*, 2020, **2**, 76–84.
- 42 X. Q. Wang, C. X. Lin, Q. G. Zhang, A. M. Zhu and Q. L. Liu, *Int. J. Hydrogen Energy*, 2017, **42**, 19044–19055.
- 43 H. Ito, N. Kawaguchi, S. Someya, T. Munakata, N. Miyazaki, M. Ishida and A. Nakano, *Int. J. Hydrogen Energy*, 2018, **43**, 17030–17039.
- 44 T. Sata, M. Tsujimoto, T. Yamaguchi and K. Matsusaki, *J. Memb. Sci.*, 1996, **112**, 161–170.
- 45 M. Mandal, G. Huang and P. A. Kohl, *J. Memb. Sci.*, 2019, **570–571**, 394–402.
- 46 J. Y. Jeon, S. Park, J. Han, S. Maurya, A. D. Mohanty, D. Tian, N. Saikia, M. A. Hickner, C. Y. Ryu, M. E. Tuckerman, S. J. Paddison, Y. S. Kim and C. Bae, *Macromolecules*, 2019, **52**, 2139–2147.
- 47 M. Mandal, G. Huang, N. U. Hassan, W. E. Mustain and P. A. Kohl, *J. Mater. Chem. A*, 2020, **8**, 17568–17578.
- 48 Wakabayashi, K.; Shimamura, M.; Akashi, Y.; Otake, S.; Matsuda, T.; Ito, M.; Noguchi, A.; Mori, H. Developer Carrier and Developing Device. WO2013035254, 14 March 2013.

Chapter 4:

Oxygen Production via Electrolysis in Altered Gravity Environments

Published as “Predicting the efficiency of oxygen-evolving electrolysis on the Moon and Mars.” B. A. Lomax, G. H. Just, P. J. McHugh, P. K. Broadley, G. C. Hutchings, P. A. Burke, M. J. Roy, K. L. Smith, and M. D. Symes, Nat. Commun., 2022, 13, 583.

Acknowledgements and Declarations

The work presented in this chapter was performed as part of the European Space Agency’s FlyYourThesis! Programme, alongside 4 other researchers who I would like to thankfully acknowledge for their contribution to this chapter. The team was led by my colleague Bethany A. Lomax (B.L.), with Gunter H. Just (G.J.) acting as the lead engineer. Paul K. Broadley (P.B.) and Greg C. Hutchings (G.H.) were primarily involved in implementing the centrifuge control, accelerometer feedback and pressure measurement and release systems. The design of the electrochemical system was the results of equal contributions from B.L. and myself (P.M.). The microgravity and hypergravity data presented was collected by P.M., B.L., G.J. and P.B.. The data manipulation behind the extrapolations, and method for normalising of voltages between cell were conceived by B.L. who also identified the current loss issue in section 4.3.2.

Abstract:

Gas evolving electrolysis is an attractive route to oxygen production in future space missions due to the availability of in-situ resources containing oxygen on many astronomical objects (e.g. ice water on the Moon and Mars, metal-oxide abundant Lunar soil). However, no study to date has been performed that examines the efficiency of this process in reduced gravity environments. In the research presented herein, the relationship between gravity and electrolysis efficiency is investigated in both the reduced gravity ($<1\text{ g}$) and hypergravity range ($> 8\text{g}$). The findings suggest that at a fixed potential, electrolytic oxygen production would suffer a 10 % and 6% reduction if performed on the Moon and Mars respectively. The agreement in the trends recorded in both the reduced gravity and hypergravity ranges suggest that data collected in future hypergravity studies can be extrapolated to predict the performance of the electrolyser at lower g-levels without the need for costly microgravity testing.

4.1 Introduction

Naturally, the future of manned space missions is heavily reliant on oxygen, however the transport of this oxygen in the payload of a spacecraft can be costly. To that end, oxygen evolving electrolysis is considered vital to the future of space exploration, with potential implementation in life support systems, fuel cells, or as an in-situ resource utilisation (ISRU) process.^{2,3}

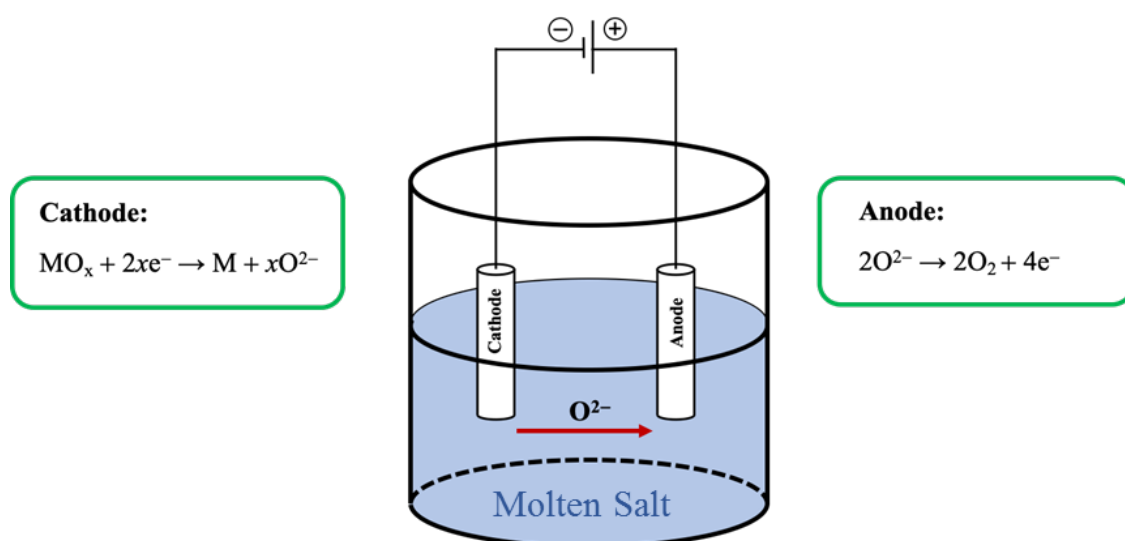


Figure 4.1: Basic representation of the FFC-Cambridge process in which electrolysis in a molten salt electrolyte is utilised to reduce a solid metal oxide cathode with the simultaneous production of oxygen at an inert anode.

As discussed in section 1.3.2, the Fray-Farthing-Chen (FFC)-Cambridge process, a method which employs electrolysis for oxygen extraction from solid metal oxides, is one such ISRU procedure which is currently being investigated for its candidacy in future ESA missions (Figure 4.1). This technique, first reported in 2000, involves the reduction of solid metal oxides in a molten salt electrolyte at high temperatures (700 – 900 °C). The key here is that the process is carried out at an appropriately high voltage so as to decompose the solid metal oxide cathode, but not the electrolyte; when paired with specific anodes (e.g. SnO₂ doped with 2 % Sb₂O₃ and 1 % CuO, CaTi_xRu_{1-x}O₃), the metal oxide reduction can be achieved with simultaneous oxygen production.⁴⁻¹⁴ In the years since, this technique has been

employed as a route to the generation of a variety of metals from their respective oxides (e.g. Ti, Si, Cr and others),^{4,7,15,16} and is widely considered a promising, low-cost route to simultaneous metal and oxygen production. Recently the viability of this method was established using lunar regolith as a feedstock; with an oxygen content of 40-45% by mass, the suitability of this material is evident.^{8,17} Using a lunar regolith simulant, Lomax *et al.* demonstrated that up to 96% of the oxygen could be extracted from the metal oxides in the soil.

An important consideration for all gas evolving electrolyses, is how the efficiency of the process can be impacted by bubble generation. In a typical electrochemical system, gas evolved throughout the experiment forms bubbles which remain adhered to the surface of the electrode.¹⁸ Whilst on the surface, the bubble blocks contact between the electrode and the electrolyte, essentially making that area of the electrode inactive. Before oxygen evolving electrolysis is implemented in future space missions, it is of great importance that examination of this bubble behaviour is performed in altered gravity environments. To that end, a number of studies have done so using parabolic flight and drop towers.¹⁹⁻²⁹ Parabolic flight and drop towers allow researchers to perform their experiment at 10^{-2} and 10^{-6} g respectively, however, testing at gravity levels between these points and Earth's gravity is more complex. Using a centrifuge, the efficiency of electrolysis as a function of gravity has been more thoroughly established in hypergravity, i.e. at gravity levels greater than Earth's gravity (1 g). These studies have all found that with increasing gravity, the force of buoyancy is increased which reduces bubble retention time; this serves to increase the overall efficiency of the process.^{18,30-32} In a model put forward by Cheng *et al.* which was later verified in a study published by Wang *et al.*, it was proposed that the relationship between cell potential (E) and applied gravity (g) followed a logarithmic trend (Equation 4.1); where E_g is the cell potential at the tested g-level, α is the rate of change, and E_c is a potential constant.^{30,33} However, it has not yet been proven whether this trend persists in the reduced gravity range or that extrapolation of the data between the two ranges is valid.

$$E_g = \alpha \log(g) + E_c \quad (4.1)$$

Although lunar regolith would be the ideal test material for oxygen extraction, the operational temperatures required for the FFC-Cambridge process (700 – 900 °C) make testing in reduced gravity using parabolic flight or the drop tower logistically difficult. The identification of ice water on the Moon and Mars suggest that water may too become available on these astronomical objects as an oxygen extraction source. One would expect there to be some overlap in the findings of a study using water, when compared to performing electrolysis in the molten salt, despite the relative differences in temperature of the electrolyte. For that reason, electrolysis is performed in this work using an aqueous system at room temperature.

To date, no experimental verification of the process between 0 and 1 g has been published; this literature gap is starker when you consider that the g-levels relating to Lunar and Martian gravity fall within this range. Probing the efficiency of gas-evolving electrolysis within this range is vital to its implementation as a route to oxygen production for manned space travel. In this chapter, we investigate the efficiency of oxygen-evolving electrolysis in the literature gap. To achieve this, small electrolysis cells were attached to the arms of a small centrifuge. In the background of microgravity, provided by parabolic flight, these cells were spun such that the relative centrifugal acceleration experienced at the electrode is equal to the g-levels of study. The efficiency of this process was probed at 9 different g-levels from 0 to 1 g including Lunar (0.166 g) and Martian (0.376 g) gravity. In addition, using identical cells and centrifuge, hypergravity measurements were taken up to 8 g thus allowing extrapolation of the data between the two gravity ranges. The results from this show that in all conditions tested, the relationship between gravity and electrolysis efficiency follows a logarithmic trend with data from each set following the trend in good agreement. The work in this chapter therefore serves as the first experimental validation that work done in ground based hypergravity studies can be used to accurately predict the efficiency of the process in reduced-gravity conditions.

4.2 Experimental

4.2.1 Materials

HPLC grade water was used in all experiments. The gold foil (0.025 mm thick, Premion 99.985 %), copper foil (0.025 mm thick, annealed uncoated, 99.8 %), Nafion™ N-117 (0.18 mm thick), and anhydrous copper sulfate (98 %) were purchased from Alfa Aesar. The sulfuric acid solutions used were prepared by dilution of 5 M sulfuric acid (titration grade) purchased from VWR chemicals. The reference electrodes used were Ag/AgCl gel electrolyte reference electrodes purchased from pine research.

4.2.2 Cell Design

The cells were manufactured from polycarbonate and comprised of two compartments (anodic and cathodic), separated by a Nafion™ N-117 proton exchange membrane held in place by a polycarbonate frame. The anodic compartment of the cell contained a 1.25 x 1.25 cm (1.5625 cm²) gold foil electrode, whilst the cathodic compartment housed a copper foil electrode of identical dimensions. An Ag/AgCl reference electrode, fixed to the cell lid via a cable gland, was also positioned in the anodic chamber (Figure 4.2).

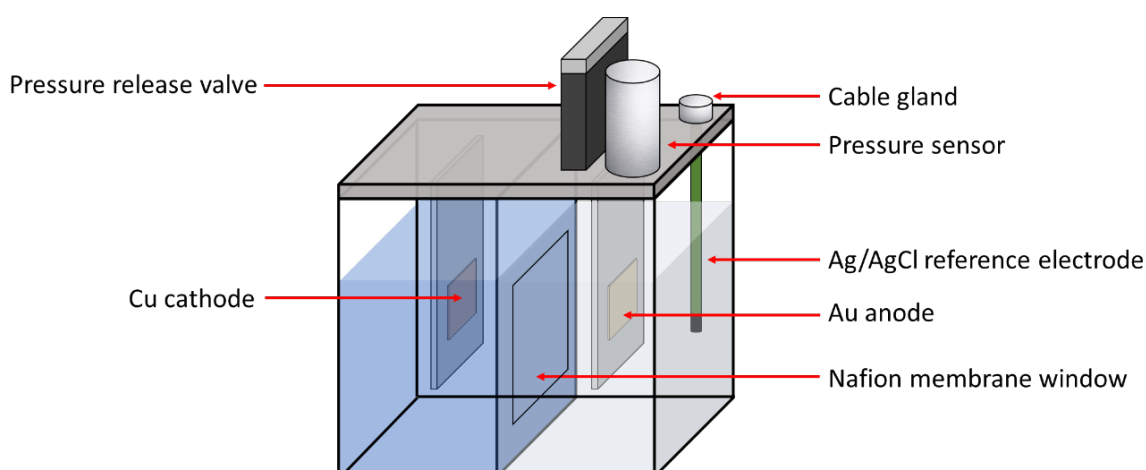


Figure 4.2: Diagram of each cell showing the gold anode, copper cathode and Ag/AgCl reference electrodes with each chamber separated by a Nafion membrane window. In addition, a pressure sensor and release valve are also shown above the anodic chamber.

The metal foil electrodes were soldered to tin-coated copper wire and fixed to the lid of the cell on polycarbonate electrode holders with epoxy resin (Gorilla Glue Company). The tin-coated copper wire was fed through a groove in the electrode holders, allowing the metal foil electrodes to remain flat; this groove was then silicon sealed to insulate the wire. These electrodes were positioned such that the metal foils were parallel to the direction of the applied gravitational field; the copper electrode was positioned facing the centre of the cell whilst the gold foil faced the transparent outer wall of the cell allowing for video recording. Unless otherwise stated, the anolyte used throughout the project was sulfuric acid (0.75 M, 37 mL) and the catholyte was copper sulfate in sulfuric acid (1.135 M CuSO₄ in 0.75 M H₂SO₄, 32 mL). Each cell lid was also equipped with a pressure sensor (Cynergy3 IPSL-G0050-5M12/PRO) and a controllable release valve (Bürkert 00290108). The cell was sealed using 12 bolts, with a gasket sandwiched between the lid and the main body. The seal was tested before each experiment, to ensure each cell was gas and liquid tight.

4.2.3 Experimental Rig

To simulate different gravity levels, 4 cells as described in section 4.2.2 were held in baskets attached to the arms of a centrifuge (radius = 25 cm) (Figure 4.3). These baskets were free swinging for loading/unloading of each cell, but fixed in a vertical position during testing. The centrifuge was assembled on a vibration dampening table to mitigate the influence of external vibrations (i.e. from the plane) on our experiment. A motor at the top of the centrifuge shaft controlled the rotation of the cells, with an accelerometer attached to one of the baskets providing a feedback loop for the control system.

This centrifuge/table assembly was housed in a larger waterproof containment box to ensure that in the event of a cell leakage, no electrolyte could enter the cabin of the aircraft. In addition to the centrifuge, within the containment box there was two stationary cells fitted upon a vibration dampening table; evidently these cells recorded measurements only in microgravity. The 6 cells within the containment box were connected to a multichannel potentiostat (Biologic VMP). The experiment was carried out by two operators, with one monitoring and controlling the centrifuge and pressure systems and the other controlling the multichannel potentiostat.

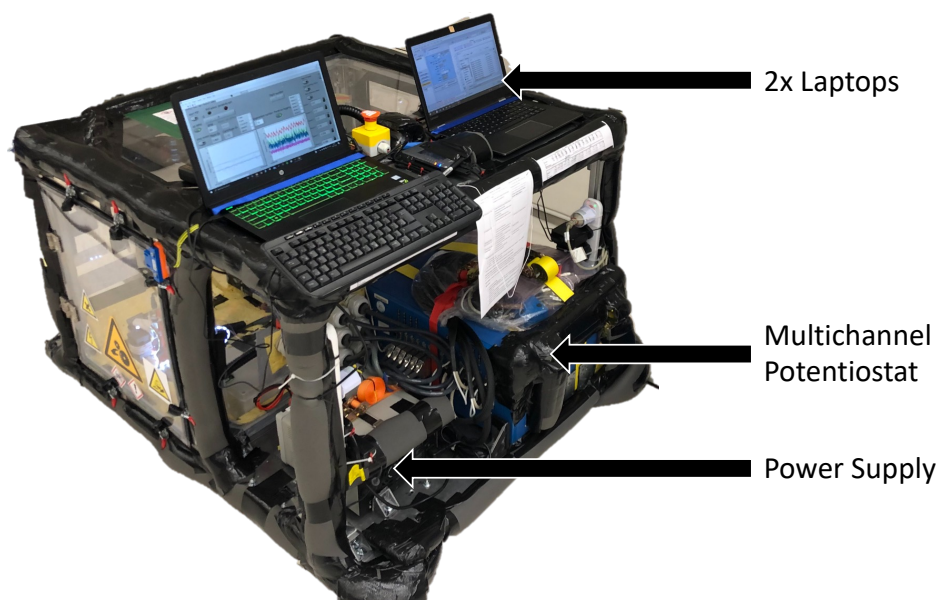
Tables 4.1 & 4.2: List of g-levels tested and corresponding RPM at which the cells were spun for both the microgravity and hypergravity investigations.

Microgravity:

g-level	RPM
0.01	5.981
0.025	9.458
0.05	13.375
0.075	16.381
0.1	18.915
0.133	21.814
0.166	24.370
0.2	26.750
0.25	29.907
0.3	32.762
0.376	36.678
0.5	42.295
0.6	46.332
0.8	53.500
1	59.815

Hypergravity:

g-level	RPM
1	59.815
1.25	66.875
1.5	73.258
1.75	79.128
2	84.591
2.5	94.576
3	103.602
3.5	111.903
4	119.630
4.5	126.886
5	133.750
6	146.516
7	158.255
8	169.182



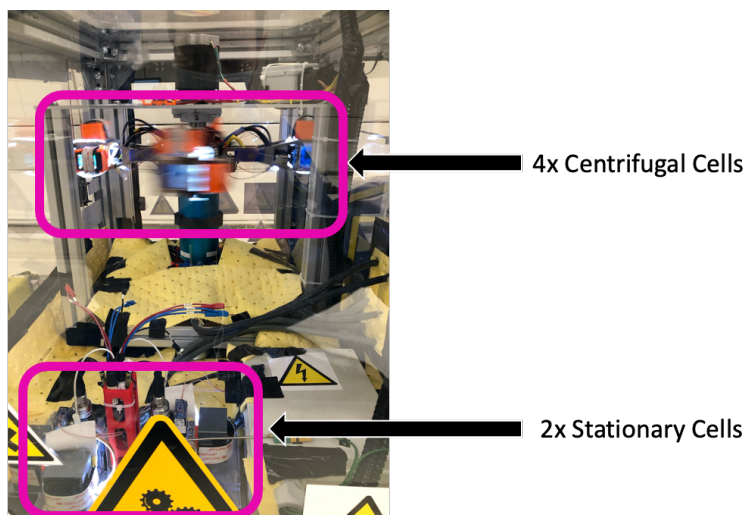


Figure 4.3: (Top) External photo of experimental rig (Bottom) Photo of internal of experimental box, cells have been highlighted with purple boxes for clarity. G.J. and P.B. were behind most of the design and assembly of centrifuge and external containment box, B.L. and P.M. designed the cells. Integration of these systems was a result of equal contribution from all members of the team.

4.2.4 Investigated Parameters

Electrolysis was carried out at fixed current densities (galvanostatic electrolysis) of 50, 75, 100 mA cm⁻² and a fixed potential (potentiostatic electrolysis) of 0.75 V. For all electrolysis parameters listed, data was collected at varying g-levels between 0 and 1 G. Oxygen production was monitored using pressure sensor, fitted above the anodic chamber of the cell. Two HD cameras, positioned to video the front face and side of the gold foil electrode, were positioned on each basket to allow for recording of bubble formation. A time-gap of ~3 mins was maintained between each electrochemical experiment to limit the result of each experiment being influenced by concentration gradients.

4.2.5 Flight Plan

The reduced gravity experiments were carried out with a background of microgravity achieved through parabolic flight aboard a NOVESPACE® Airbus A310 aircraft. This flight manoeuvre involves the plane gaining altitude at a pitch angle of 50° for roughly 20 seconds, during this phase the cabin experiences hypergravity at 1.8 g. Upon reaching an altitude of

around 7600 m, the plane alters its pitch axis such until the nose is pointed down at angle of 42° ; during this phase the cabin experiences microgravity for ~ 22 seconds. As the plane decreases in altitude, the aircraft is gradually levelled off inducing another period of hypergravity within the cabin of the aircraft (Figure 4.4). This manoeuvre is repeated for 31 successive parabolas, 30 of which can be used for experiments. Our experimental data was collected from 3 flights.³⁴

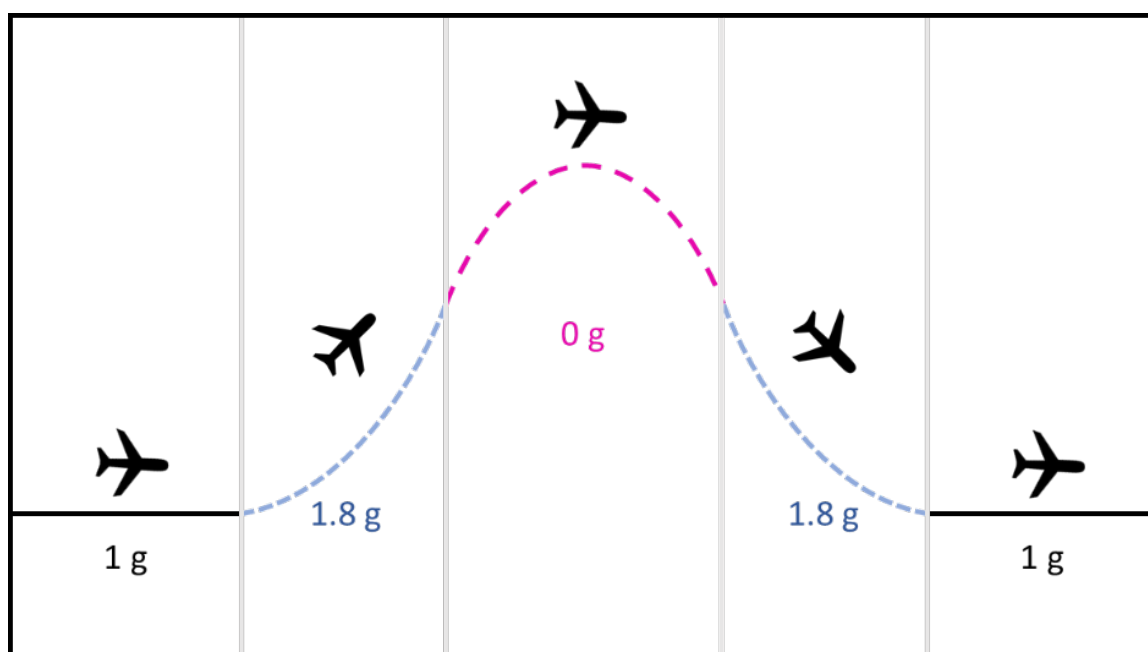


Figure 4.4: Diagram showing the basic flight path of the aircraft during a single parabola; steady flight, during which the cabin experiences 1 g, is indicated by the black line; the blue lines show the phases of the manoeuvre when the plane is pulling up and levelling out, when the cabin experiences 1.8 g; the pink line represents the period of the manoeuvre when the cabin experiences microgravity.

Unfortunately, due to several issues which arose on each flight day, not all cells were in operation as expected. Ground tests were performed before each flight to ensure that each cell was functioning as expected; if any of the cells failed these tests their respective channels were deselected. Some issues with cabling on the centrifuge cells came to light during this step; for this reason only two centrifuge cells were operational in flights 1 & 3, and only 3

were running in flight 2. Full details on number of replicates available for each measurement is in appendix 1.



Figure 4.5: Patrick McHugh and Gunter Just in microgravity (as indicated by the floating pen) during one of the parabolas.

4.3 Results

4.3.1 Cell Consistency

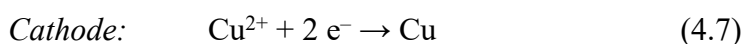
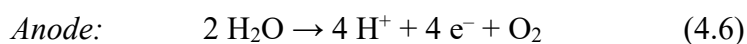
The unique environment in which this experiment was carried out meant that our initial vision of the experiment had to be altered to operate within the limitations of parabolic flight. These restrictions included limits on the concentration of acid permitted, constraints on the overall volume of electrolyte allowed on board, and the inhibiting of significant hydrogen production. The cathodic reaction for hydrogen production and copper reduction are given by Equation 4.2 & 4.3.



Note that the reduction potential of Cu^{2+} is more positive than H^+ . This value is an indication of the tendency a given species has towards accepting electrons, with more positive values indicating greater susceptibility to reduction. Thus, in an aqueous system containing both Cu^{2+} and H^+ ions, copper deposition will be the dominant reaction at the cathode. Hydrogen production can thus be avoided, so long as the concentration of Cu^{2+} ions around the cathode is sufficiently high. Considering this value for the two most likely anodic reactions (equations 4.4 & 4.5), it is clear that the presence of sulfate ions does not inhibit oxygen production as, of the two, water oxidation has the more negative reduction potential and so has a greater tendency towards electron donation.



One operational restriction was that each cell must be sealed and inaccessible during flight; this posed a potential issue with ensuring a degree of chemical consistency for each cell over the course of 30 parabolas. Regarding the reaction being carried out in each compartment of the cell (equations 4.6 & 4.7), there were two primary factors which had to be controlled;



1. The CuSO_4 concentration, as this is consumed throughout the experiment.
2. The acidity, as the protons generated in each parabola could drastically alter the pH of the electrolyte.

A handful of electrolyte systems were tested under 30 successive galvanostatic bulk electrolyses to mimic the experimental conditions undergone during a single flight. Initial control tests were performed using aqueous CuSO_4 solution (0.3 M) as the electrolyte, using a simple two-electrode setup. In this system, across the 30 electrolyses, a downward trend in potential was observed. pH probe measurements also indicated that within the cathodic chamber, the pH dropped from a value of 3.75 to 3.18. In the anodic chamber of the cell this drop was more significant, with the final pH recorded to be 2.86. These results taken together indicated that pH variance across the 30 parabolas meant that the recordings were not comparable. To address this, 5 mL of phosphate buffer (0.5 M) was added to the electrolyte in the anodic chamber. However, there was still a significant drop in the pH in this system (3.75 to 3.29). At this point it was suggested that carrying out the experiment in acidic conditions, where the protons generated throughout the experiment are comparatively negligible to the concentration of protons present in the electrolyte, may yield more consistent results. As such, tests were carried out on an electrolyte comprised of 1 M CuSO_4 in 1 M H_2SO_4 which yielded promising results in two regards; the potential across the 30 repeats was relatively stable and the overall potential requirement for the process was lower.

As could be expected based on Equation 4.6, bubbles of oxygen are produced as this experiment proceeds. In between each parabola on the final flight, it had been planned to rotate the centrifuge arm at 60 rpm to help clear this deposited gas layer since the difference in electrode coverage may be introduce inconsistencies between each run. To replicate this

for the consistency tests, a stirring bar had been used to agitate the solution between each electrolysis. However, as can be seen in Figure 4.6, large variations were recorded. It was found that leaving a time interval between each measurement (equal to the real time between each parabola on the flight), with no agitation of the solution, yielded a much more consistent set of results. The dataset was further improved when readings from the initial few seconds of electrolysis (i.e. the times in which initial electrode coverage may be more significant) were discarded, and the average potential was calculated from measurements taken between 4 and 18 seconds of the electrolysis.

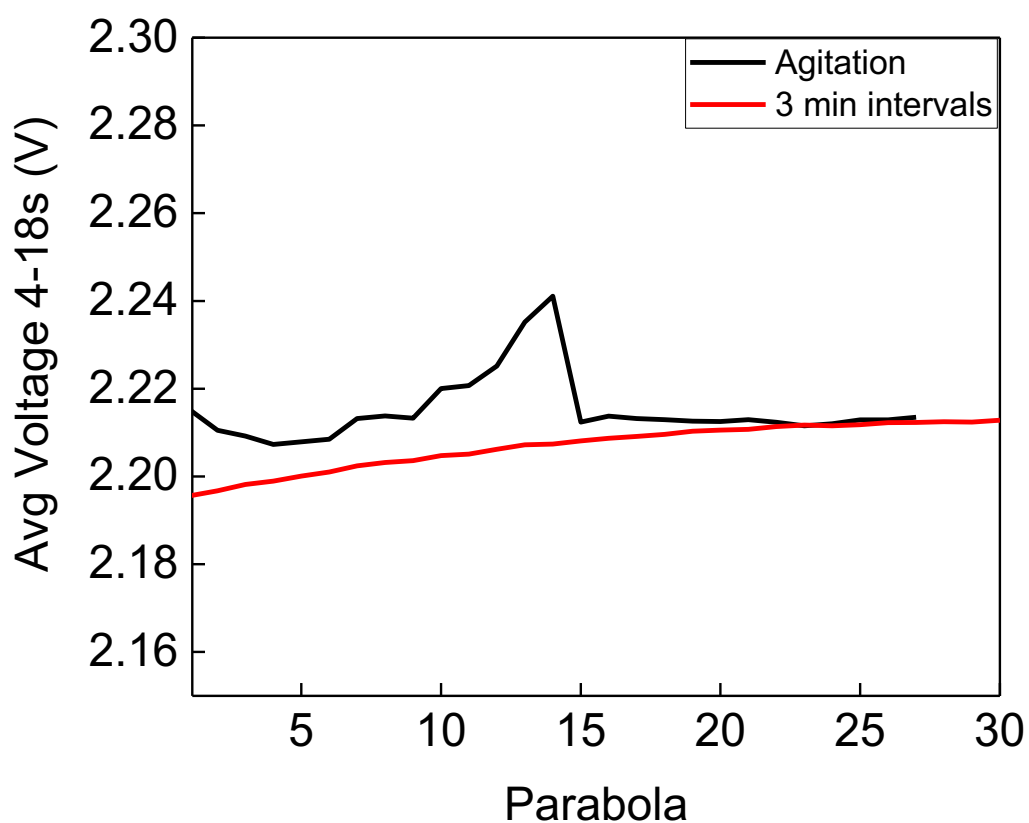
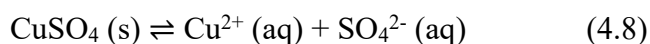


Figure 4.6: Results of consistency tests carried out in a two-compartment cell, showing comparison of average voltage required to meet current demand of 50 mAcm^{-2} between 4-18s in solutions of 1 M CuSO_4 in 1 M H_2SO_4 .

Importantly, over the development time, several changes were made to the cell design to comply with further recommendations from Novespace. These included changing the anodic electrolyte to just H₂SO₄, and alterations to the electrolyte volume and electrode size. Solubility issues related to CuSO₄ arose from these changes, leading to a process of iterative modification of the electrolyte. It was observed that a decrease in acid concentration promoted solubility; this could be expected when considering the equation for dissolution of copper sulfate (Equation 4.8):



A decrease in acid concentration decreases the concentration of sulfate ions, which would promote the forward reaction in the equation above. Thus, multiple iterations of the electrolyte were trialled until optimal concentrations of each electrolyte constituent was achieved. Ultimately, consistent datasets across all electrolysis conditions was achieved using 0.75 M H₂SO₄ as the anolyte and 1.135 M CuSO₄ in 0.75 M H₂SO₄ as the catholyte.

4.3.2 Microgravity Results

As discussed in section 4.2.5, the microgravity data was collected over three flights. As 30 parabolas were available on each flight for experimentation, it was decided that two different electrolysis conditions would be tested each flight (allowing for 15 different g-levels to be investigated per condition). On flight 1 galvanostatic electrolysis was performed at 50 and 100 mA cm⁻², flight 2 was used to record data at 75 mA cm⁻² and 2.075 V vs Ag/AgCl. For both flights, the applied g-level was increased for each parabola starting at the lowest value (0.01 g) up to the highest measurement (at 1 g); the full list of each g-level and corresponding centrifuge rpm, is in table 4.1. To ensure that any observed trends were as a function of the change in g-level and not due to other changes which may occur over the course of the flight (i.e. increase in cabin temperature, electrolyte consumption etc.), flight 3 was used to repeat the measurements taken in flight 1 but in reverse order.

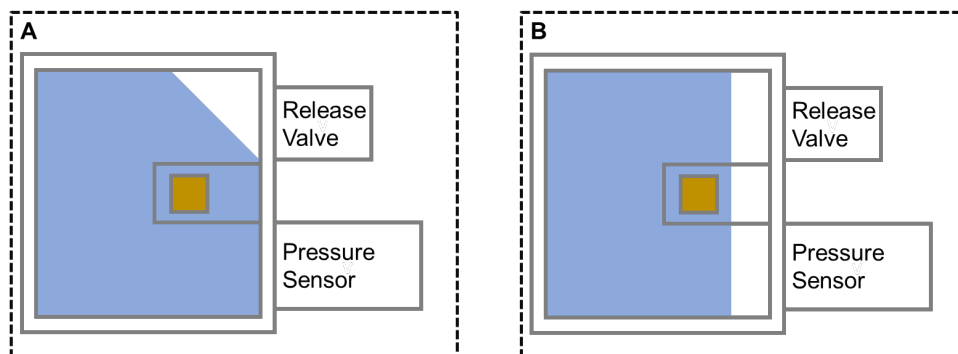
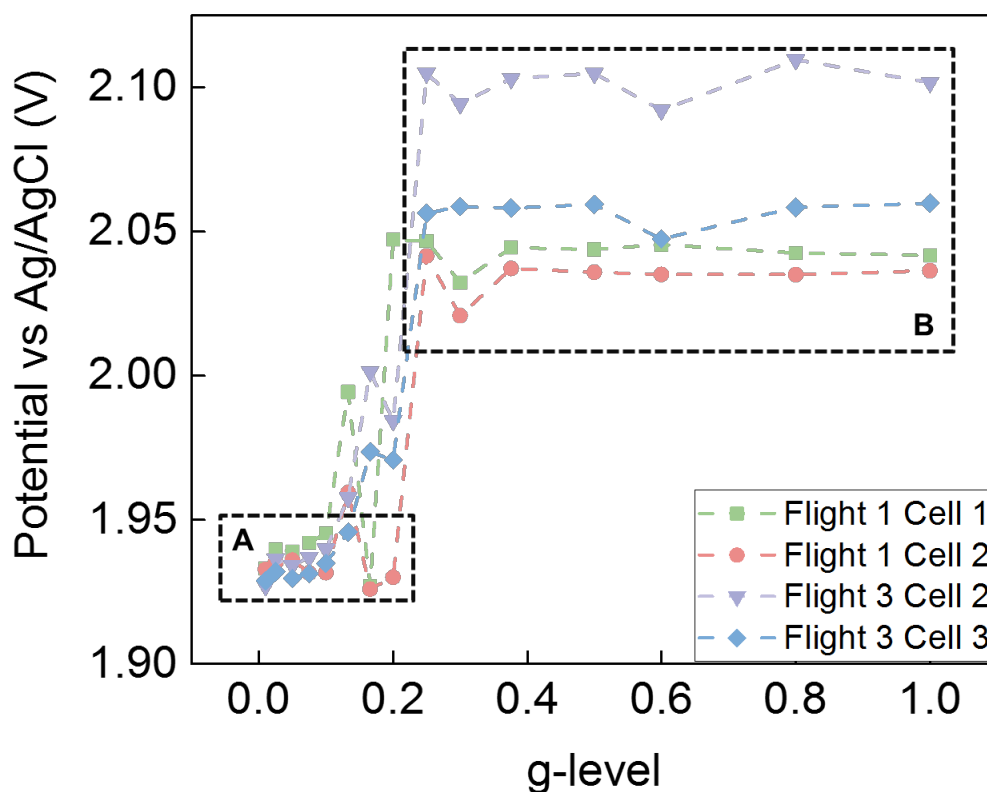


Figure 4.7: (above) Sample set showing the relationship between g-level and potential requirement for the cells to operate at a fixed current of 50 mA cm^{-2} , with “low resistance” region denoted A, and “high resistance” region denoted B. (below) Simplified cell diagram showing the corresponding electrolyte orientation for each of the labelled regions.

Upon initial inspection of our data, an unexpected trend was observed. As discussed in the introduction, previous investigations into the relationship between gravity and electrolysis had found a consistent trend, with the process becoming more efficient as g-level is increased.^{18,30–32} The data collected in this experiment indicated the opposite, suggesting a

“low resistance” window between 0.0 and 0.2 g with consistent potential demands/currents recorded in this range. As g-level was increased a tipping point was observed, above which a similar “high resistance” range was found (Figure 4.7). This trend was consistent across all centrifugal cells tested and persisted in both the potentiostatic and galvanostatic electrolysis data. As our understanding of the factors expected to dominantly influence efficiency (such as buoyancy and bubble retention) did not line up with this result, several other possible causes were investigated such as variations in the gravitational field brought about by abnormalities in the parabolic flight manoeuvres; however, readings from the accelerometers in our setup and those provided by Novespace, did not explain the trends. Later, it was possible to replicate this behaviour in ground tests carried out post-flight, using an orbital shaking plate. It was noted that that the low resistance readings coincided with times when the electrolyte was in contact with the pressure sensor (Figure 4.7 cell A). This sensor was not in circuit with the potentiostat, though current loss was still possible as it was electrically grounded. On flight, the lower potential readings occurred when the g-level generated for each cell was close to microgravity. Video recordings taken at these g-levels, confirm that the force of gravity was insufficient to properly orient the headspace in the cell at the lid, and so it is reasonable to expect the same current loss through the pressure sensor to be occurring, giving the “low resistance” measurements. At higher centrifugal rotation speeds, the g-level was sufficient to orient the headspace over both the sensor and pressure release valve. Consequently, data collected in this “low resistance” region was discarded. Another point of note here is that each cell recorded slightly different values for the 1 g reading that was taken as a baseline, this was likely due to the minor differences in the cell assembly comprising of custom-made materials and electronics. Thus, to fairly represent the change in efficiency of the process with gravity, a mean value for 1 g was first calculated. The percentage change of current/potential at different g-levels from 1 g was then averaged to give a value that was more representative of the trend with gravity. Figure 4.8 shows the results from this microgravity campaign, including measurements taken at both Lunar (0.166 g) and Martian (0.376 g) gravity. Error bars are shown where multiple datapoints were collected, except for at 1 g, since the values on the graph are average % change from the mean at this g-level.

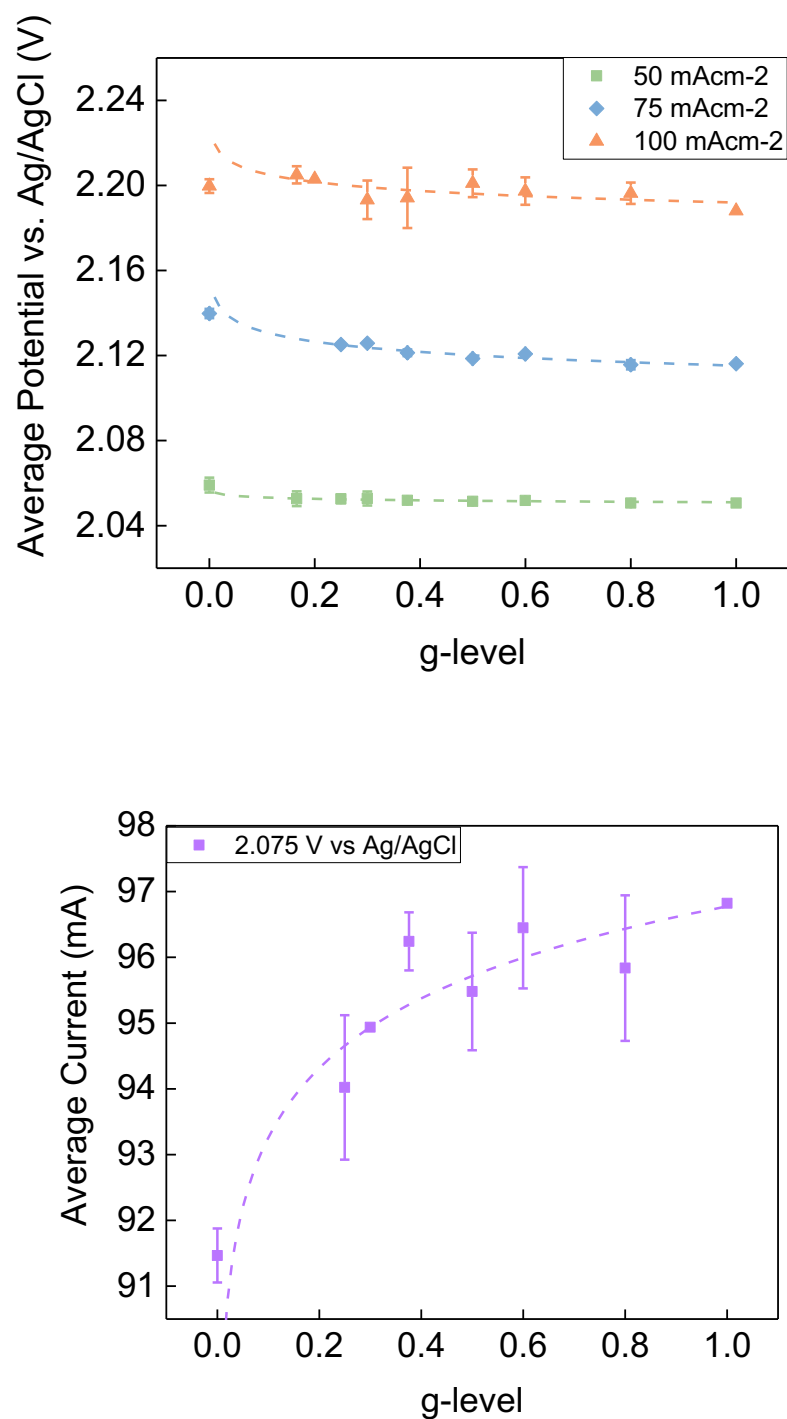


Figure 4.8: (Top) Average potentials and (bottom) average currents recorded when performing electrolysis at g-levels ranging from 0 to 1 g. To account for variations in the baseline for each cell, values were calculated as average % change from the average value recorded at 1g. Error bars are present when more than one recording was collected though, due to the issue previously discussed, this was not possible at every g-level. See appendix 1 for specifics on number of replicates which contributed to each datapoint.

Tables 4.3 & 4.4: Trendlines for electrolysis data recorded in microgravity.

Current Density	Trendline Equation	R ²
50 mA cm ⁻²	$y = -0.001 \cdot \ln(x) + 2.051$	0.848
75 mA cm ⁻²	$y = -0.007 \cdot \ln(x) + 2.115$	0.868
100 mA cm ⁻²	$y = -0.006 \cdot \ln(x) + 2.192$	0.496

Fixed Potential	Trendline Equation	R ²
2.075 V	$y = 1.528 \cdot \ln(x) + 96.775$	0.651

The microgravity data seen in figure 4.8 all seem to loosely follow a very slight logarithmic trend, which is in line with the previously reported model discussed in the introduction.^{30,33} However, it should be noted that in all conditions tested, the R² value indicates significant deviation in our results from an ideal logarithmic trend. It is likely that this is a consequence of the previously mentioned variation between each cell. This deviation is most glaring in the case of the 100 mA cm⁻² dataset, where it's adherence to a logarithmic trend at all is debateable. Furthermore, some of the biggest outlying values from these trends were recorded at 0 g. This is because every other measurement was taken from the centrifuge cells whereas microgravity measurements were taken from the two stationary cells. These deviations may have been mitigated had it been possible to record 1 g electrolysis measurements using the standing cells in between two parabolas on flight however, due to safety concerns, operation was not permitted on flight outside of parabolas.

4.3.3 Hypergravity Results

Like in the microgravity campaign, bulk electrolysis was carried out at three fixed current densities (50, 75 and 100 mA cm⁻²) and one fixed potential (2.075 V). In the hypergravity range investigated (from 1 to 8 g), the data recorded across all electrolysis conditions still followed a logarithmic trend (Figure 4.9).

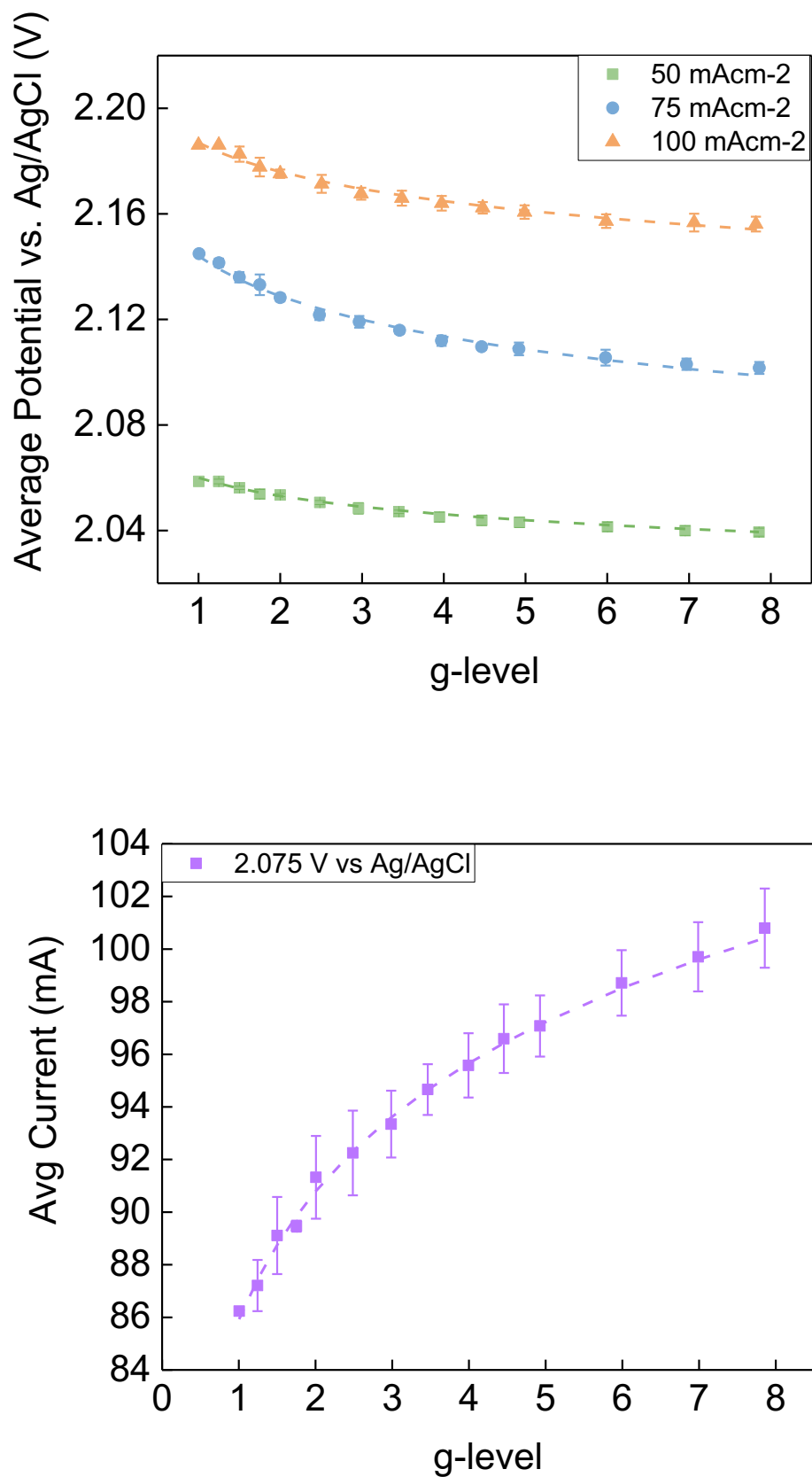


Figure 4.9: (Top) Average potentials and (bottom) average currents recorded when performing electrolysis at g-levels ranging from 1 to 8 g.

Tables 4.5 & 4.6: Trendlines for electrolysis data recorded in hypergravity range.

Current Density	Trendline Equation	R ²
50 mA cm ⁻²	$y = -0.010 \cdot \ln(x) + 2.060$	0.994
75 mA cm ⁻²	$y = -0.022 \cdot \ln(x) + 2.144$	0.988
100 mA cm ⁻²	$y = -0.016 \cdot \ln(x) + 2.187$	0.983

Fixed Potential	Trendline Equation	R ²
2.075 V	$y = 7.045 \cdot \ln(x) + 85.9$	0.9827

The data points collected here are much more in line with their respective logarithmic trend and, as can be seen by the small error bars in Figure 4.9, had much less variation at each given g-level. The greater error seen in the microgravity data is most likely due to a combination of factors. During parabolic flight, the spinning cells would be subject to vibrations of the centrifuge, in addition to imperfect microgravity conditions brought about by minor turbulence encountered by the aircraft. These both introduce a degree of variance that would not be present in the ground-based hypergravity measurements. It is likely then that this is the cause of difference in consistency across the two datasets. An interesting observation from this data is that, over this range, the change is greater in the potentiostatic experiment than it is in the galvanostatic runs. From 1 to 8 g the potential requirement of the electrolysis decreases by 0.9-2%, over the same range the current at 2.075 V increases by ~17%. This indicates that the rate of oxygen production in a system can be drastically improved through minor increases in the overpotential applied across the cell.

4.3.4 Extrapolation from Microgravity to Hypergravity

In the results collected in both hypergravity and microgravity, the relationship between electrolysis efficiency and gravity follows a logarithmic trend. If there is congruence in these trends, and results from hypergravity could be extrapolated to gravity levels below 1 g, then the feasibility of different electrolytic systems can be predicted without the need for costly testing programmes by lower gravity methods. For this to be the case, there must be

continuity on how gravity is affecting the process at g-levels below and above Earth's gravity. Indeed, there is already evidence to suggest that this "gravitational continuum" is valid for certain biological systems.³⁵

To ascertain if our results follow this principle of continuity, and prove that the response to gravity shown in hypergravity electrolysis data can be used to predict the performance of the process in a microgravity environment, the percentage change from 1 g in each data set across both studies was plotted (Figure 4.10). General observations that can be made here are that as you reduce the gravity level from 1 g to our lowest measurement at 0.166 g the potential requirement to meet each set current increases, whereas over this range we see a decrease in the current that is produced when applying a fixed potential. Likewise, if you increase the gravity level from 1 g up to 8 g, we see a decrease in the potential requirement of the galvanostatic process and promoted currents at a fixed potential. These results are in line with previously reported studies and can be attributed to the formation of a resistive layer of deposited gas bubbles that are generated throughout the electrolysis. Further analysis on the bubble behaviour throughout this experiment carried out by B. Lomax and P. A. Burke confirmed that formation of a frothy layer of retained bubbles was more prevalent at the lower gravity levels, with electrode coverage gradually decreasing as the g-level is increased.³⁶ The electrolysis data taken in tandem with this bubble analysis suggest that electrode coverage due to bubble retention is the primary cause for the trends in our data. This would also explain why the datasets showing the greatest change across the range of tested gravity levels are those in which current flow & subsequent bubble production is highest, as has been observed in previous studies.^{19,21,37}

Tables 4.7: Predicted changes in the oxygen yield and energy cost of operating this procedure in an identical setup on the Moon or on Mars

	Moon		Mars	
	O ₂ Production	Energy Cost	O ₂ Production	Energy Cost
50 mA cm ⁻²		↑0.6%		↑0.3%
75 mA cm ⁻²		↑1.1%		↑0.4%
100 mA cm ⁻²		↑0.9%		↑0.5%
2.075 V	↓10%		↓6%	

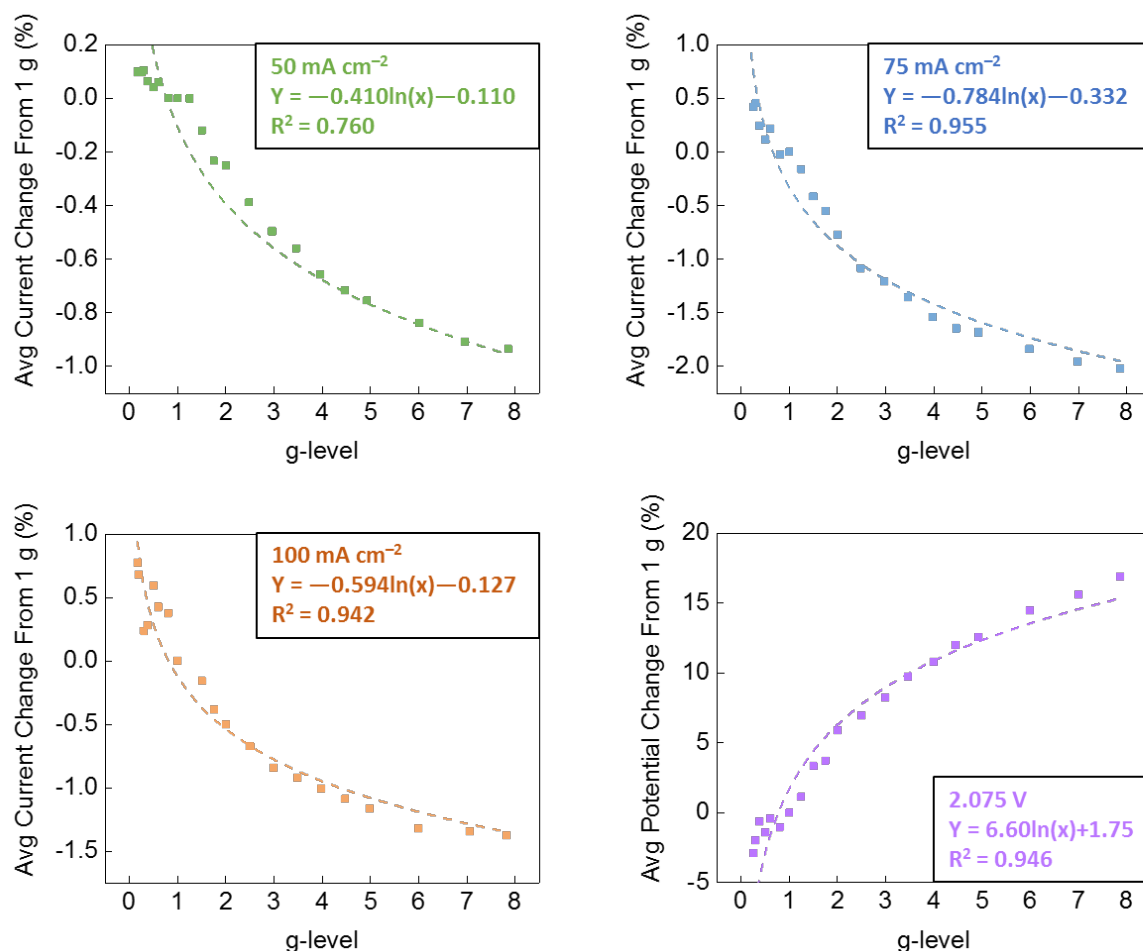


Figure 4.10: Percentage change in electrolysis efficiencies relative to Earth gravity from 0.166 – 8 g.

We also found that there is good agreement in the data, with the combined datasets for 50 mA cm⁻², 75 mA cm⁻², 100 mA cm⁻², and 2.075 V having R^2 values equal to 0.76, 0.955, 0.942, and 0.946 respectively. This agreement to a trend is notable, especially when considering the previously discussed factors that introduce variability to the microgravity study that are not present in the hypergravity data, and would not be present in the reduced-gravity environments where this process be implemented in future space missions. Indeed, it is possible that measurements carried out in these environments such as on the Moon (0.166 g) or Mars (0.376 g) may fall on the trend line with more accuracy.

As discussed in section 2.1.3, we can consider current and potential in an electrochemical reaction to be analogous to reaction rate & energy input respectively. The proportion of this current that fuels oxygen production is expressed as a Faradaic efficiency. If we assume

across all conditions that Faradaic efficiency is constant, then we can use the data to predict how the oxygen yield and energy cost of this process can change should the experiment be performed on the Moon or Mars (Table 4.7).

4.4 Conclusions

The work presented in this chapter includes the first published experimental verification of the efficiency of gas evolving electrolysis at gravity levels between 0 & 1 g. This was achieved using a small centrifuge, which induced different g-levels on cells in a microgravity background provided by parabolic flight. To do this, electrolytic cells were employed in which the anodic reaction evolves oxygen in tandem with copper deposition at the cathode. This electrolysis was tested at fixed currents of 50, 75 & 100 mA cm⁻², and at a fixed potential of 2.075 V vs Ag/AgCl. In this gravity range we see very slight logarithmic trends in the current response at fixed voltage, and potential requirement for electrolysis at constant current. In a series of ground-based tests, this centrifuge was then used to test this experiment in hypergravity up to 8 g. Logarithmic trends were again observed in all conditions. The formation of a gaseous insulating layer was identified as the primary factor governing these trends, with ohmic resistance increasing at lower gravity levels due to increased electrode coverage by this layer. At higher g-levels, bubble buoyancy is enhanced and so the growth of this layer is repressed.

Combining the data from both studies, expressed as average change from the 1 g baseline, it was found that all the data in each electrolysis condition follows logarithmic trends with good agreement. Crucially, this suggests that data collected in ground-based centrifugal cells at higher g-levels can be used to predict the efficiency in microgravity with some accuracy. If this holds true for other electrolytic systems, then a huge financial impediment may have been removed in the development of gas evolving processes for future space travel.

References

- 1 H. W. Jones, *48th Int. Conf. Environ. Syst.*, 2018, 81.
- 2 M. B. Duke, B. R. Blair and J. Diaz, *Adv. Sp. Res.*, 2003, **31**, 2413–2419.
- 3 R. J. Davenport, F. H. Schubert and D. J. Grigger, *J. Power Sources*, 1991, **36**, 235–250.
- 4 G. Z. Chen, D. J. Fray and T. W. Farthing, *Nature*, 2000, **407**, 361–365.
- 5 *US Pat. WO1999064638A1*, 2004.
- 6 S. Jiao and D. J. Fray, *Metall. Mater. Trans. B*, 2010, **41**, 74–79.
- 7 G. Z. Chen, *Trans. Institutions Min. Metall. Sect. C Miner. Process. Extr. Metall.*, 2015, **124**, 96–105.
- 8 B. A. Lomax, M. Conti, N. Khan, N. S. Bennett, A. Y. Ganin and M. D. Symes, *Planet. Space Sci.*, 2020, **180**, 104748.
- 9 C. Schwandt, J. A. Hamilton, D. J. Fray and I. A. Crawford, *Planet. Space Sci.*, 2012, **74**, 49–56.
- 10 K. Kilby, L. Centeno, G. Doughty, S. Mucklejohn and D. Fray, *Sp. Resour. Roundtable VIII*, 2006, 64–65.
- 11 K. T. Kilby, S. Jiao and D. J. Fray, *Electrochim. Acta*, 2010, **55**, 7126–7133.
- 12 R. Barnett, K. Tripuraneni Kilby and D. J. Fray, , DOI:10.1007/s11663-008-9219-6.
- 13 2009.
- 14 S. Jiao, K.-N. P. Kumar, K. T. Kilby and D. J. Fray, *Mater. Res. Bull.*, 2009, **44**, 1738–1742.
- 15 T. Nohira, K. Yasuda and Y. Ito, *Nat. Mater.*, 2003, **2**, 397–401.
- 16 G. Z. Chen, E. Gordo and D. J. Fray, *Metall. Mater. Trans. B Process Metall. Mater. Process. Sci.*, 2004, **35**, 223–233.

- 17 D. S. McKay, G. Heiken, A. Basu, G. Blanford, S. Simon, R. Reedy, B. M. French and J. Papike, in *Lunar Sourcebook*, Cambridge University Press, 1991, pp. 285–356.
- 18 A. Taqieddin, R. Nazari, L. Rajic and A. Alshawabkeh, *J. Electrochem. Soc.*, 2017, **164**, E448–E459.
- 19 M. Sakurai, Y. Sone, T. Nishida, H. Matsushima and Y. Fukunaka, *Electrochim. Acta*, 2013, **100**, 350–357.
- 20 A. Iwasaki, H. Kaneko, Y. Abe and M. Kamimoto, *Electrochim. Acta*, 1998, **43**, 509–514.
- 21 H. Matsushima, T. Nishida, Y. Konishi, Y. Fukunaka, Y. Ito and K. Kuribayashi, *Electrochim. Acta*, 2003, **48**, 4119–4125.
- 22 D. Kiuchi, H. Matsushima, Y. Fukunaka and K. Kuribayashi, *J. Electrochem. Soc.*, 2006, **153**, E138.
- 23 H. Matsushima, D. Kiuchi, Y. Fukunaka and K. Kuribayashi, *Electrochem. commun.*, 2009, **11**, 1721–1723.
- 24 G. Sakuma, Y. Fukunaka and H. Matsushima, *Int. J. Hydrogen Energy*, 2014, **39**, 7638–7645.
- 25 K. Brinkert, M. H. Richter, Ö. Akay, J. Liedtke, M. Giersig, K. T. Fountaine and H.-J. Lewerenz, *Nat. Commun.*, 2018, **9**, 2527.
- 26 H. Kaneko, K. Tanaka, A. Iwasaki, Y. Abe, A. Negishi and M. Kamimoto, *Electrochim. Acta*, 1993, **38**, 729–733.
- 27 Z. Derhoumi, P. Mandin, H. Roustan and R. Wüthrich, *J. Appl. Electrochem.*, 2013, **43**, 1145–1161.
- 28 P. Mandin, Z. Derhoumi, H. Roustan and W. Rolf, *Electrochim. Acta*, 2014, **128**, 248–258.
- 29 A. Bashkatov, X. Yang, G. Mutschke, B. Fritzsche, S. S. Hossain and K. Eckert,

- Phys. Chem. Chem. Phys.*, 2021, **23**, 11818–11830.
- 30 M. Wang, Z. Wang and Z. Guo, *Int. J. Hydrogen Energy*, 2010, **35**, 3198–3205.
- 31 H. Cheng, K. Scott and C. Ramshaw, *J. Electrochem. Soc.*, 2002, **149**, D172.
- 32 L. Lao, C. Ramshaw and H. Yeung, *J. Appl. Electrochem.*, 2011, **41**, 645–656.
- 33 H. Cheng and K. Scott, *J. Electroanal. Chem.*, 2003, **544**, 75–85.
- 34 Airbus A310 Zero G: gravity-free aircraft by Novespace,
<https://www.airzerog.com/the-airbus-a310-zero-g/>, (accessed 26 March 2020).
- 35 C. E. Wade, *Adv. Space Biol. Med.*, 2005, **10**, 225–245.
- 36 B. A. Lomax, G. H. Just, P. J. McHugh, P. K. Broadley, G. C. Hutchings, P. A. Burke, M. J. Roy, K. L. Smith and M. D. Symes, *Nat. Commun.*, 2022, **13**, 583.
- 37 M. Wang, Z. Wang and Z. Guo, *Int. J. Hydrogen Energy*, 2009, **34**, 5311–5317.

Chapter 5:

Sonoelectrochemical Degradation of Diclofenac

Acknowledgements and Declarations

The work presented in this chapter was carried out as part of a loose collaboration with Dr. Wei Lun Ang, whereby a parallel study was carried out in his lab with the aim of scaling up the process. As such, some design decisions such as electrode material choice were made in conjunction with both Dr. Wei Lun Ang and Dr. Mark D. Symes. This chapter does not however contain any work from the study performed by Dr. Wei Lun Ang; all work presented is my own. I also would like to thank Dr. Gangi Reddy for his assistance in optimising the LC-MS method used.

Abstract

Owing to its widespread global use as an anti-inflammatory agent, diclofenac contaminated wastewaters are becoming increasingly prevalent. Efficient wastewater degradation methods for the drug are therefore vital; even more so due to the fact it has been found to be harmful to aquatic life. In the research described herein, an ultrasound assisted electrochemical method is used to degrade diclofenac, finding a 64% decrease in DCF concentration using 80 kHz ultrasound coupled with 5 mA cm^{-2} constant electric current. The use of a similar method has been previously reported using a high frequency sonication in low concentration solutions of diclofenac. Here we test the efficacy of the procedure in much higher concentrations of the pharmaceutical, using low frequency sonication generated using an ultrasonic bath.

5.1 Introduction

One of the most commonly administered non-steroidal anti-inflammatory drugs, used both on humans and livestock, is diclofenac (2-(2-(2,6-dichlorophenylamino)phenyl)acetic acid, DCF). Available commercially in both a gel and tablets, this drug has an estimated annual consumption of 940 tonnes which has led to a detection of DCF as a pollutant in water sources across the globe.¹ Illustrating the widespread nature of this pollution González-Alonso *et al.* tested water samples collected in one of the world's most remote regions, the Antarctic Peninsula.² In this study, diclofenac was detected in concentrations up to $\sim 15 \mu\text{g L}^{-1}$ and this is not an isolated result; similarly high concentrations of the drug have been detected in water samples taken in Malaysia (79.89 ng L^{-1}),³ Poland (92.6 ng L^{-1}),⁴ the UK & Ireland (195 ng L^{-1} , 460 ng L^{-1}),^{5,6} Portugal (241 ng L^{-1}),⁷ China (843 ng L^{-1}),⁸ and Saudi Arabia (3000 ng L^{-1}).⁹ This contamination is more concerning when considering the deleterious effect that even low concentrations of diclofenac can have on the health of local fauna. Example studies have found that diclofenac contamination has led to significant drops in vulture population across south Asia,^{10,11} tissue damage and cytological changes in rainbow trout,^{12–15} and causing renal issues in other fish such as the three-spined stickleback.¹⁶ With specific regard for how this contamination could have an ill-effect on human health, there is strong evidence from recent studies to suggest that DCF can cause gastrointestinal issues, and may lead to neuro-, hepa-, and bone marrow toxicity issues.¹⁷ In response to this, the drug was added to the European Union's watchlist for water monitoring.¹⁸

It is no surprise then that the degradation of diclofenac has been the subject of considerable study using a variety of techniques.¹⁹ As discussed in chapter 1, the coupling of ultrasound to electrolysis is a well-established approach for degradation within this field as it generally yields an enhancement of the electrochemical process, without the requirement of additional “environmentally unfriendly” chemicals. What's more, the tunability of applied sonication adds a degree of versatility to the experiment which has often led to the pollutant degradation process being more energy efficient, safer, and able to be operated in milder conditions. Nonetheless, although photolytic,^{20–24} photocatalytic,^{25–31} ozonation,^{31–36} Fenton,^{25,31,37–39} radiolysis,^{40–44} sonolysis,^{30,34,45–47} and electrochemical^{48–50} methods have all been thoroughly investigated, only one study, by Finkbeiner *et al.*, has been published using a combined sonoelectrochemical method for the degradation of diclofenac.⁵¹ In their experiment, an ultrasonic transducer was fitted to the bottom of the reaction vessel and was used to generate

high-frequency ultrasound at 850 kHz. Applying this sonication, in conjunction with a potentiostatic electrolysis at 7.2 V using two BDD electrodes, the researchers observed optimal DCF degradation of ~93 % ($\text{DCF}_{\text{conc}} = 50 \mu\text{g L}^{-1}$, $k = 0.505 \text{ min}^{-1}$). The authors arrive at these optimal conditions after assessing the influence of various experimental parameters such as applied voltage, pH, and electrode positioning.

The experimental setup used in this chapter differs from the work of Finkbeiner *et al.* in two primary ways; the nature of the applied sonication and the electrode material. Whilst in the previous report the researchers opted to use very high frequency sonication (850 kHz) generated using a transducer connected directly to their reaction vessel, our work utilises ultrasound at only 37 & 80 kHz applied by placing our reaction vessel in an ultrasonic bath. As touched upon in chapter 1 (section 1.2.2), ultrasonic bath emitters typically yield lower rates of radical generation as the reaction mixture is most often in a separate vessel submerged in the bath, and so the sound waves are dampened by the material which makes up the vessel. This issue is not present when the transducer is attached to the reactor albeit at the expense of homogeneity, with the acoustic field distributed unevenly throughout the reactor. In electrode choice, Finkbeiner *et al.* opted to use BDD, an electrode material used extensively in electro-oxidation processes, however, this material has a large capital cost which could be an impediment to the scaling up of the process. The primary anodic material used in the research herein is Pt-Ti, which is available at a reduced cost when compared to BDD. In short, the dearth of published results using this approach to remove diclofenac from water leaves a lot of room for the process to be optimised, in both an economical and performance sense; in the research presented herein we seek to do that.

5.2 Experimental

5.2.1 Materials

The Pt/Ti anodes were cut from platinised titanium fibre felt purchased from FuelCellStore. The cathodes were cut from 0.06 mm thick Dexmet Ti mesh (2TI4-031FA). The diclofenac sodium (>95%), sodium acetate (99%), sodium sulfate (99%) were purchased from Alfa Aesar. The dimethylmalonic acid (98%) was purchased from Merck. All aqueous solutions were prepared using ultrapure grade deionised water (18.2 M Ω ·cm) obtained from a Sartorius Arium Comfort combined water system.

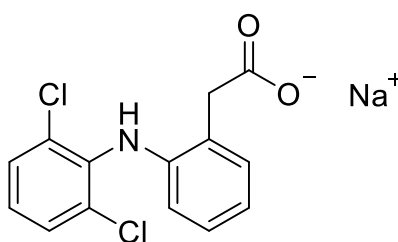


Figure 5.1: Structure of the sodium salt of diclofenac.

5.2.2 Cell Setup

Electrochemical reactions were carried out in a cylindrical glass cell (diameter X.X), using a standard two-electrode configuration (working electrode surface area = 4 cm², counter electrode working area = ~8 cm²) arranged with ~16 mm separation. Unless otherwise stated, experiments were carried out in a 500 mg L⁻¹ solution of diclofenac sodium in 0.3 M Na₂SO₄. Both electrodes were connected to an Admiral Instruments Squidstat Plus potentiostat. Ultrasound assisted, and heated electrolysis experiments were performed in a Fisher Scientific 15050 ultrasonic bath (Figure 5.2); in these runs the cell was always clamped into the same position in the bath and submerged to the same depth. The increase in temperature of the water in the bath over 1 hour of sonication was up to 50 °C, as such this was the chosen set temperature for the heated experiments. To control for the promoted mass transfer in solution that occurs during sonication, silent runs were performed using the same cell but fitted with a magnetic stirrer bar and stirred at a rate of 150 rpm using an IKA-RCT digital stirring plate.

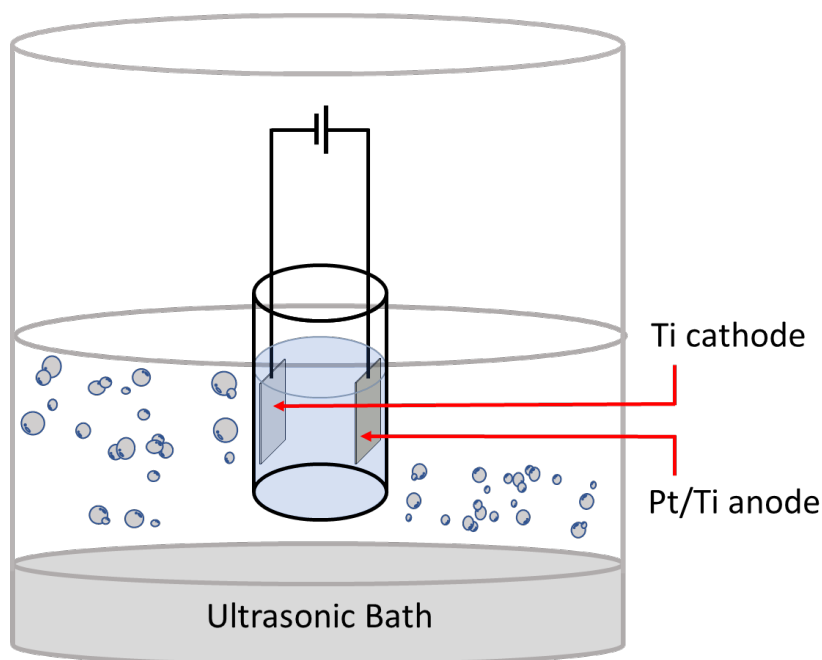


Figure 5.2: Diagram of typical experimental setup when using a combined sonoelectrochemical approach consisting of a conventional two-electrode cell submerged in a ultrasonic bath.

5.2.3 Electrochemical Characterisation

Electrochemical impedance spectroscopy (EIS) and cyclic voltammetry (CV) measurements were recorded using Admiral Instruments Squidstat Plus. Data was recorded and analysed using Squidstat User Interface software (v2.0 beta, Admiral Instruments (Tempe, Arizona, USA)). Unless otherwise stated, the EIS data was recorded using the following parameters: starting frequency = 20 kHz, ending frequency = 10 mHz, DC bias = 20 mA, AC excitation amplitude = 10 mA. The EIS data was fitted to equivalent circuits (Figure 5.3) using AfterMath (v1.5.9644, Pine Research Instrumentation Inc. (Durham, NC, USA)). For the 80 kHz US-EC runs, the data was fitted to the equivalent circuit, $R_1 + Q_1/R_2$ where R_1 , corresponds to the series resistance of the cell (R_s), R_2 corresponds to the polarisation resistance of the cell (R_p), and Q_1 represents a constant phase element. Due to the apparent secondary process in the 37 kHz US-EC data, the circuit was adjusted to $R_1 + Q_1/(R_2 + Q_2/R_3)$. The details of the components of the equivalent circuit are as follows: R_1 , which corresponds to the series resistance of the cell (R_s); R_2 , which corresponds to the polarisation resistance corresponding to the first process (R_{p1}); R_3 , which corresponds to the polarisation

resistance of the second process (R_{p2}); Q_1 & Q_2 , which represent constant phase elements. As is discussed later in this chapter, the secondary process is most likely passivation of the anode due to deposition. For this process to occur, sufficient charge must first pass to polarise the cell (the resistance of which is R_2), for that reason both R_3 and Q_3 must be in series with R_2 . This circuit has also been used previously to fit data where a similar inhomogeneous passive film is formed through electrodeposition.⁵²

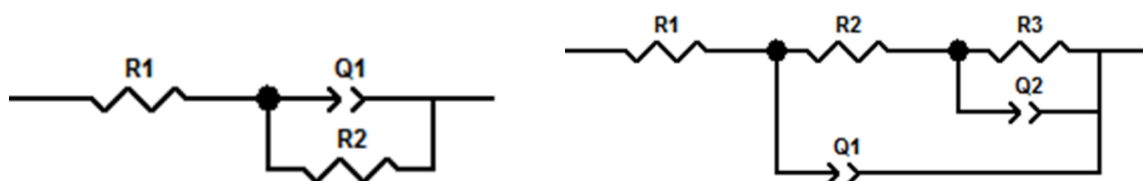


Figure 5.3: Circuit diagrams of the equivalent circuits used to fit EIS data from: (left) 80 kHz US-EC conditions and (right) 37 kHz US-EC conditions.

Table 5.1: Complete list of equivalent circuit parameters used to fit EIS data.

Condition	R_1 (Ω)	R_2 (Ω)	R_3 (Ω)	Q_1 [Q] ($\mu\text{s}^\alpha/\Omega$)	Q_1 [α]	Q_2 [Q] ($\mu\text{s}^\alpha/\Omega$)	Q_2 [α]
80 kHz US-EC	50.00	8.33		1000	0.92		
37 kHz US-EC	48.00	19.30	4.27	42.19	0.76	1000	1

5.2.4 UV-Vis Spectrometry Procedure

UV-Vis spectra were recorded on solutions of DCF at concentrations ranging from 0–1 mM in 0.1 M NaOH using a Cary 60 UV-Vis spectrophotometer. Unless stated otherwise, the data was collected using the following parameters: starting wavelength = 400 nm, ending wavelength = 190 nm, scan rate = 200 nm min⁻¹. The concentration of DCF was determined by noting the peak absorbance value ($\lambda_{\text{max}} = 275$ nm), and a calibration curve was thus

assembled. The concentration of the pollutant throughout the reaction was then determined by referencing the absorbance at this wavelength to the calibration curve.

5.2.5 NMR Procedure

NMR samples were prepared using the following composition: 0.3 mL sample, 0.1 mL internal standard and 0.1 mL. Samples were analysed in at 296K in a Bruker 400 MHz spectrometer.

DCF: ^1H NMR (400 MHz, Deuterium Oxide) δ 7.42 (d, $J = 8.1$ Hz, 2H), 7.20 (dd, $J = 7.4$, 1.6 Hz, 1H), 7.12 – 7.03 (m, 2H), 6.90 (td, $J = 7.5$, 1.1 Hz, 1H), 6.43 (dd, $J = 7.5$, 1.0 Hz, 2H), 3.60 (s, 2H).

Dimethylmalonic Acid: ^1H NMR (400 MHz, DMSO- d_6) δ 12.7 (s, 2H), δ 1.3 (s, 6H)

5.2.6 LCMS Procedure

40 μL samples of the electrolyte were taken from the reaction at 0, 15, 30, 45 and 60 mins. These samples were then diluted using ultrapure water to a volume of 2 mL and filtered using a Fisherbrand PTFE syringe filter (diameter = 13 mm, pore size = 0.2 μm) before analysis. The LCMS measurements were performed using an Agilent 1260 Infinity II machine fitted with a Shim-pack XR-ODS column (2.0 mm i.d. x 50 mm). The procedure was carried out using a mixture of two solvents: A (0.1% (v/v) formic acid in ultrapure water) and B (0.1% (v/v) formic acid in methanol) at a ratio of A:B equal to 1:4. The measurements were recorded using a flow rate of 0.3 mL min^{-1} and gas temperature of 300 $^\circ\text{C}$. Using these parameters, the retention time of DCF was 2.7 mins.

5.2.7 SEM Procedure

Samples were cut from the electrodes and loaded onto 12 mm AGAR scientific conductive carbon tabs. Images were obtained with acceleration voltages between 12 kV and 20 kV.

5.3 Results and Discussion

5.3.1 Preliminary DCF Degradation Experiments

For monitoring the degradation of DCF, several different methods were trialed. Firstly, UV-Vis spectroscopy was tested on low concentration samples of diclofenac (1 mM DCF in 0.1 M NaOH). In this instance, the degradation process was carried out in a 3-electrode cell consisting of a BDD working electrode ($S.A. = 0.85 \text{ cm}^2$), a Ti mesh counter electrode, and a Pt wire pseudo-reference electrode. Cyclic voltammetry measurements taken in this setup indicated two oxidation peaks for diclofenac at ~ 0.5 and 1.4 V (appendix 2). Figure 5.4 shows the concentration of DCF after 1 hour of degradation at a current density of 10 mA cm^{-2} under different parameters.

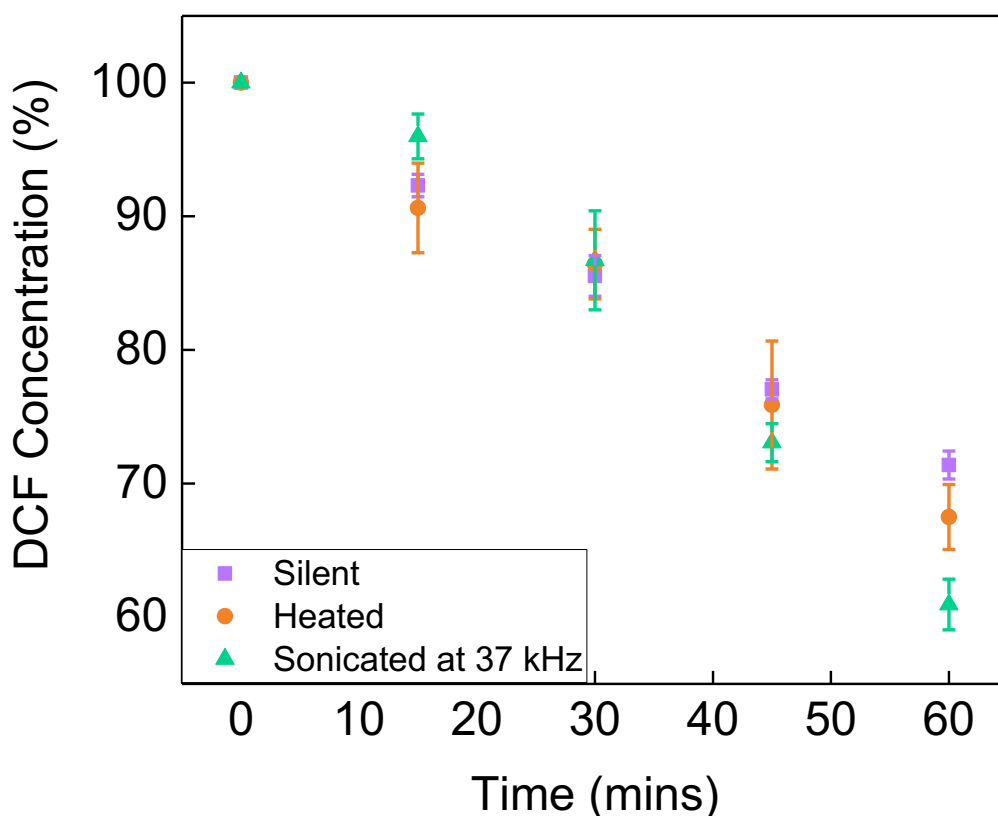


Figure 5.4: Results from electrolysis of 1 mM DCF in 0.1 M NaOH at a current density of 10 mA cm^{-2} in three different sets of conditions: silent runs (purple line) where solutions were stirred at 730 rpm using a magnetic stirring bar, stirred and heated runs (orange line) where solutions were stirred at 730 rpm using a magnetic stirring bar and submerged in an oil bath set to $50 \text{ }^\circ\text{C}$, and sonicated runs (green line) where the solutions were sonicated at a frequency of 37 kHz in an ultrasonic bath.

Averaged over three repeats, DCF concentration was reduced by 29% in the silent runs, 33% in the stirred and heated runs, and 39% in the 37 kHz US-EC runs, however, the extent of degradation remained within error of each other until the last measurement taken. The final measurement suggested that sonication may possibly promote the degradation of this compound; in an attempt to promote this enhancement, the supporting electrolyte was changed from NaOH to Na₂SO₄. As mentioned in section 1.2.4, sodium sulfate is a widely used background electrolyte in ultrasound-assisted decontamination methods due to its tendency to form highly oxidising sulfate species under the action of an ultrasonic field. The use of this background electrolyte also prevents large variance in the pH across the experiment. However, the sulfate anion absorbs strongly in the spectral range that DCF also absorbs. This led to difficulties in assembling congruent measurements for a calibration curve and ultimately lead to a large variance in our results when testing for DCF samples in the reaction mixture. For this reason, the UV-Vis approach was abandoned.

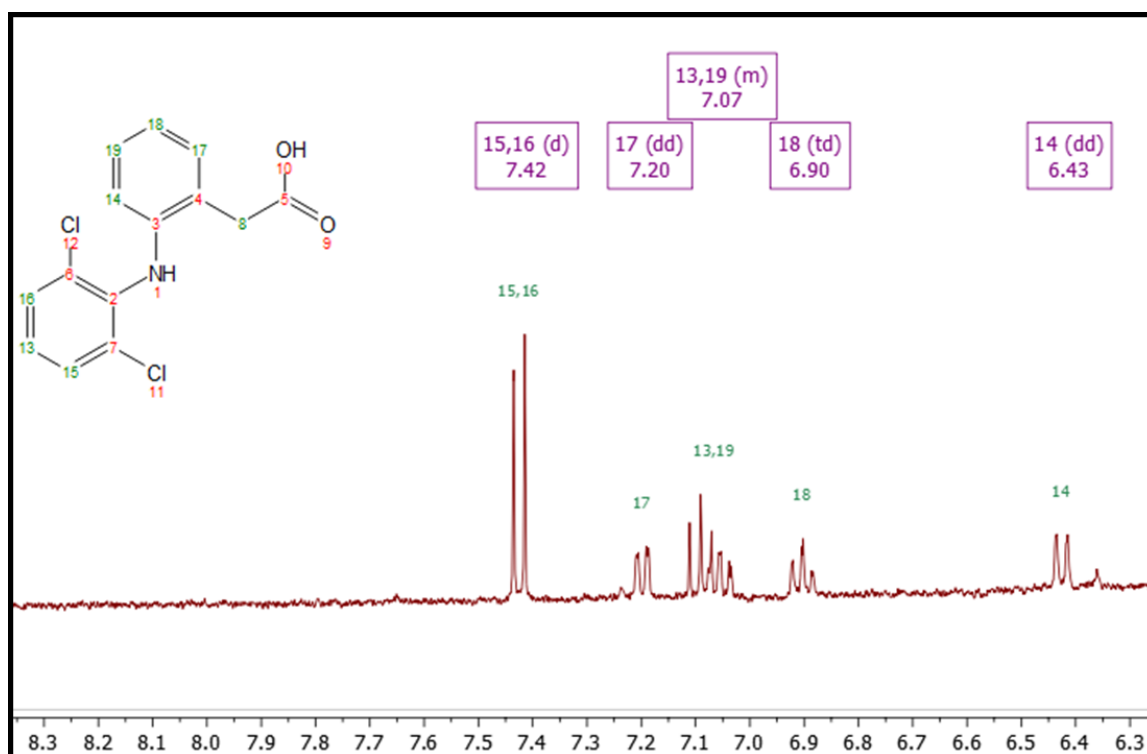


Figure 5.5: Assigned NMR spectra of DCF in D₂O. When using internal standard, DCF was referenced using the doublet at 7.42 ppm assigned to the protons at position 16 and 17 on the structure. The signal corresponding to the two protons at position 8 is not shown due to obfuscation by the water peak.

To avoid further false positive results, NMR spectroscopy was then employed which allowed the use of sodium sulfate as a background electrolyte. In this set of experiments, an internal NMR standard of known concentration was used to quantify DCF throughout the degradation. Additionally, due to logistical difficulties experienced by our collaborators in Malaysia, the working electrode material was changed from BDD to Pt/Ti. The typical sample composition was 0.3 mL of the reaction mixture, 0.1 mL of internal standard and 0.1 mL of deuterated solvent so naturally, the peak associated with water (4.58 ppm) dominated the spectrum in each recording; thus, identifying an appropriate internal standard was crucial. Initially, sodium acetate was used as its associated ^1H NMR peak as reported was sufficiently downfield so as not to overlap with any of the DCF signals or the signal associated with water.⁵³ However, when this standard was used, two signals would arise; this was ascribed to protonation of acetate to acetic acid.

Dimethylmalonic acid was then trialled. When preparing samples using previously stated composition, both the DCF and standard peaks could be identified and integrated though both had miniscule intensity when compared to the large water peak, leading to inaccurate results. To address this, the concentration of DCF was increased from 1 mM (318 mg L^{-1}) to 1.6 mM (500 mg L^{-1}). Unfortunately, at higher concentrations solubility issues were commonly encountered. To mitigate this, the method was altered such that the solvent in each sample from the reaction was first removed using a rotary evaporator. This allowed the use of a variety of different deuterated solvents; deuterated water (D_2O), methanol (CD_3OD) and acetone ($(\text{CD}_3)_2\text{CO}$) were all assessed, yet none could fully dissolve all the solid components of the test sample.

5.3.2 LC-MS Analysis

When the method of evaluating DCF concentration was switched to LC-MS, consistent and repeatable results were finally possible. Figure 5.6 shows the electrolytic degradation of DCF over 1 hour at a fixed current density of 5 mA cm^{-2} , using a Pt/Ti WE & Ti mesh CE, under several different experimental conditions (section 5.2.2). When the electrolysis was coupled with sonication at 80 kHz, an optimal degradation of 64% was achieved. When the solution was heated in a water bath at $50 \text{ }^\circ\text{C}$, the DCF degradation was 55%. An interesting result from this experiment was that when the electrolysis was coupled with ultrasonic

irradiation at 37 kHz the degradation efficiency was 37%, which was almost identical to the performance in the silent experiment.

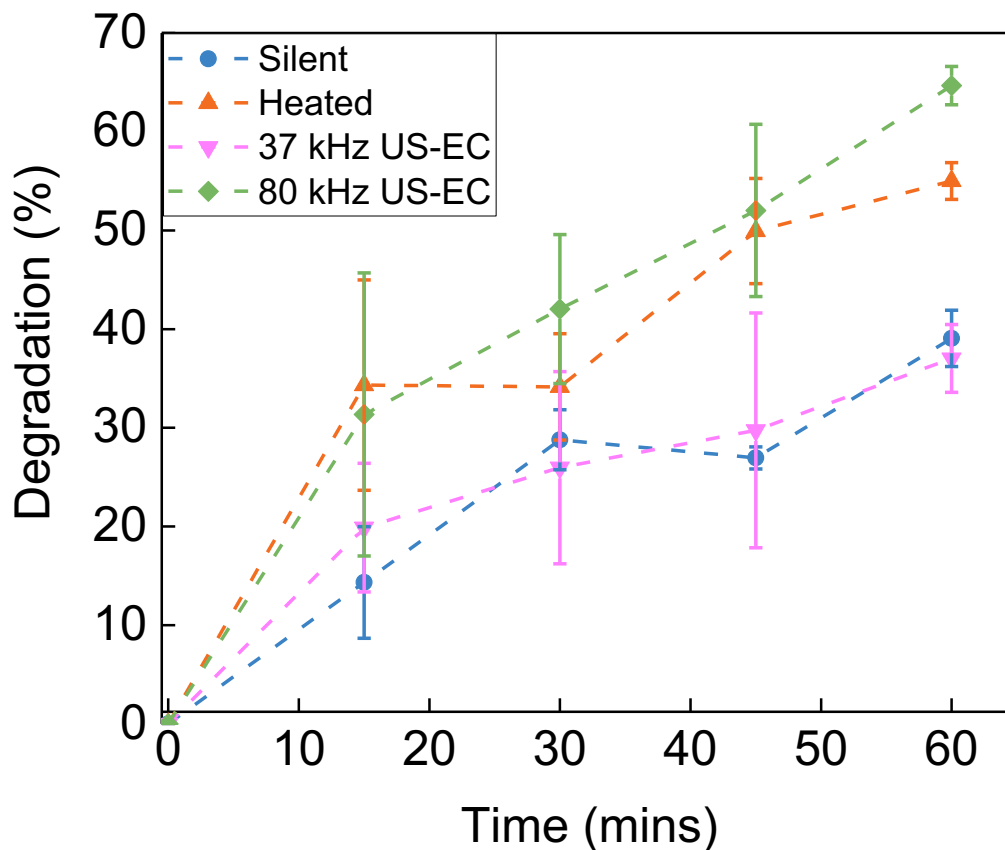


Figure 5.6: Results from electrolysis of 500 mgL^{-1} DCF in $0.3 \text{ M Na}_2\text{SO}_4$ at a current density of 5 mA cm^{-2} in four different sets of conditions: silent runs (blue line) where solutions were stirred at 150 rpm using a magnetic stirring bar in the absence of sonication, heated runs (orange line) where solutions were submerged in a water heated to $50 \text{ }^\circ\text{C}$, 37 kHz US-EC (pink line) and 80 kHz US-EC (green line) where the solutions were sonicated at these frequencies in an ultrasonic bath.

Though it could have been anticipated that the degradation of diclofenac would be promoted with increasing frequency of sonication, it is entirely unexpected that coupling the process to 37 kHz sonication would not offer an enhancement over the silent run. To ascertain a possible cause for this, further characterisation of the technique was performed using EIS. Figure 5.7 displays Nyquist plots from EIS measurements recorded at a DC current identical to that which was used in the previous degradation experiments.

Table 5.2: Series resistance, R_s , and polarisation resistance, R_p , obtained from EIS analysis of DCF degradation under different conditions.

Condition	R_s (Ω)	R_{p1} (Ω)	R_{p2} (Ω)	R_{Total} (Ω)
80 kHz US-EC	50.00	8.33		58.33
37 kHz US-EC	48.00	19.30	4.27	71.57

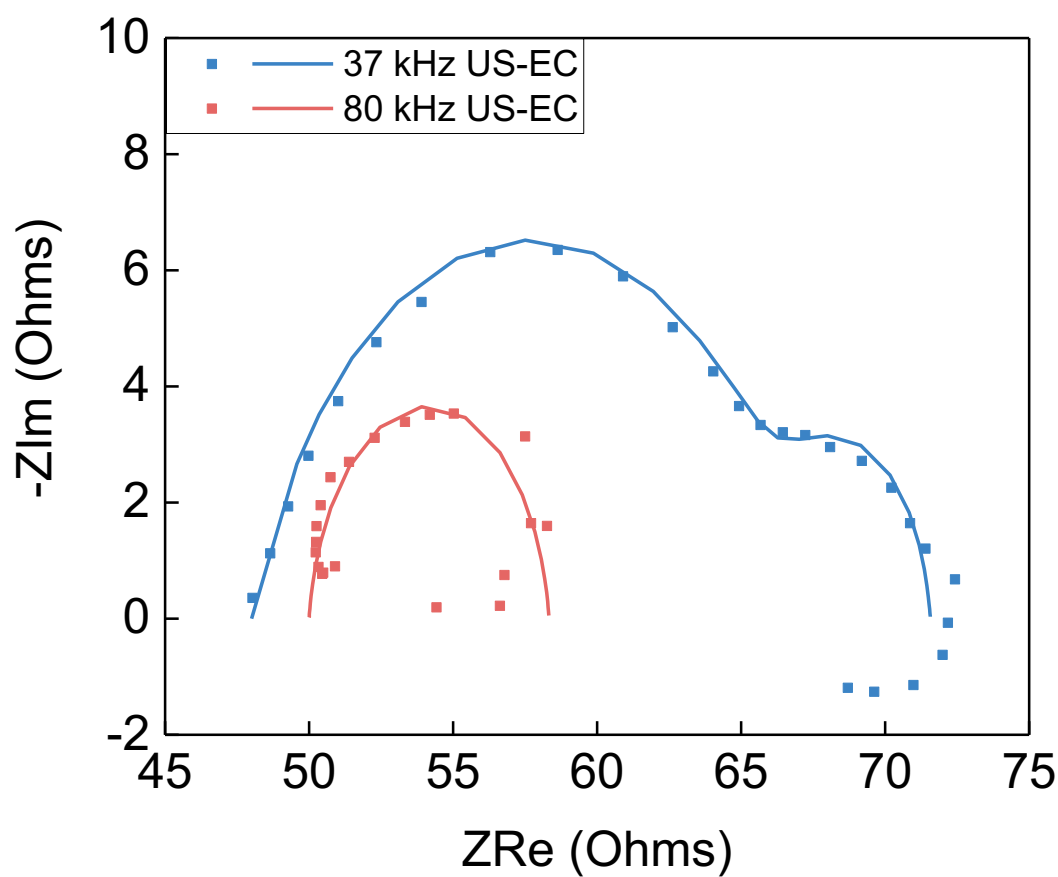


Figure 5.7. EIS comparison showing the Nyquist plots of the data collected during the process (markers) and their corresponding simulated fits (solid lines). The conditions tested were 5 mAcm^{-2} and sonication at 37 kHz (blue), and at 80 kHz (red).

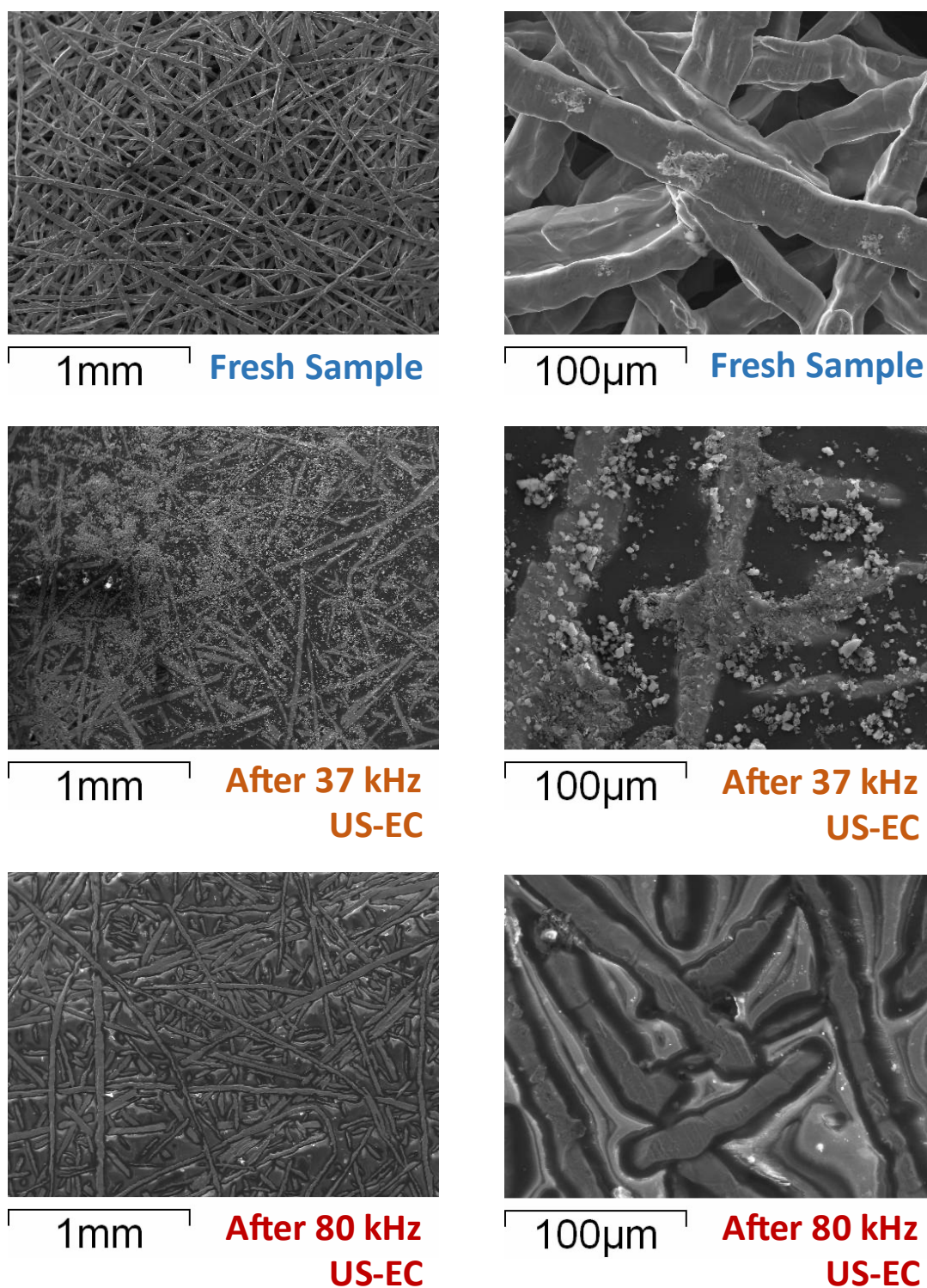


Figure 5.8: SEM images at indicated scale of a fresh Pt/Ti anode (top), of a Pt/Ti after use in a 37 kHz US-EC experiment (middle) of a Pt/Ti after use in a 80 kHz US-EC experiment (bottom).

As mentioned in section 3.3.2, R_s can be obtained from Figure 5.7 by considering where the semi-circle first intercepts the x-axis at high frequency. In an ideal setting, R_p is then simply

the difference between the high and low frequency intercepts of the x-axis. This holds for single semi-circle Nyquist plots which, as can be seen in Figure 5.7, only applies to the silent and 80 kHz US-EC conditions. The smaller semi-circle in the 37 kHz US-EC experiment indicates that a secondary process occurs under this condition. Fitting the data to equivalent circuits (section 5.2.3), it was found that both experiments had similar series resistances, R_s ; 48 Ω for the 37 kHz US-EC run, $\sim 50 \Omega$ for the US-EC experiment sonicated at 80 kHz. The primary difference then between the two conditions lies in the R_p value; for the 37 kHz US-EC run, an equivalent circuit with two separate R_p values was required to account for the two processes. For the 80 kHz US-EC experiments, the R_p value was 8.33 Ω . The sum of the two polarisation resistances calculated for the 37 kHz US-EC was significantly higher, at 23.57 Ω . Table 5.2 shows the complete breakdown of the EIS results.

As mentioned, the second semicircle seen in the 37 kHz EIS data is indicative of a secondary process occurring. Several possible causes were considered such as electrode decomposition, or the formation of an insulated layer due to deposition. To further investigate this, various SEM images were collected of the Pt-Ti anode after both 37 kHz & 80 kHz US-EC degradation runs, as well as of a fresh anode that had not been used (Figure 5.8). As can be seen in the images, the 37 kHz US-EC experiment results in extensive deposition on the surface of the electrode. Whilst deposition is still visible in the sample used in an 80 kHz US-EC run, it is not as severe. It is likely then that electrode passivation is the cause for the poor performance at 37 kHz, however, this does not explain why the deposition is greater at this frequency over 80 kHz. One of the key benefits in coupling sonication to electrochemical processes, is that often electrode passivation can be inhibited due to a “cleaning” of the surface via acoustic cavitation events.⁵⁴ It is also well established that the number of cavitation events is often increased at higher frequency. These two facts taken in tandem may explain our data; it is possible that at 80 kHz, the sonication is producing enough cavitation events to prevent electrode passivation whereas at 37 kHz, it is not.

Alternatively, it could be that the deposition observed in figure 5.8 was not accumulation of the oxidation products of diclofenac but rather a result of extensive electrode breakdown. As can be seen particularly in the 100 μm scale SEM image taken after a 37 kHz US-EC experiment, there is an observed roughness to the surface of the Pt-Ti fibres. It is possible that this roughness is an indication of electrode deterioration, rather than being due to the deposition of an inhomogeneous film. The poor diclofenac degradation at 37 kHz could then be explained by a more severe attack on the Pt/Ti anode in conditions when the cavitation

events are more violent. If more time had been available, it would have been beneficial to investigate and conclusively identify this cause.

5.3.3 Synergistic Index

As with many of the cases highlighted in chapter 1, a key benefit to this approach to pollutant degradation is that the coupling of sonolysis and electrolysis can yield results which indicate synergistic behaviour. This is dependent on several factors, such as current density and electrolyte concentration, and can be typically quantified by the synergistic index (S.I.) calculated by first determining the rate constant for each degradation process and then using equation 5.1 below. Based on the previous sonoelectrochemical study on diclofenac, and other persistent organic pollutants, pseudo-first order kinetics were assumed.^{51,55,56} An SI value greater than 1 is an indication of a synergistic relationship in the combined method.

$$SI = \frac{k_{US-EC}}{k_{EC} + k_{US}} \quad (5.1)$$

Table 5.3: Calculated rate constants and synergistic indices for the sonoelectrochemical processes in both frequencies.

Condition	5 mAcm ⁻²	80 kHz	80 kHz + 5 mAcm ⁻²	37 kHz	37 kHz + 5 mAcm ⁻²
Rate Constant (min ⁻¹)	-0.0083	-0.0037	-0.0174	-0.0024	-0.0083
SI			1.45		0.77

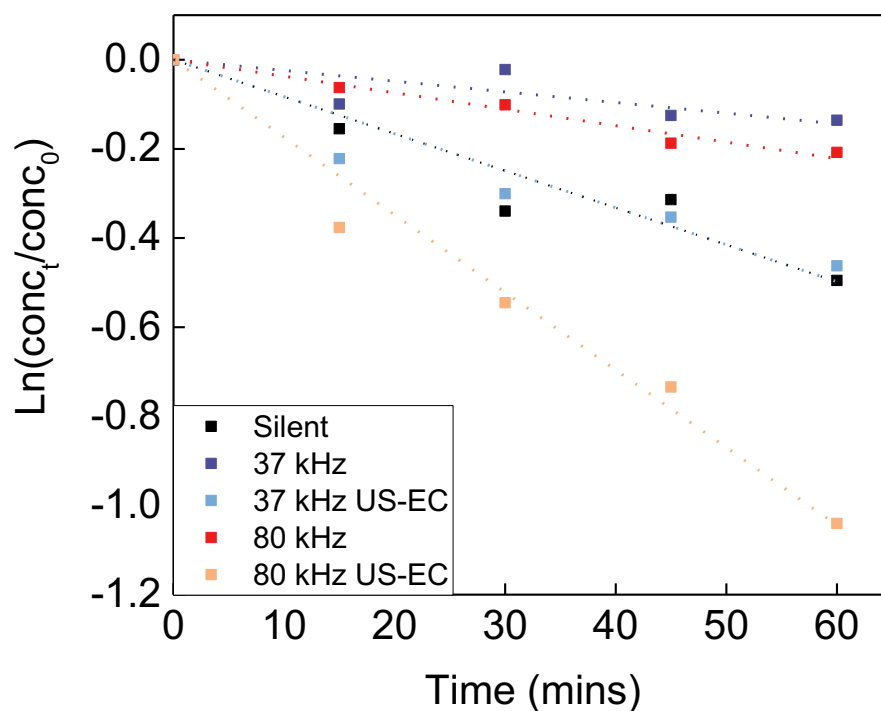


Figure 5.9: Reaction kinetics for sonoelectrochemical DCF degradation.

As can be seen from Table 5.3 and Figure 5.9, a strong synergistic factor was recorded in the 80 kHz US-EC conditions with the combined method having a rate constant almost 50% greater than the sum of the rate constants from the individual processes. Although no synergistic relationship was observed for 37 kHz sonication under the parameters used in this study, slight alterations of said parameters may yield a different result. In the previously mentioned prior study into the sonoelectrochemical degradation of diclofenac by Finkbeiner *et. al.*, they carried out the process using potentiostatic electrolysis at three different voltages; 2.8, 5.0 and 7.2 V.⁵¹ Interestingly, a minor synergistic effect was observed at 2.8 V but no synergism was recorded at the two higher voltages tested. In our own study when carrying out the US-EC degradation methods, the typical voltages ranged from 4–4.5 V thus in range with the voltages in the previous study that had no observable synergism. If more time was available, it would have been of interest to trial a range of current densities to determine if a different current may lead to a synergistic process.

5.3.4 Anode Material

As discussed in section (intro section on electrode), the choice of electrode material can greatly influence the selectivity and efficiency of electrochemical degradation processes. Boron doped diamond electrodes are used extensively across this field due to the mechanical and chemical stability of the diamond structure, coupled with the high electrical conductivity that is achieved via its p-type doping with boron.⁵⁷ It is of interest then to implement this electrode in to our experimental apparatus, Figure 5.10 illustrates the DCF degradation performance using BDD benchmarked against our previous results using Pt-Ti.

The removal of DCF from the solution proceeds at largely the same rate when using BDD as when using Pt/Ti for the first 45 mins, however, for the last 15 mins of the experiment the degradation rate increases substantially for BDD. In fact, in the last 15 mins alone, an average of ~30 % of the total DCF concentration was removed across the 3 repeats using BDD. One possible explanation for this trend may be as a result of the solution heating up. As previously mentioned, during the sonication runs we see the temperature of the water increase substantially over the hour. Typically, the water in the sonication bath is around 20 °C at the start of the experiment and can rise to as high as 50 °C by the end. However, looking at the LC-MS data for runs using Pt/Ti we see no indication of this rise in temperature with most of the degradation trends being largely linear. It may be that electrode passivation of Pt/Ti over the course of the experiments masks any improvement brought about by elevated temperatures. A key benefit offered by BDD is its resistance to passivation, and so degradation when using this material may be enhanced as the solution heats up.⁵⁸

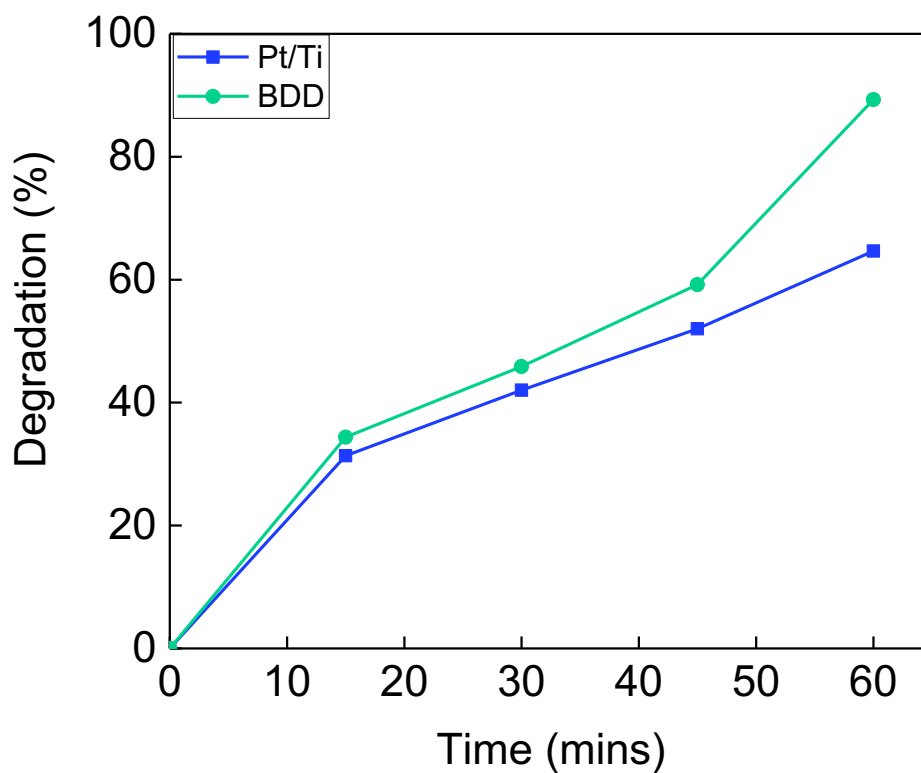


Figure 5.10: Degradation of DCF using either Pt/Ti (green line) or BDD (blue line) while combining electrolysis performed at 5 mA cm^{-2} and sonication at 80 kHz.

5.4 Conclusions and Future Work

In this study, we have examined the degradation of diclofenac via coupling constant-current electrolysis with sonication. The optimal degradation conditions were found using a Pt-Ti working electrode and Ti mesh counter electrode, at a current density of 5 mAcm^{-2} whilst sonicating the solution in an ultrasonic bath at 80 kHz. Under these parameters, ~64% of DCF was removed from the test sample.

As discussed in both chapter 1 and section 5.3.3, one of the key benefits to this approach is that parameter optimisation can yield a synergistic effect. We observed a high level of synergism when coupling sonication at 80 kHz with electrolysis yet no synergism at 37 kHz. Had more time been available, it would have been of interest to carry out a study using different current densities and/or electrolyte concentrations in hopes of finding a set of results that would yield synergism at that frequency.

Direct comparison between BDD and Pt/Ti was carried out by performing this process at equal current densities whilst sonicating the reaction at 80 kHz. Optimal degradation was achieved using BDD which removed DCF by close to 90% over 1 hour. An interesting observation was that the rate of degradation when using BDD drastically increased over the last 15 mins. It was suggested that this may be due to an improvement brought about by elevated temperatures in the absence of a passivating layer. Had more time been available, a temperature study could have been carried out that would confirm this theory.

An interesting result from the study was that the degradation of DCF in the 37 kHz US-EC experiment offered no improvement over a non-sonicated electrolysis. In section 5.3.2 we offered two possible theories to explain this result. In the first, we postulated that in our experiment an enhancement of mass transfer led to the formation of a passivating layer that deactivated the electrode. We proposed that the number of cavitation events occurring at 80 kHz is higher than at 37 kHz, which inhibited the formation of this insulating deposition at that frequency. It would be of interest to repeat this experiment across a range of different frequencies; should this explanation be accurate, alteration of the frequency may help determine a critical frequency, below which the application of ultrasound is not beneficial to the degradation of DCF. The second theory put forward is that the poor performance observed at 37 kHz was due to a degradation of the Pt/Ti anode under the more violent bubble collapses which occur at this frequency. Proper identification of the observed anodic deposition would help to determine if this is the case. Alternatively, it would be of interest to take further SEM images of the anode after removal of the deposition through cleaning to

assess if the observed roughness on the Pt/Ti (figure 5.8) persists. Throughout this chapter, we assessed and compared the degradation in each experiment solely by looking at the change in concentration of DCF. Whilst this is perfectly valid considering diclofenac is our target compound, a better idea of the efficacy of each technique could have been gained had access to a total organic carbon (TOC) analyser been possible. By measuring the TOC levels in our reaction mixture, we would gain insight into the degree of mineralisation that was being achieved in each run, ensuring that the degradation of DCF was not leading to increased levels of other potentially harmful organic by-products. Furthermore, as all the electrolyses in this project were performed at a fixed current, we can easily calculate the total charge passed. The benefit of this is that an evaluation of current efficiency could have been made using the results from a TOC experiment and the electrochemistry data, as has been achieved previously.⁵⁹

The lack of published data utilising sonoelectrochemical methods for the removal of DCF means that, to our knowledge, this is the first study investigating the efficiency of this process using more economical materials. Avoiding the use of BDD, and demonstrating that an alternative can be utilised, removes one of the largest impediments to the scaling up of this experiment. It is our belief that the work in this chapter lays the groundwork on which an effective and cheaper sonoelectrochemical degradation method for diclofenac may be found.

References

- 1 Y. Zhang, S. U. Geißen and C. Gal, *Chemosphere*, 2008, 73, 1151–1161.
- 2 S. González-Alonso, L. M. Merino, S. Esteban, M. López de Alda, D. Barceló, J. J. Durán, J. López-Martínez, J. Aceña, S. Pérez, N. Mastroianni, A. Silva, M. Catalá and Y. Valcárcel, *Environ. Pollut.*, 2017, **229**, 241–254.
- 3 N. A. H. Ismail, S. Y. Wee, N. H. Kamarulzaman and A. Z. Aris, *Environ. Pollut.*, 2019, **249**, 1019–1028.
- 4 M. Borecka, G. Siedlewicz, Ł. P. Haliński, K. Sikora, K. Pazdro, P. Stepnowski and A. Białk-Bielińska, *Mar. Pollut. Bull.*, 2015, **94**, 62–71.
- 5 K. V. Thomas and M. J. Hilton, *Mar. Pollut. Bull.*, 2004, **49**, 436–444.
- 6 G. McEneff, L. Barron, B. Kelleher, B. Paull and B. Quinn, *Sci. Total Environ.*, 2014, **476–477**, 317–326.
- 7 A. Lolić, P. Paíga, L. H. M. L. M. Santos, S. Ramos, M. Correia and C. Delerue-Matos, *Sci. Total Environ.*, 2015, **508**, 240–250.
- 8 Y. Yang, J. Fu, H. Peng, L. Hou, M. Liu and J. L. Zhou, *J. Hazard. Mater.*, 2011, **190**, 588–596.
- 9 B. Bonnefille, E. Gomez, F. Courant, A. Escande and H. Fenet, *Mar. Pollut. Bull.*, 2018, **131**, 496–506.
- 10 J. L. Oaks, M. Gilbert, M. Z. Virani, R. T. Watson, C. U. Meteyer, B. A. Rideout, H. L. Shivaprasad, S. Ahmed, M. J. Iqbal Chaudhry, M. Arshad, S. Mahmood, A. Ali and A. Ahmed Khan, *Nature*, 2004, **427**, 630–633.
- 11 M. A. Taggart, R. Cuthbert, D. Das, C. Sashikumar, D. J. Pain, R. E. Green, Y. Feltrer, S. Shultz, A. A. Cunningham and A. A. Meharg, *Environ. Pollut.*, 2007, **147**, 60–65.
- 12 J. Schwaiger, H. Ferling, U. Mallow, H. Wintermayr and R. D. Negele, *Aquat. Toxicol.*, 2004, **68**, 141–150.

- 13 B. Hoeger, B. Köllner, D. R. Dietrich and B. Hitzfeld, *Aquat. Toxicol.*, 2005, **75**, 53–64.
- 14 R. Triebkorn, H. Casper, V. Scheil and J. Schwaiger, *Anal. Bioanal. Chem.*, 2007, **387**, 1405–1416.
- 15 A. C. Mehinto, E. M. Hill and C. R. Tyler, *Environ. Sci. Technol.*, 2010, **44**, 2176–2182.
- 16 J. Näslund, J. Fick, N. Asker, E. Ekman, D. G. J. Larsson and L. Norrgren, *Aquat. Toxicol.*, 2017, **189**, 87–96.
- 17 P. Sathishkumar, K. Mohan, R. A. A. Meena, M. Balasubramanian, L. Chitra, A. R. Ganesan, T. Palvannan, S. K. Brar and F. L. Gu, *J. Hazard. Mater.*, , DOI:10.1016/j.jhazmat.2021.126135.
- 18 S. Tavazzi, B. Paracchini, G. Suurkuusk, G. Mariani, R. Loos, M. Ricci, B. M. Gawlik and S. Tavazzi, *Water Framework Directive Watch List Method Analysis of diclofenac in water WATCH LIST SUBSTANCE: DICLOFENAC – MONITORING METHOD*, 2014.
- 19 A. G. Capodaglio, A. Bojanowska-Czajka and M. Trojanowicz, *Environ. Sci. Pollut. Res.*, 2018, **25**, 27704–27723.
- 20 T. Poiger, H. R. Buser and M. D. Müller, *Environ. Toxicol. Chem.*, 2001, **20**, 256–263.
- 21 D. Vogna, R. Marotta, R. Andreozzi, A. Napolitano and M. D’Ischia, *Chemosphere*, 2004, **54**, 497–505.
- 22 A. Agüera, L. A. Perez Estrada, I. Ferrer, E. M. Thurman, S. Malato and A. R. Fernandez-Alba, *J. Mass Spectrom.*, 2005, **40**, 908–915.
- 23 P. Bartels and W. von Tümpling, *Sci. Total Environ.*, 2007, **374**, 143–155.
- 24 R. R. Giri, H. Ozaki, Y. Takayanagi, S. Taniguchi and R. Takanami, *Int. J. Environ. Sci. Technol.*, 2011, **8**, 19–30.

- 25 L. A. Pérez-Estrada, M. I. Maldonado, W. Gernjak, A. Agüera, A. R. Fernández-Alba, M. M. Ballesteros and S. Malato, *Catal. Today*, 2005, **101**, 219–226.
- 26 P. Calza, V. A. Sakkas, C. Medana, C. Baiocchi, A. Dimou, E. Pelizzetti and T. Albanis, *Appl. Catal. B Environ.*, 2006, **67**, 197–205.
- 27 L. Rizzo, S. Meric, D. Kassinos, M. Guida, F. Russo and V. Belgiorno, *Water Res.*, 2009, **43**, 979–988.
- 28 A. Achilleos, E. Hapeshi, N. P. Xekoukoulotakis, D. Mantzavinos and D. Fatta-Kassinos, *Chem. Eng. J.*, 2010, **161**, 53–59.
- 29 C. Martínez, M. Canle L., M. I. Fernández, J. A. Santaballa and J. Faria, *Appl. Catal. B Environ.*, 2011, **107**, 110–118.
- 30 I. Michael, A. Achilleos, D. Lambropoulou, V. O. Torrens, S. Pérez, M. Petrović, D. Barceló and D. Fatta-Kassinos, *Appl. Catal. B Environ.*, 2014, **147**, 1015–1027.
- 31 M. Tokumura, A. Sugawara, M. Raknuzzaman, M. Habibullah-Al-Mamun and S. Masunaga, *Chemosphere*, 2016, **159**, 317–325.
- 32 C. Zwiener and F. H. Frimmel, *Water Res.*, 2000, **34**, 1881–1885.
- 33 D. Vogna, R. Marotta, A. Napolitano, R. Andreozzi and M. D'Ischia, *Water Res.*, 2004, **38**, 414–422.
- 34 V. Naddeo, V. Belgiorno, D. Ricco and D. Kassinos, *Ultrason. Sonochem.*, 2009, **16**, 790–794.
- 35 A. D. Coelho, C. Sans, S. Esplugas and M. Dezotti, *Ozone Sci. Eng.*, 2010, **32**, 91–98.
- 36 A. Aguinaco, F. J. Beltrán, J. F. García-Araya and A. Oropesa, *Chem. Eng. J.*, 2012, **189–190**, 275–282.
- 37 M. Ravina, L. Campanella and J. Kiwi, *Water Res.*, 2002, **36**, 3553–3560.
- 38 N. De la Cruz, J. Giménez, S. Esplugas, D. Grandjean, L. F. De Alencastro and C.

- Pulgarín, *Water Res.*, 2012, **46**, 1947–1957.
- 39 S. Bae, D. Kim and W. Lee, *Appl. Catal. B Environ.*, 2013, **134–135**, 93–102.
- 40 R. Homlok, E. Takács and L. Wojnárovits, *Chemosphere*, 2011, **85**, 603–608.
- 41 Q. Liu, X. Luo, Z. Zheng, B. Zheng, J. Zhang, Y. Zhao, X. Yang, J. Wang and L. Wang, *Environ. Sci. Pollut. Res.*, 2011, **18**, 1243–1252.
- 42 A. Kimura, M. Osawa and M. Taguchi, *Radiat. Phys. Chem.*, 2012, **81**, 1508–1512.
- 43 H. Yu, E. Nie, J. Xu, S. Yan, W. J. Cooper and W. Song, *Water Res.*, 2013, **47**, 1909–1918.
- 44 A. Bojanowska-Czajka, G. Kciuk, M. Gumiela, S. Borowiecka, G. Nałęcz-Jawecki, A. Koc, J. F. Garcia-Reyes, D. S. Ozbay and M. Trojanowicz, *Environ. Sci. Pollut. Res.*, 2015, **22**, 20255–20270.
- 45 J. Hartmann, P. Bartels, U. Mau, M. Witter, W. v. Tümpling, J. Hofmann and E. Nietzschmann, *Chemosphere*, 2008, **70**, 453–461.
- 46 E. Nie, M. Yang, D. Wang, X. Yang, X. Luo and Z. Zheng, *Chemosphere*, 2014, **113**, 165–170.
- 47 A. Ziyilan, S. Dogan, S. Agopcan, R. Kidak, V. Aviyente and N. H. Ince, *Environ. Sci. Pollut. Res.*, 2014, **21**, 5929–5939.
- 48 X. Zhao, Y. Hou, H. Liu, Z. Qiang and J. Qu, *Electrochim. Acta*, 2009, **54**, 4172–4179.
- 49 E. Brillas, S. Garcia-Segura, M. Skoumal and C. Arias, *Chemosphere*, 2010, **79**, 605–612.
- 50 M. D. Vedenyapina, E. D. Strel’Tsova, N. A. Davshan and A. A. Vedenyapin, *Russ. J. Appl. Chem.*, 2011, **84**, 204–207.
- 51 P. Finkbeiner, M. Franke, F. Anschuetz, A. Ignaszak, M. Stelter and P. Braeutigam, *Chem. Eng. J.*, 2015, **273**, 214–222.

- 52 I. Korolev, K. Yliniemi, M. Lindgren, L. Carpén and M. Lundström, *Metall. Mater. Trans. B Process Metall. Mater. Process. Sci.*, 2021, **52**, 3107–3119.
- 53 T. Rundlöf, M. Mathiasson, S. Bekiroglu, B. Hakkarainen, T. Bowden and T. Arvidsson, *J. Pharm. Biomed. Anal.*, 2010, **52**, 645–651.
- 54 R. G. Compton, J. C. Eklund, S. D. Page, G. H. W. Sanders and J. Booth, *J. Phys. Chem.*, 1994, **98**, 12410–12414.
- 55 J. R. Steter, D. Dionisio, M. R. V. Lanza and A. J. Motheo, *J. Appl. Electrochem.*, 2014, **44**, 1317–1325.
- 56 Y. Huang, T. Zhou, X. Wu and J. Mao, *Ultrason. Sonochem.*, 2017, **38**, 735–743.
- 57 Y. Einaga, *Bull. Chem. Soc. Jpn.*, 2018, **91**, 1752–1762.
- 58 J. G. Manjunatha, *Voltammetry for Sensing Applications*, Bentham Science Publishers, 2022.
- 59 X. Yu, M. Zhou, Y. Hu, K. Groenen Serrano and F. Yu, *Environ. Sci. Pollut. Res.*, 2014, **21**, 8417–8431.

Conclusions and Future Work

In the work presented in this thesis, electro-oxidation has been utilised in the development of several so-called “green” processes with applications in renewable energy devices, oxygen-evolving systems for space exploration, and water decontamination methods. In Chapter 1 we introduced the motivations behind our research, setting the backdrop of the current climate crisis and introducing the reader to the fundamentals of the three areas of research covered in the rest of the thesis.

In Chapter 3 we reported the development of a novel anion-exchange membrane electrolyser which makes use of the electro-oxidation of the naturally occurring polymer, lignin. The global shift to renewable energy necessitates an appropriate method of energy storage for when intermittent renewable sources (e.g. wind, solar, tidal) are not available. Electrolytic water splitting offers a solution to this problem, with renewable energy stored as hydrogen fuel.² Of the two half-reactions which constitute water splitting, the oxygen evolution reaction is responsible for the majority of the overpotentials associated with this process; these overpotentials can be reduced by coupling the hydrogen evolution reaction with the electro-oxidation of an organic feedstock. Using a novel membrane, which is a co-polymer of dehydrofluorinated poly(vinylidene fluoride-co-hexafluoropropylene) with (vinylbenzyl)trimethylammonium chloride and N-vinylimidazole, simultaneous electrolytic water splitting and electro-oxidation of lignin was performed. Using Pt/C and Pt/Ru catalysts impregnated on carbon cloth, it was found that the membrane performed comparably to a commercially available equivalent, matching previously reported performance in the literature.³ However upon repeated use, the performance of this membrane began to deteriorate. SEM imaging of the membrane revealed huge morphological changes to the membrane with significant holing having developed. Previous work reported in the literature had suggested that in alkaline solutions, membranes containing the benzyl trimethylammonium moieties present in our samples were vulnerable to hydroxide attack via an S_N2 mechanism.⁴ Comparison of IR spectra recorded on our samples before and after extensive use revealed that the peaks associated with the terminal C-N⁺ stretches in the quaternary amine groups were not present in the used membrane seemingly confirming this degradation. In section 3.3.4 we suggest how an alternative monomer could be used that may be more resistant to this degradation mechanism, producing a more robust membrane.

The work presented in Chapter 4 demonstrates just how far-reaching the applications of electro-oxidation are as we present the first experimental verification for the efficiency of gas-evolving electrolysis at gravity levels between 0 & 1 g. The future of manned space

travel is heavily dependent on oxygen production, with a great deal of interest now in the utilisation of in-situ resources as feedstock. Gas evolving electrolysis is one such route that can make use of the abundance of oxygen containing resources on many of the destinations in planned future space missions (e.g. ice water on the Moon and Mars, metal-oxide abundant Lunar soil). Yet, although the efficiency of this electrolysis has been extensively studied in microgravity (~ 0 g) and at gravity levels greater than Earth's gravity, no experimental study had been performed to verify the performance of the process in reduced gravity environments. In the investigation detailed in this chapter, electrolysis was performed in cells attached to a small centrifuge on a parabolic flight. In the background of microgravity, the cells were spun at different rates to simulate several different gravity levels including the equivalent g-levels of the Moon and Mars. It was found that at a fixed potential, electrolytic oxygen production would suffer a 10% and 6% reduction if performed on the Moon and Mars respectively. Perhaps more importantly, it was discovered that there was good agreement in the trends recorded in microgravity and hypergravity which would suggest that extrapolation can be used in future studies to predict how systems will perform in reduced gravity. This could potentially remove a large financial impediment to the development of gas-evolving systems for future space travel.

In Chapter 5, a combined sonoelectrochemical approach to remove the anti-inflammatory drug diclofenac from aqueous solution was used. In optimal conditions (5 mA cm⁻² electrolysis coupled with 80 kHz sonication) we observed a strong synergistic effect, with $\sim 64\%$ of the pollutant removed in 1 hour. This was achieved whilst using a Pt-Ti anode and a Ti mesh cathode in a simple ultrasonic bath reactor. One of the key aims of this study was to investigate the efficacy of this process in a more economically attractive experimental setup than that which had previously been reported in the literature (BDD anode & cathode coupled with high frequency ultrasound).¹ A comparison was then performed using identical parameters but with a BDD anode substituted for the Pt-Ti. As could be expected, the BDD anode performed significantly better than Pt-Ti removing over 90% of diclofenac in 1 hour. This difference in performance was attributed to the development of a passivating layer on Pt-Ti, though it is possible that the formation of this layer could be inhibited through modification of the sonication parameters; this would be an exciting route for future study. This aside, the promising results presented in this chapter demonstrate that cheaper alternatives can be utilised in the sonoelectrochemical degradation of diclofenac. In all the examples cited across both chapters, the studies were performed in small batch reactors. Widespread implementation of this technique would require a significant scaling up of the

process and, since the performance of the technique is heavily reliant on reactor design, it is yet unclear if this approach is suited to larger, continuous-flow systems. As mentioned in section 1.4, the issue of energy consumption may too impede widespread adoption of this approach. It is likely that reducing this energy cost will be a focal point for future investigations in this field.

References:

- 1 P. Finkbeiner, M. Franke, F. Anschuetz, A. Ignaszak, M. Stelter and P. Braeutigam, *Chem. Eng. J.*, 2015, **273**, 214–222.
- 2 J. S. Wallace and C. A. Ward, *Int. J. Hydrogen Energy*, 1983, **8**, 255–268.
- 3 A. Caravaca, W. E. Garcia-Lorefice, S. Gil, A. de Lucas-Consuegra and P. Vernoux, *Electrochem. commun.*, 2019, **100**, 43–47.
- 4 T. Sata, M. Tsujimoto, T. Yamaguchi and K. Matsusaki, *J. Memb. Sci.*, 1996, **112**, 161–170.

Appendix

Appendix 1 – Microgravity Data

As discussed in chapter 4, an issue was encountered in the microgravity study whereby current loss through the grounded pressure sensor gave rise to false “low resistance” measurements (see section 4.3.2). Measurements where this had occurred were ultimately removed from our data sets, meaning that an uneven number of replicates were available for each data point. The remaining raw data is provided in the tables below, orange boxes indicate these “low resistance” measurements which were omitted. Each column header gives an indication of flight and cell number, for example, F1C1 corresponds to flight 1 - cell 1.

50 mA cm⁻²:

G-level	F1C1	F1C2	F3C1	F3C3	Avg	STDev	Error
0.166	2.047126		2.063177		2.055151	0.01135	0.008026
0.25	2.046671	2.041443	2.065817	2.056308	2.05256	0.010771	0.005386
0.3			2.070081	2.058671	2.064376	0.008068	0.005705
0.376	2.044415	2.037139	2.068021	2.058179	2.051938	0.013823	0.006912
0.5	2.043758	2.035862	2.066783	2.059376	2.051445	0.014143	0.007072
0.6	2.045423	2.035073	2.067886	2.058933	2.051828	0.014492	0.007246
0.8	2.042549	2.035068	2.066622	2.058309	2.050637	0.014401	0.007201
1	2.041663	2.036382	2.064601	2.05979	2.050609	0.013693	0.006847

75 mA cm⁻²:

G-level	F2C1	F2C2	F2C3	Avg	STDev	Error
0.166						
0.25			2.114116	2.114116		
0.3			2.114756	2.114756		
0.376	2.118068	2.133366	2.112576	2.121337	0.010774	0.00622
0.5	2.113366	2.134994	2.107532	2.118631	0.014468	0.008353
0.6	2.117231	2.134681	2.110443	2.120785	0.012504	0.007219
0.8	2.110643	2.127496	2.108891	2.115677	0.010273	0.005931
1	2.112233	2.131167	2.105188	2.116196	0.013435	0.007757

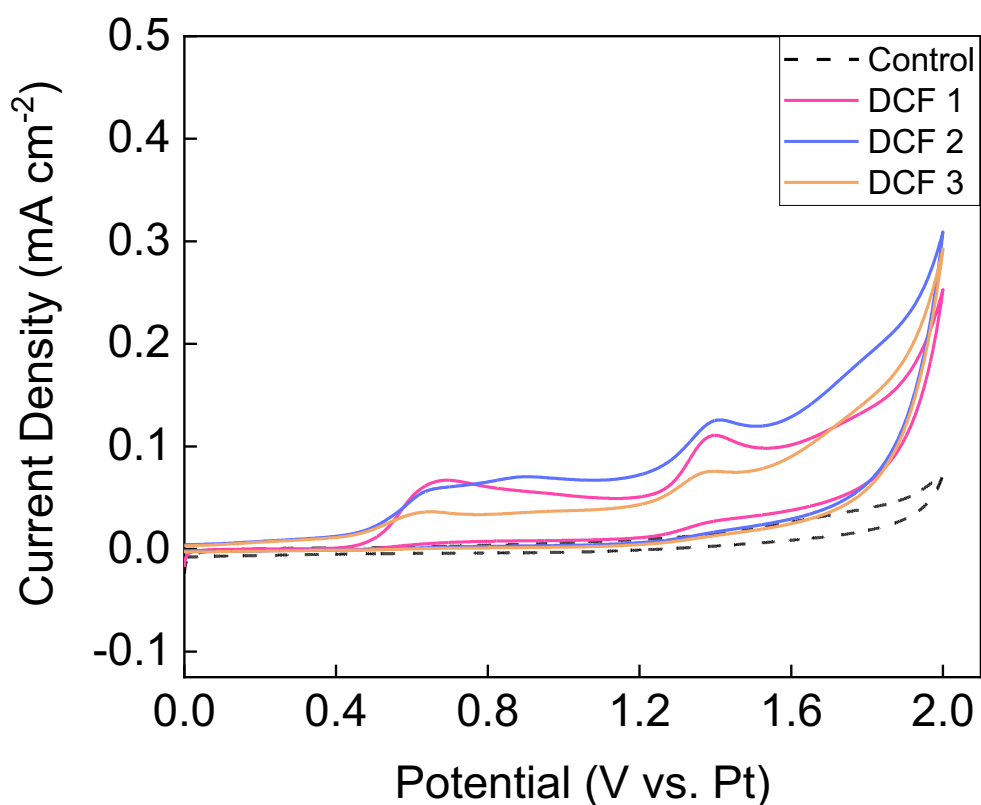
100 mA cm⁻²:

G-level	F1C1	F1C2	F3C1	F3C3	Avg	STDev	Error
0.166	2.167291	2.147969			2.15763	0.013663	0.009661
0.2	2.161349				2.161349		
0.3	2.159523	2.143909	2.246844	2.221671	2.192987	0.049165	0.024583
0.376			2.260349	2.221877	2.241113	0.027204	0.019236
0.5	2.155512	2.143629	2.27124	2.233767	2.201037	0.061557	0.030779
0.6	2.153505	2.134819	2.271694	2.229731	2.197437	0.064312	0.032156
0.8	2.150928	2.133787	2.277571	2.223583	2.196467	0.066623	0.033311
1	2.146696	2.135356	2.268721	2.201443	2.188054	0.06103	0.030515

2.075 V vs Ag/AgCl:

G-level	F2C1	F2C2	F2C3	Avg	STDev	Error
0.25	96.53676		96.98967	96.76321	0.320255	0.226454
0.3			96.80173	96.80173		
0.376	99.37626		98.58275	98.9795	0.561097	0.396755
0.5	97.48047	90.11957	98.89693	95.49899	4.71224	2.720613
0.6	101.3347	89.26916	98.91272	96.50553	6.382813	3.685119
0.8	99.0368	88.78147	99.83578	95.88468	6.164521	3.559088
1	100.4247	91.3182	98.72443	96.82245	4.842041	2.795553

Appendix 2 – Diclofenac CV



The figure above shows the cyclic voltammetry results collected using a in a 3-electrode cell consisting of a BDD working electrode (S.A. = 0.85 cm²), a Ti mesh counter electrode, and a Pt wire pseudo-reference electrode. The potential was scanned between -2.0 and +2.0 V at a scan rate of 100 mV s⁻¹. DCF 1-3 correspond to the three scans of 1 mM DCF in 0.1 M NaOH, the control used was 0.1 M NaOH.